Technische Universität München
TUM School of Natural Sciences

TUM

Synthesis and Characterization of Novel Tetradentate NHC Ligands with Modified Electronic Properties and Transition Metal Complexes for Oxidation Catalysis and Medicinal Chemistry

Wolfgang Roland Erich Büchele

Vollständiger Abdruck der von der TUM School of Natural Sciences der Technischen Universität

München zur Erlangung eines

Doktors der Naturwissenschaften (Dr. rer. nat.)

genehmigten Dissertation.

Vorsitz: Prof. Dr. Klaus Köhler

Prüfende der Dissertation:

1.   Prof. Dr. Fritz E. Kühn
2.   Prof. Dr. Tom Nilges

Die Dissertation wurde am 04.02.2025 bei der Technischen Universität München eingereicht und durch die TUM School of Natural Sciences am 25.02.2025 angenommen.

„Praesentia non est indicium meriti"
oder zu deutsch
 "Anwesenheit ist kein Leistungsmerkmal"

Die vorliegende Arbeit wurde im Zeitraum von Januar 2022 bis Dezember 2024 im Fachgebiert Molekulare Katalyse der Technischen Universität München angefertigt.

Mein erster und besonderer Dank gilt meinem Doktorvater

Herrn Prof. Dr. Fritz E. Kühn

Für die reibungslose Aufnahme in seiner Arbeitsgruppe, das mir entgegengebrachte Vertrauen und die Möglichkeit, eine spannende Thematik zu bearbeiten. Weiterhin bin ich für die forscherische Freiheit am Arbeitskreis dankbar, die für ein besonderes, angenehmes und produktives Forschungsumfeld schafft. Zusätzlich möchte ich mich auch für die zeitnahen Rückmeldungen und Feedbacks auch außerhalb der regulären Arbeitszeiten bedanken.

Acknowledgment

Im Besonderen möchte ich zunächst meinem Masteranden **Andi** für seinen unermüdlichen Ehrgeiz bei der Arbeit danken. Auch wenn man dir ab und zu einen kleinen Schubs in die richtige Richtung geben musste, hast du eine tolle Arbeit abgeliefert und mir sehr viel Arbeit abgenommen. Außerdem schätze ich unsere unkomplizierte Zusammenarbeit und die daraus entstandene Freundschaft sehr.

Als Nächstes gilt mein besonderer Dank **Marina**, **Anna** und **Erik** für ihre super Arbeit im Rahmen ihres Forschungspraktikums. Eure Unterstützung hat mir vieles erleichtert, und die lustigen Hauspartys, Feiern und sonstigen Abende mit euch werde ich nicht vergessen. Wie sagt man so schön *„Erfolg hat man, Glück wünscht man"* deswegen wünsche ich euch viel Glück bei euren eigenen Promotionsprojekten und danke euch nochmal für die fantastische Zeit und eure großartige Hilfe!

Ein weiterer besonderer Dank gilt den deutschen Steuerzahlern für die Finanzierung meiner Ausbildung und der Technischen Universität München für die Bereitstellung der hervorragenden Infrastruktur.

Als nächste möchte ich einen besonderen Dank an meine Freunde richten. **Philipp Pfändner**, **Roberta Sangiovanni**, **Moritz Leonhardt**, **Sina Ivakko**, **Aleksandar Jagličić**, **Julian Kufer**, **Yannik Seidel** und **Kevin Heiser**.

Philipp da du ja meintest, es soll kurz sein – hier, fünf Buchstaben: DANKE.

Roberta, meine Güte, was wir alles zusammen im Studium erlebt haben – wie du mich und Phil durch QM geboxt hast, die unvergesslichen Urlaube, die zahlreichen witzigen Abenden mit geilem Essen und all die unzähligen lustigen Momente mit dir. Einfach unglaublich und vielen Dank!

Moritz, wir kennen uns jetzt schon seit über 26 Jahr – das ist schon fast eine Ehe. Meister, ich wollte einfach mal Danke sagen, für deine Jahrelange Freundschaft und all die genialen Momente, die wir seit unserer Kindheit zusammen erlebt haben. Von unzähligen Mario-Kart-Rennen über Sommer Camps, Camping, Partys, Festivals und Snowboard-Abenteuer bis hin zu unseren crazy Geschäftsideen- so viele unvergessliche Erinnerungen. Auf dich konnte ich mich immer verlassen, und genau dafür möchte ich dir an dieser Stelle nochmal ausdrücklich Danke sagen!

Sina, seit unserer Schulzeit in Finnland haben wir so viel zusammen gelacht – und über die Jahre ist daraus eine großartige Freundschaft entstanden. Danke für all die witzigen Abende und die unzähligen aufbauenden Gespräche mit dir! Auch wenn du nicht mehr in München bist und wir jetzt meist stundenlang per Telefon quatschen, freue ich mich auf ein baldiges Wiedersehen. Kiitos paljon!

Alex, was haben wir gelacht während der Praktika, die wir zusammen betreut haben. Ohne dich wäre die Zeit – und die Promotion – nur halb so witzig gewesen. Es hat einfach riesigen Spaß mit dir gemacht. Auch für die zahlreichen lustigen Kaffeepausen und stundenlangen spannenden Gespräche: Vielen Dank.

Julian, was haben wir schon alles zusammen erlebt – die legendäre Zeit im Studentenwohnheim, Festivals, Pokerabende und die ganzen Partys- more to come!. Es gab so viele witzige Momente mit dir, und ich wollte einfach mal Danke sagen für die geile Zeit.

Yannik & **Kevin**: Jungs wie viele Stunden haben wir schon in Siedler verbracht ? Die unzähligen Gespräche über Gott und die Welt – und natürlich eure, ehrlichen, neutralen Meinungen, wenn ich sie gebraucht habe. Es waren immer geniale Abende mit euch, voller Spaß und entspannter Momente nach einem stressigen Tag. Danke für die großartige Zeit mit euch

Zu guter Letzt gilt mein besonderer Dank meinen kleinen geheimen Helfern, meiner Familie, ohne die ich diesen Weg niemals hätte meistern können.

Zuerst möchte ich meiner Schwester, **Dr**. **Dominique Büchele**, danken. **Dominique**, du hast mich immer unterstützt, auch wenn du mir immer gesagt hast: *„studier bloß nicht Chemie, mach was anderes.“* Deine Ratschläge und deine Hilfe, die ich jedes Mal bekommen habe, waren von unschätzbarem Wert.

Ich möchte die Chance nutzen, meinem Vater, **Dr**. **Wolfgang Büchele**, zu danken. Papa, ich weiß, du sagst oft: *„In der Kürze liegt die Würze“*, aber in diesem Fall reicht die Kürze nicht aus, um dir für alles zu danken, und es wird jetzt halt etwas länger.

Du hast immer gesagt: *„Ist doch selbstverständlich“*, wenn ich dich um Hilfe gebeten habe, aber ich möchte trotzdem Danke sagen für die zahllosen Stunden, die du für mich geopfert hast, wenn ich mal wieder Mist gebaut habe und du es grade biegen musstest, oder wenn ich kurz vor knapp angerannt kam und du mitten in der Nacht einen Bericht oder eine Abschlussarbeit von mir lesen und korrigieren musstest, damit sie noch rechtzeitig fertig wurde.

Außerdem waren deine Ratschläge nicht nur praktisch, sondern haben mich oft auch auf neue Wege gebracht. Du hast mir von klein auf gezeigt, wie wichtig es ist, Probleme anzupacken – sei es beim Kabelziehen, beim Verlegen von Rohrleitungen im Garten oder bei Herausforderungen im Studium, bei der Promotion oder im Leben. Wie sagst du so schön: *„Probleme gibt es nicht, sondern nur Lösungen“*. Deine ruhige Herangehensweise hat mir beigebracht, auch in schwierigen Momenten einen klaren Kopf zu bewahren. Diese Haltung und manche deiner Lebensweisen – ob bewusst oder unbewusst vermittelt – haben mich geprägt. Manchmal sagt Dominique am Telefon, ich rede und höre mich an wie Papa.

Ein großer Teil meines Erfolgs ist dir zu verdanken, und ich möchte, dass du weißt, wie unglaublich dankbar ich dir für alles bin – auch wenn du es als selbstverständlich ansiehst.

Eine der wichtigsten Personen nach meinem Vater, der ich noch danken möchte, ist meine Mutter, **Dr. Uta Büchele**.

Mama, leider gibt es nicht genug Worte, um zu beschreiben, wie sehr ich dich lieb habe und wie viel du mir bedeutest. Von all den oben genannten Leuten gebührt dir definitiv mein größter Dank. Dein kleines Bärchen hat es geschafft, und das verdanke ich in so vielerlei Hinsicht dir. Ich weiß, es war nicht einfach mit mir und wie viele schlaflose Nächte du wegen mir hattest, weil du dir Sorgen gemacht hast, und wie viele zahllosen Stunden du geopfert hast, um mir während meines Lebens und des Studiums zu helfen – sei es beim Lernen, beim Schreiben eines Berichtes oder einfach nur, indem du für mich da warst. Deine Ratschläge, ob liebevoll oder direkt, haben mir oft den richtigen Weg gezeigt. Wenn mal wieder mein Fokus auf unwichtigen Dingen im Leben gerichtet waren, war es deine Sprüche *„Jetzt setz dich auf deine vier Buchstaben"* oder *„Komm endlich in die Pötte"*, die den Focus wieder in die richtige Richtung gelenkt haben. Du hast mir beigebracht, wie wichtig es ist, im Leben Danke zu sagen und dass es sich lohnt, hart zu arbeiten, und dass man niemals aufgeben sollte, egal, wie schwierig die Situation erscheint.

Wenn ich ein Problem hatte, warst du immer die erste Person, zu der ich rennen konnte. Egal, wie groß oder klein das Problem war, du hast mich in den Arm genommen, mich getröstet und mir immer das Gefühl gegeben, dass alles gut wird. Die Zeit, die du dir jedes Mal genommen hast, wenn ich ein Problem hatte, und die unzähligen „Care Pakete", die du mir mit Liebe gepackt hast, bedeuten mir mehr, als ich in Worte fassen kann.

Ich weiß, es war nicht einfach für dich, deinem kleinen Bärchen die Freiheiten zu geben, die du mir gegeben hast, und du dich oft allein gefühlt hast. Mama, auch wenn ich nicht der Beste darin bin, mich regelmäßig zu melden (können meine Freunde definitiv bestätigen), möchte ich, dass du weißt, dass ich jeden Tag an dich gedacht habe. Auch wenn ich doch etwas älter geworden und vielleicht etwas größer bin und eigentlich jetzt der Yogi-Bär bin, werde ich immer dein kleines Bärchen bleiben, egal in welchem Lebensabschnitt ich mich befinde.

Mama, der größte Teil meines Erfolgs ist dir zu verdanken, weil du nicht nur die beste Mama bist, sondern auch immer für mich da warst.

Vielen Dank für alles!

Abstract

In this work, the synthesis and characterization of novel bio-inspired macrocyclic tetradentate and open-chained *N*-heterocyclic carbene (NHC) ligands are designed with distinct electronic properties. These ligand precursors were employed in the synthesis of various transition metal complexes, such as iron and group 10 and 11 metals. The resulting transition metal complexes were developed for catalytic and medicinal applications.

Compared to the existing imidazole-based system, two ligands with 4,5-diphenylimidazole or 4,5-(*para*-fluorophenyl)imidazole as NHC moieties were synthesized for epoxidation catalysis. One of the key objectives is to explore how the ligands' donor properties influence the iron center and the stability of the complexes in oxidation catalysis. In addition, a naphtho[2,3-*d*]imidazolium-based ligand was developed to improve the stability of the resulting iron complexes compared to the existing benzimidazole-based system.

Furthermore, palladium, platinum, and gold complexes containing novel saturated and unsaturated ethylene-bridged NHC ligands (macrocyclic and open-chained) were investigated *in vitro* for their cytotoxic effects on cancer cells. Notably, one of the synthesized gold complexes demonstrated the ability to induce apoptosis in neuroblastoma cells and overcome cisplatin resistance.

Additionally, a pipetting robot named "*MULA*" was developed to enhance laboratory workflows and improve the reproducibility of results. This versatile robot supports various applications, including precise timed catalytic sampling, high-throughput screening for crystallization optimization, and precise NMR sample preparation.

Kurzzusammenfassung

In dieser Arbeit wird die Synthese und Charakterisierung neuartiger, makrozyklischer und offenkettiger *N*-heterozyklischer Carbene (NHC), die unterschiedliche elektronische Eigenschaften aufweisen, präsentiert. Diese Liganden wurden zur Synthese verschiedener Übergangsmetallkomplexe mit Eisen und Metallen der Gruppen 10 und 11 verwendet. Diese Übergangsmetallkomplexe wurden für katalytische und medizinische Anwendungen entwickelt.

Im Vergleich zum bereits existierenden Imidazol-basierten System werden zwei Liganden entwickelt, welche aus 4,5-Diphenylimidazol- und 4,5-(*para*-Fluorphenyl)imidazol Einheiten bestehen. Die Wirkung der donierenden Eigenschaften der Liganden auf das Eisenzentrum und die einhergehende Stabilität der Komplexe werden untersucht. Außerdem wurde ein Ligand auf Naphtho[2,3-*d*]imidazolium Basis entwickelt, um die Stabilität zukünftiger Eisen-Katalysatoren zu verbessern.

Darüber hinaus wurden Palladium-, Platin- und Gold-Komplexe, mit neuartigen gesättigten und ungesättigten, ethylenverbrückten NHC-Liganden (makrozyklisch und offenkettig) auf ihre zytotoxischen Wirkungen auf Krebszellen *in vitro* untersucht. Einer der synthetisierten Gold-Komplexe zeigte die Fähigkeit, Apoptose in Neuroblastomzellen auszulösen und Cisplatin-Resistenzen zu überwinden.

Des Weiteren wurde ein Pipettierroboter namens *„MULA"* entwickelt, um Laborabläufe zu optimieren und die Reproduzierbarkeit von Ergebnissen zu verbessern. Dieser vielseitige Roboter unterstützt verschiedene Anwendungen, einschließlich präziser zeitgesteuerter katalytischer Probenahme, Hochdurchsatz-Screening zur Optimierung der Kristallisation verschiedener Verbindungen und präzises Vorbereiten von NMR Ansätzen.

Abbreviations

A	Adenine
BRAF	B-Raf Proto-Oncogene, Serine/Threonine Kinase
C	Cytosine
Cisplatin	*Cis*-diamminedichloridplatinum(II)
CV	Cyclic voltammetry
CYP 450	Cytochrome P450
DCM	Dichloromethane
DFT	Density-functional theory
DMSO	Dimethyl sulfoxide
DNA	Deoxyribonucleic acid
$E_{1/2}$	Half-cell potential
EGFR	Epidermal Growth Factor Receptor
ESI	Electrospray ionization
Et_2O	Diethyl ether
Fc	Ferrocene
FDA	United States Food and Drug Administration
G	Guanine
G4-DNA	Guanine quadruplex
GSH	Gluthathione
h	Hour
His	Histidine
HOMO	Highest occupied molecular orbital
HMDS	Hexamethyldisilazane
HPPO	Hydrogen peroxide propylene oxide
IC_{50}	Half maximal inhibitory concentration
L	Ligand
LA	Lewis acid
LUMO	Lowest unoccupied molecular orbital
Me	Methyl
MeCN	Acetonitrile
MeOH	Methanol
min	Minute
MS	Mass spectroscopy
NHC	*N*-heterocyclic carbene

NMR	Nuclear magnetic resonance
OTf	Trifluoromethanesulfonate
Ph	Phenyl
Ph-F	*Para*-fluorophenyl
PhMDA	Pharmaceuticals and Medical Devices Agency
PF_6	Hexafluorophosphate
ROS	Reactive oxygen species
SC-XRD	Single crystal X-ray diffraction
T	Thymine
TEP	Tolman electronic parameter
THF	Tetrahydrofuran
TOF	Turnover frequency
TON	Turnover number
Trx	thioredoxin
TrxR	Thioredoxin reductase
UV	Ultraviolet
Vis	Visible
WHO	World Health Organization

Table of Contents

1. Introduction

1.1. Oxidation Catalysis

The production of complex pharmaceuticals and polymers, amongst other important industrial goods, relies on functionalizing and converting various alkanes, primarily obtained by refining mineral oil and natural gas.[1-7] After refining, the crude mineral oil is distilled into fractions, such as gaseous fuel, naphtha, kerosene, and heavier compounds.[7-9] Thermal steam cracking of naphtha results in unsaturated hydrocarbons, including ethylene and propylene, with an annual production of 225.5 million tons (2022) and 150.3 million tons (2022).[10-14]

Besides being polymerized into highly sought-after polyethylene and polypropylene, a significant portion is converted into ethylene oxide and propylene oxide through epoxidation.[3, 15-17] This process typically uses hydrogen peroxide, alkyl hydroperoxides, peracids, or oxygen in the presence of a transition metal (TM) catalyst to convert the olefins to their respective epoxides.[18, 19] The interest in these epoxides lies in their reactivity, as the tension in the three-membered ring allows for regio- and stereoselective opening by numerous nucleophiles and also mechanistic interactions for antibiotic and antitumor reagents.[20] The resulting 1,2 functionality is a common biological motif and thereby has a major significance for organic synthesis. Consequently ethylene- and propylene oxide are subsequently converted into glycol, polycarbonates, polyesters, polyurethanes, and epoxy resins, among other products.[9, 21-26]
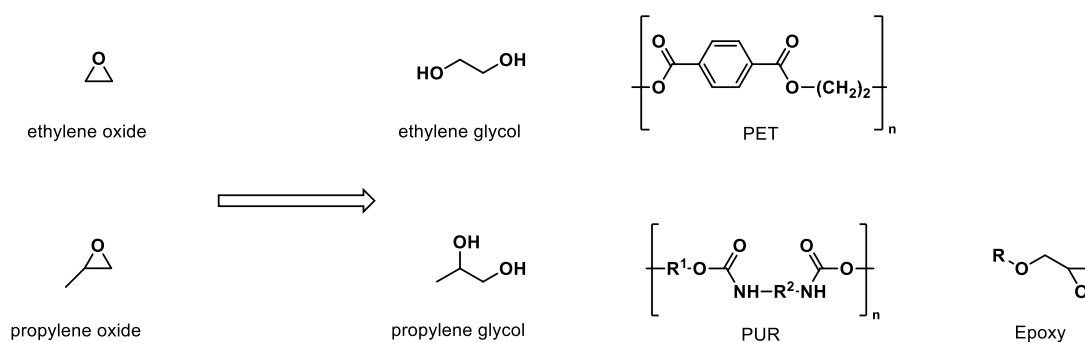
Figure 1. Examples of products of ethylene- and propylene oxide.[9, 21-26]

1.1.1. Industrial Olefin Epoxidation Catalysis

In the 20th century, *Union Carbide* synthesized ethylene oxide *via* the two-step chlorohydrin process, achieving 80% selectivity. However, the process was inefficient economically due to the high chlorine consumption and wastewater treatment.[27] To address this, *Union Carbide* developed a direct catalytical oxidation process, which remains today's most common industrial method for ethylene epoxidation. Ethylene is directly oxidized by oxygen from air or pure oxygen and catalyzed *via* an α-alumina-supported silver nanoparticle catalyst.[27, 28] However,

this process is only applicable to olefins without allylic C-H bonds due to the stabilization of the olefin resulting in low yield and selectivity towards the epoxide.[29, 30]
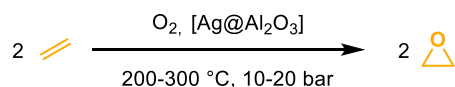
Scheme 1. Ethylene epoxidation with [Ag@Al$_2$O$_3$] and oxygen.[28]

When propylene is reacted under the same conditions, a large margin is over-oxidized to CO_2 and H_2O, and the formation of acrolein or acrylic acid as main products occurs.[27, 31, 32] The development of an industrial direct oxidation process for propylene using selectively dioxygen to epoxidize propylene is still in development and has been referred to in chemistry as the "holy grail" due to its difficulty.[9, 27, 30, 33-35] The most common procedures for obtaining propylene oxide are the chlorohydrin and (hydro)peroxide processes.[9, 27, 30, 31]

The chlorohydrin route (**Scheme 2**) includes a two-step process using chlorine and water, which generates hypochlorous acid as an intermediate and reacts with polypropylene to the propylene chlorohydrin isomers at 35-50 °C and 2-3 bar.
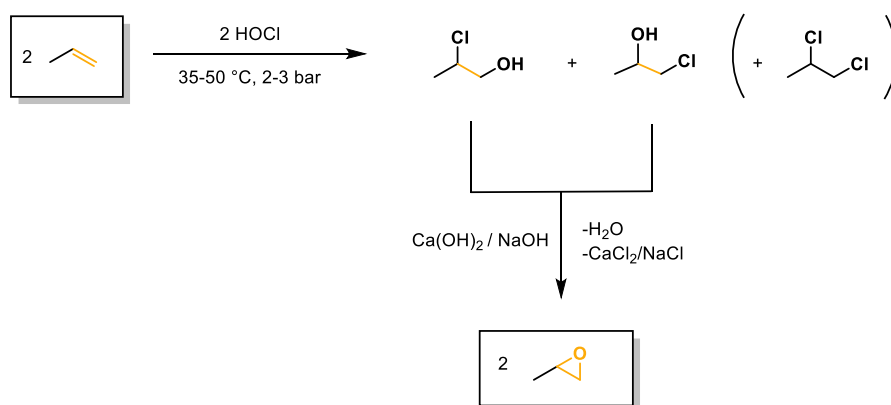
Scheme 2. The chlorohydrin process is illustrated by its two-step reaction using propylene as an example.[30]

The second step includes the *in-situ* dehydrochlorination of the isomers with calcium- or sodium hydroxide at 25 °C to obtain polypropylene and further purification *via* distillation. Propylene oxide is obtained with a selectivity of ca. 90% in reference to the applied propylene.[9, 27, 30] However, as already mentioned, one of the disadvantages is the high chlorine consumption. Furthermore, the chlorohydrin process generates unwanted side products, such as 1,2-chloropropane and chloride salts, and an enormous effort has to be made to treat the brine solution because of the high wastewater load.[30, 31] Therefore, alternative routes were developed involving direct oxidation with organic hydroperoxides as oxidants and various high-valent TM catalysts, such as MoO_3 or $Mo(CO)_6$.[36] Although molybdenum catalysts utilizing TBHP (*tert*-butyl hydroperoxide) show high activity and selectivity, they depict some major disadvantages

2

since molybdenum is considered toxic and TBHP is more expensive.[37, 38] However, a significant breakthrough was achieved by *Enichem* in 1983 with the introduction of a titanium-substituted silicalite-1 (TS-1) catalyst. This innovation enabled liquid-phase oxidation and the use of hydrogen peroxide as a more environmentally friendly and cost-effective oxidizing agent compared to TBHP.[9, 39-41] By implanting this innovation, *Evonik, EniChem*, *Dow*, and *BASF* developed the HPPO (hydrogen peroxide to propylene oxide) industrial state-of-the-art process (Scheme 3), in which propylene is oxidized in methanol in the presence of the catalyst TS-1 and hydrogen peroxide.[9, 30, 31]

$$\text{propylene} \xrightarrow[\text{40 °C, 1 atm, (MeOH)}]{H_2O_2, \text{[TS-1]}} \text{propylene oxide} \; + \; H_2O$$
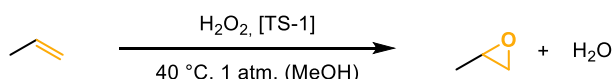
Scheme 3. Depiction of the HPPO process using hydrogen peroxide and TS-1 catalyst to oxidize propylene.[30]

1.1.2. Homogenous Olefin Epoxidation Catalysis

In contrast to heterogeneous epoxidation catalysts, homogenous catalysts are considerably less prevalent in the industry, as the metal precursors are usually expensive, and the synthesis of the respective catalysis may include multiple steps. In addition, homogenous catalysts are generally very difficult to separate and can rarely be reused due to low stability. However, in terms of activity, selectivity, and tolerance, they are superior compared to heterogeneous systems.[9, 42-45]

Therefore, such catalysts are mainly used in the chemical industry for fine chemicals, fragrances, and pharmaceutical products, which are comparably expensive (Figure 2). Furthermore, the defined structure of homogeneous catalysts allows for easier mechanistic investigations compared to heterogeneous catalysts.[46-49]

Mensacarin
antibiotic

Inadvir
HIV protease inhibitor

β-Ionone epoxide
fragrance

AZD-4818
CCR1 antagonist

BRL 55834
potassium channel activator

CDP840
PDE IV Inhibitor
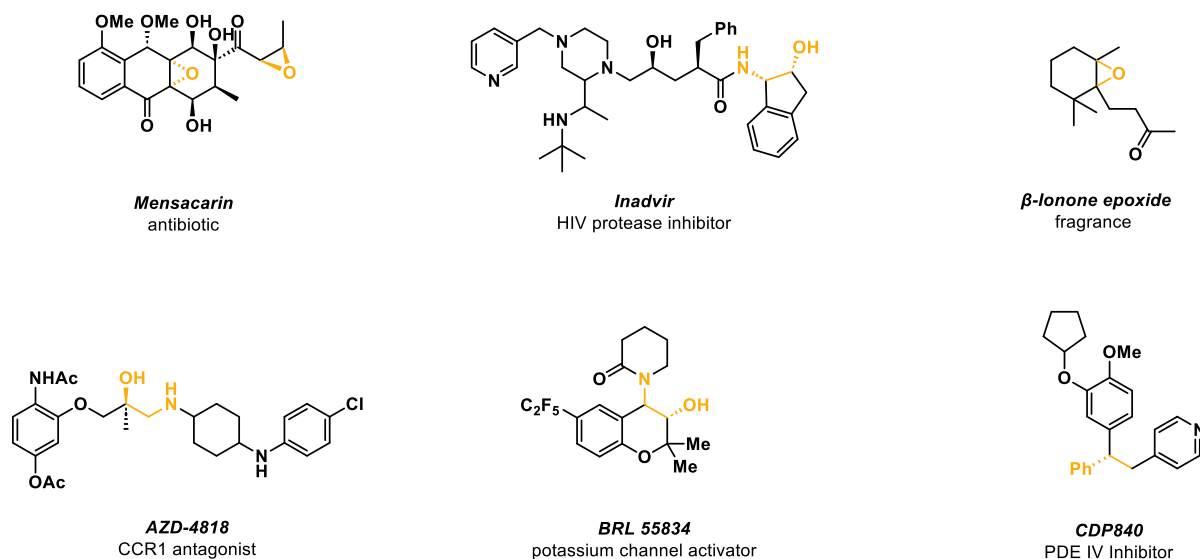
Figure 2. Selection of epoxides of fragrances, antibiotics, and pharmaceuticals containing epoxides (marked yellow) in the synthesis stage.[50-54]

Pioneers such as *Sharpless*[55, 56], *Kochi*[55, 57] *Jacobsen*[58, 59], *Katsuki*[60, 61], *Herrmann*[62, 63], and *Espenson*[64, 65] have significantly advanced the field of homogeneous epoxidation catalysis. Notably, *Sharpless's* groundbreaking method of epoxidizing allyl alcohol with over 90% enantiomeric excess earned him the Nobel Prize in chemistry in 2001, highlighting his contribution to asymmetric homogenous epoxidation catalysis.[55, 56]

[Ti(tartrate)(OR)$_2$]$_2$
Sharpless

[Mn(salen)Cl]
Kochi, Jacobsen, Katsuki

[MeReO$_3$], MTO
Espenson, Herrmann
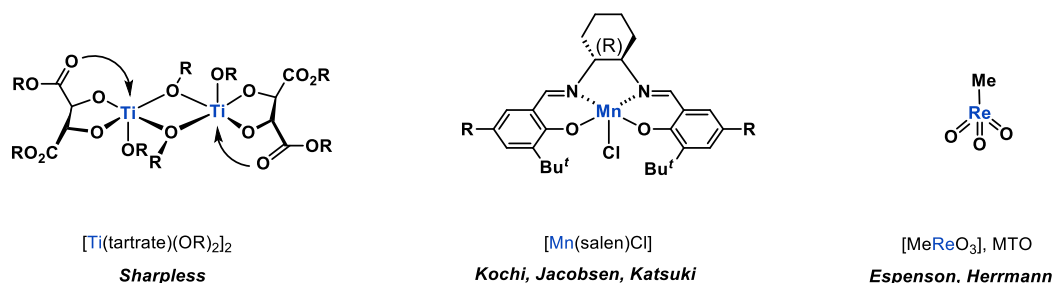
Figure 3. Chemical structures of important epoxidation catalysts studied by *Sharpless*[55, 56] (left), *Kochi, Jacobsen, Katsuki*[55, 57, 59] (middle), *Espenson, and Herrmann*[62-65] (right).

Another proven epoxidation catalyst is methyltrioxorhenium (MTO), which was first synthesized in 1978 by *Beattie* and *Jones* and later applied by *Herrmann* and *Espenson.* It has great versatility as a catalyst for oxidation catalysis.[63, 65-69] However, its broader industrial application has been limited by the high cost of rhenium and the complexity of synthesizing advanced complexes. Moreover, the aforementioned catalysts have primarily been used for relatively simple organic molecule synthesis.[70, 71] Consequently, inspired by nature, research has shifted toward developing more enantioselective, cost-efficient, less toxic, and more environmentally friendly alternatives.[47, 69]

1.1.3. Bioinspired Oxidation Catalysis

In nature, most biological oxidations are commonly achieved with the iron-based heme protein cytochrome P450 (CYP450) oxidase and soluble methane monooxygenase (sMMO).[72-78] One of the key features of those enzymes is their ability to catalyze numerous highly selective oxygen insertions into challenging substrates under mild physiological conditions.

For instance, CYP450 (Figure 4, left) can selectively insert oxygen into C-H bonds of substrates such as alkenes and aromatic compounds. Similarly, sMMO (Figure 4, right) catalyzes the conversion of methane to methanol using atmospheric oxygen.[74, 76, 77, 79]

CYP450   **sMMO**
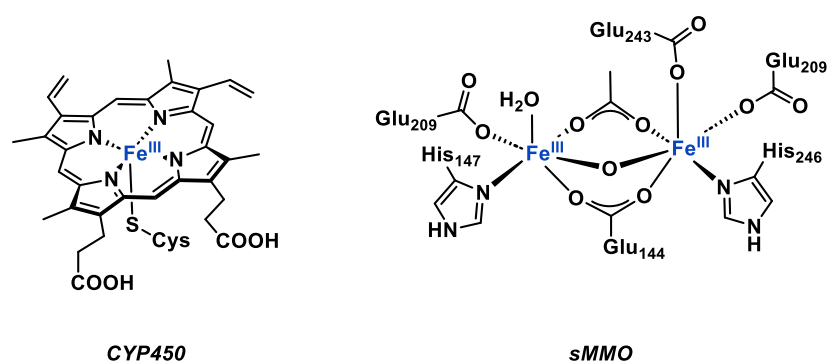
Figure 4. Chemical structures and active sites of CYP450 (left)[77, 80] and sMMO[81, 82] (right).

In the case of CYP450, the active center consists of a heme-B cofactor with a Fe(III) ion. The iron is coordinated by a porphyrin ring, an axial water, and a cysteine residue, which coordinates the heme-iron complex to the protein. The *S*-donor properties of cysteine play a critical role, due to its *trans* effect, in coordinating and subsequently reducing molecular oxygen.[83] The exact mechanism of the oxidation process by CYP450 has been extensively studied over the past decades (Scheme 4).[72, 73, 78, 80, 84-93]
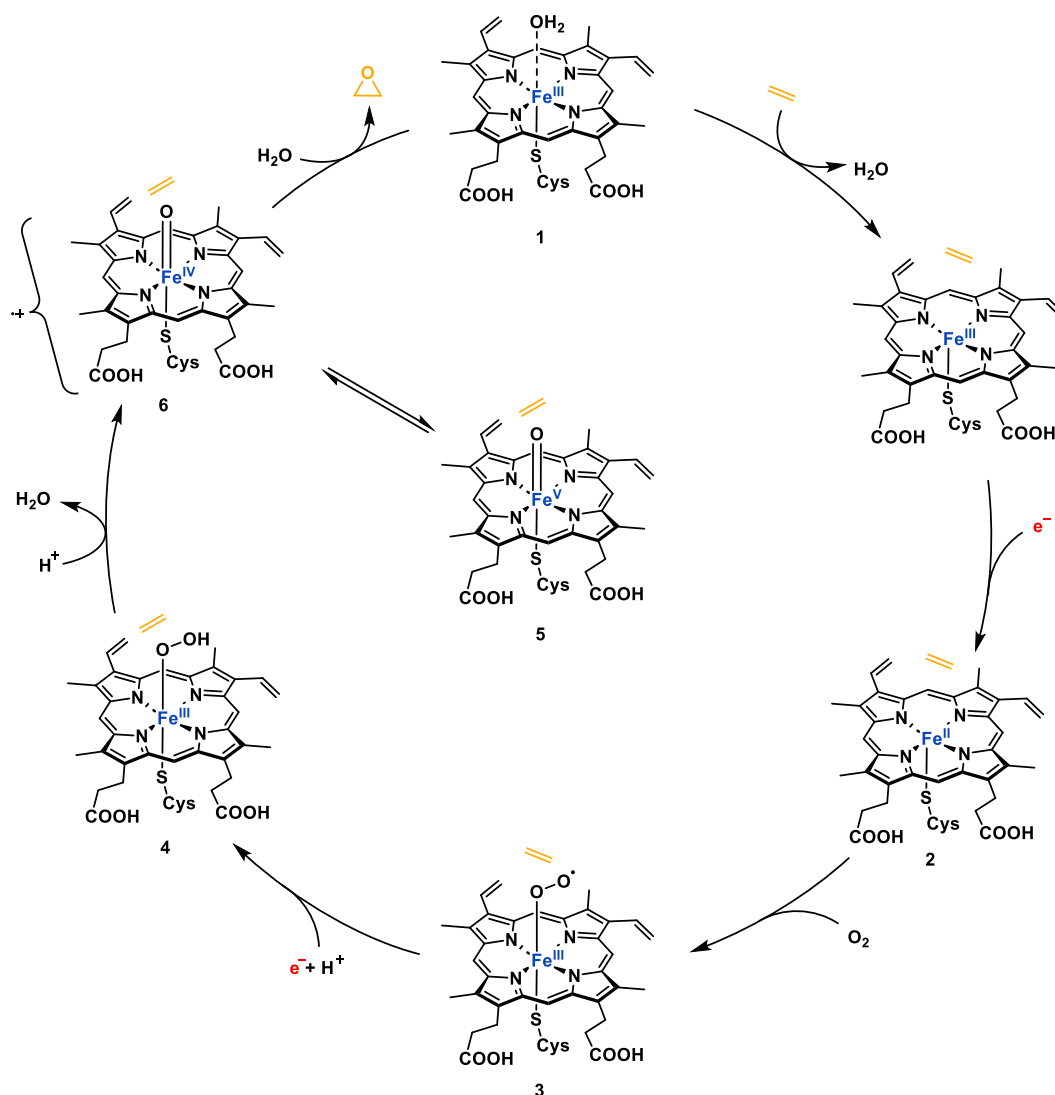
Scheme 4. Simplified scheme of the epoxidation mechanism of cytochrome P450 enzymes utilizing molecular oxygen as oxidant.[72, 73, 78, 80, 84-93]

In the initial phase, the low-spin Fe(III) complex **1** is reduced to the Fe(II) complex **2** *via* a single electron reduction of NADPH by P450 oxidoreductase (POR).[90] Molecular oxygen replaces the labile water ligand and coordinates to the resulting high-spin complex, forming a Fe(III) end-on superoxide species **3** in a formal redox reaction.[73] This species then undergoes another reduction-protonation step, resulting in an end-on η^1-hydroperoxo Fe(III) species **4**.[73] This species can also be formed *via* the "peroxide shunt" pathway by the direct coordination of hydrogen peroxide to the Fe(III) heme complex.[73, 77, 94-96] The subsequent heterolytic cleave of the O-O bond results in the formation of a formal Fe(V) oxo species **5**, which is considered the active species capable of oxygen transfer to an available substrate. In 1979 *Groves* demonstrated with his pioneering work that the species **5** is more accurately described as a Fe(IV) oxo porphyrin radical **6**, due to the stabilization abilities of porphyrin, by decolonization

of the positive charge of the high valent Fe(V) intermediate onto the porphyrin scaffold, resulting in a formal Fe(IV) oxo cationic radical species.[77, 80, 96, 97] In the final step, **6** transfers the oxygen atom to the olefin, forming the epoxide and the initial Fe(III) species **1**.[80, 91-93] This interaction with the ligand system, to alter the metal's oxidation state *via* redox activity plays a vital role in the substrate oxidation and is called non-innocence.[77, 92, 98, 99] Because of this ability, porphyrins were studied in more detail.

The group of *Groves* was the first to develop a bioinspired porphyrin-catalyzed epoxidation model by oxidizing cyclohexene **7** to the corresponding epoxide **8** with an iron tetrakis(phenyl)porphyrin (FeTPPCl) **9a** in catalytic amounts and idosylbenzene (PhIO) as the stochiometric oxidant.[100] However, the system lacked utility, based on the average yield (49%) and the large excess of substrate used. An assumption was that the efficiency of catalyst **9a** decreased due to oxidative degradation.[101]
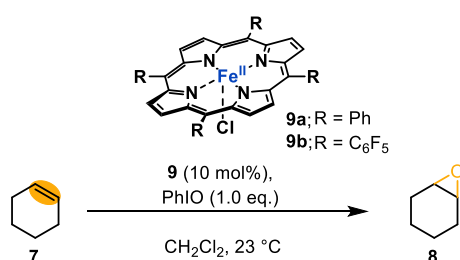
Scheme 5. Oxidation of cyclohexene **7** to the epoxide **8** with bioinspired porphyrin catalysts **9a/b**.[100, 101]

Chang managed to identify the problem as irreversible oxidation of the porphyrin, which results in the observed deactivation of the catalyst.[102] By introducing pentafluorophenyl groups (**9b**) at the *meso*-position of the porphyrin ring, *Chang* was able to increase the yield of *Groves* model reaction up to 95%.[101]

It was postulated that decreasing the electron density in the porphyrin ligand would enhance the electrophilicity of the reactive oxo iron (IV) species and the reactivity, resulting in a higher yield and prolonging the respective catalyst's life span.[103] Therefore, different variations with electron-donating (EDG) and electron-withdrawing groups (EWG), such as tetramesitylporphyrin (TMP, EDG) and 2,6-difluorphenylporphyrin (DFPP, EWG), in the *meso*-position of the porphyrin ring were synthesized. The resulting influence on the catalytic reactivity was studied in an effort to understand the electronic effects of porphyrins on the chemical properties of the Fe-oxo intermediates.[86, 104-107] The results indicated that the catalytic activity increased by introducing EWGs, and the oxidizing power of the Fe-oxo complex could be controlled by modifying the electronic system of the porphyrin ligand (Figure 5).[105, 106, 108]
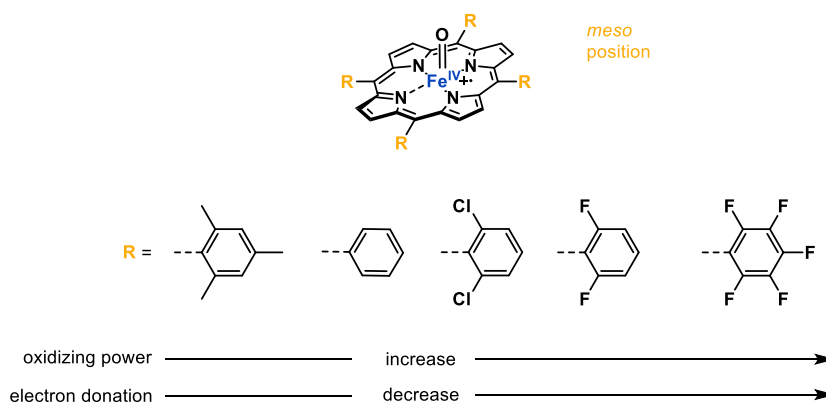
Figure 5. Possible modifications of the meso-position and its stereo-electronic influence on the catalytic reaction progression.[107]

Inspired by the reactivity, selectivity, and essential role of porphyrins in biological systems- such as photosynthesis and oxygen transport- a lot of resources have been invested in developing biomimetic iron catalysts over the past decades.[86, 104-107, 109-111] The resulting biomimetic iron catalysts are divided into heme and non-heme complexes.[107] Heme catalysts are modified compounds that are based on porphyrin ligands, while non-heme catalysts are based on tetradentate *N*-, *O*-, *C*-, or *S*-donors.[107, 112-117]

1.1.4. Non-Heme-Iron Catalysts

Iron complexes with *N*-donors have been widely studied for their catalytic applications and reaction mechanisms. Commonly used *N*-donors include amines, pyridines, and pyrrolidines, and so far, a variety of tetra *N*-donor ligands, such as cyclam, TPEN, TMC, and TPM, have been employed in non-heme iron complexes.[112, 118, 119] One of the first non-heme iron epoxidation catalysts [Figure 6, (Fe^{III})$_2$PBATA(OAc)$_2$] was reported by *Que* in 1986, which is inspired by the sMMO subunit.[120] In 1991 *Nam* reported the first epoxidation catalyst with a single iron center utilizing the cyclam ligand system [Figure 6, *trans*-Fe^{II}(cyclam)].[121]

Over the decades, numerous non-heme iron complexes have been synthesized to explore their structure-reactivity relationships. *Que*, *Costas*, *White*, *Nam*, and *Valentine* have extensively studied the mechanism of these complexes, which was found to be somewhat similar to CYP450.[113, 121-125]
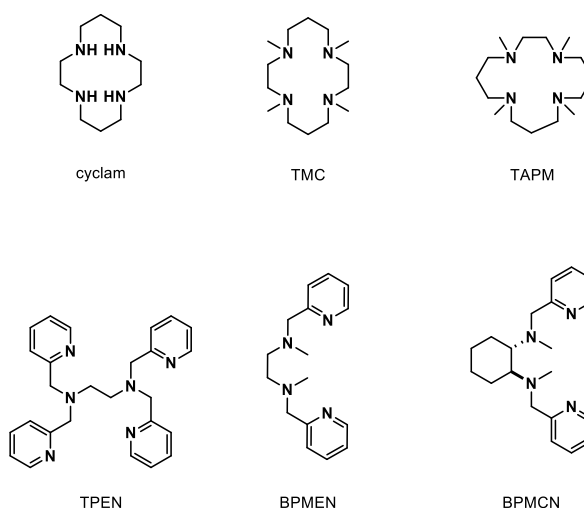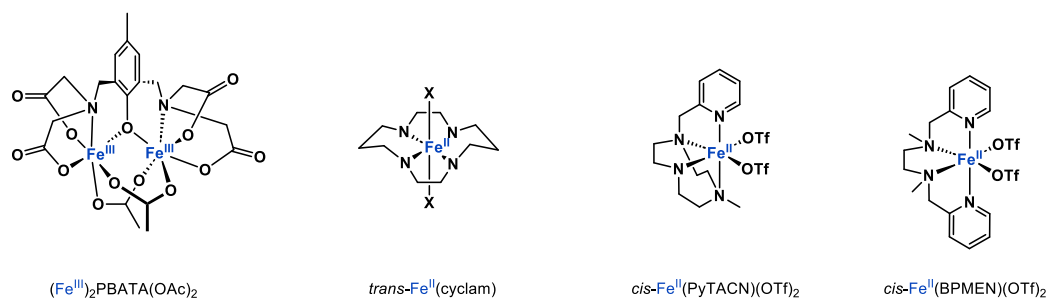
Figure 6. Chemical structure of non-heme iron catalysts for oxidation reactions (top) and various ligands for non-heme complexes (bottom).[107, 112, 117, 120, 121, 126]

However, despite the immense effort, the mechanism remains partially understood, and non-heme iron catalysts still fall short in terms of efficiency and stability under oxidative conditions compared to the enzymes they are supposed to mimic or Mo, and Re-based complexes.[112]

In recent years, *N*-heterocyclic carbenes (NHCs) have emerged as a promising alternative to the widely studied and applied *N*-donating ligands.[127, 128] In 2012, *Kühn* reported an iron-based oxidation catalyst that demonstrated significantly better performance than purely *N*-donor ligand-based catalysts. For example, while the *cis*-Fe^{II}(BPMEN)(OTf$_2$) catalyst (Figure 6) achieves a turnover frequency (TOF) of only 17 h^{-1} and a turnover number (TON) of 8.4, in the epoxidation of *cis*-cyclooctene, the NHC-based catalyst **10** (Figure 7) achieved a TOF of 800 h^{-1} and a TON of 50, even without additives.[125, 129, 130] Subsequent iron catalysts **11a** and **11b**, employing a 16-membered macrocyclic tetra-NHC ligand, achieved even greater results, with initial TOFs of 50 000 h^{-1} for **11a** and up to 183.000 h^{-1} for **11b** with a selectivity of 99% in the same model epoxidation reaction, even outperforming MTO in terms of activity.[131, 132] However the stability of those catalysts is nowhere near optimized as Mo- and Re-based catalysts.[69] To overcome the stability issues, *Kühn's* group modified the macrocyclic structure by adjusting the electron-donating ability of the ligand. A comparative catalytic study of the resulting iron catalysts **12** and **13** was conducted. The results revealed that decreasing the electron density

9

improved the stability of the respective iron complex; however, this came at the cost of reduced oxidative catalytic activity and *vice versa*.[133]

Nevertheless, the remarkable performance improvement of **10-13** compared to traditional non-heme catalysts with purely N-donor ligands underlines the potential of NHCs as highly promising ligands for homogeneous catalytic applications.[112]
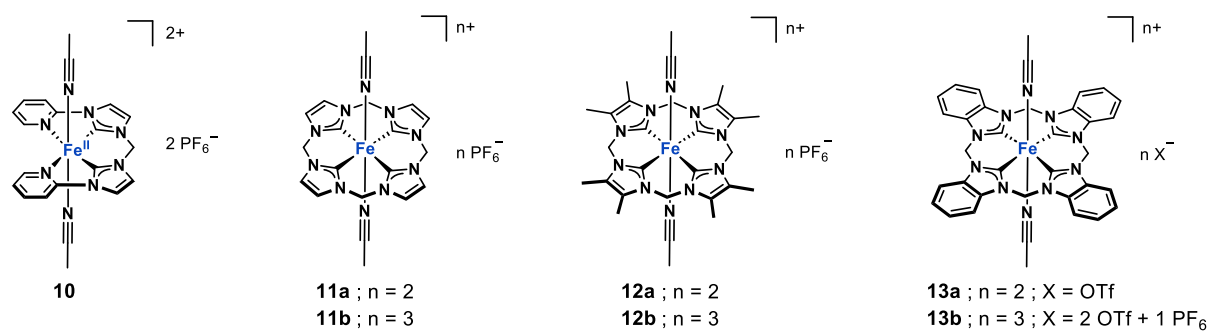
Figure 7. Structures of *Kühn's* iron oxidation catalysts based on NHCs.[129, 131, 133]

1.2.   *N*-Heterocyclic Carbene Ligands

In the 1960s, *Öfele* and *Wanzlick* discovered a new class of *N*-heterocyclic carbene (NHC) compounds.[134, 135] In contrast to *Fischer* and *Schrock* carbenes, which found wide applications as ligands in catalysis and organic synthesis, these compounds were to that date considered mere "lab curiosities".[136, 137] *Schrock* was also awarded the Nobel Prize in 2005 in chemistry for olefin metathesis with transition metal carbene complexes.[138, 139]
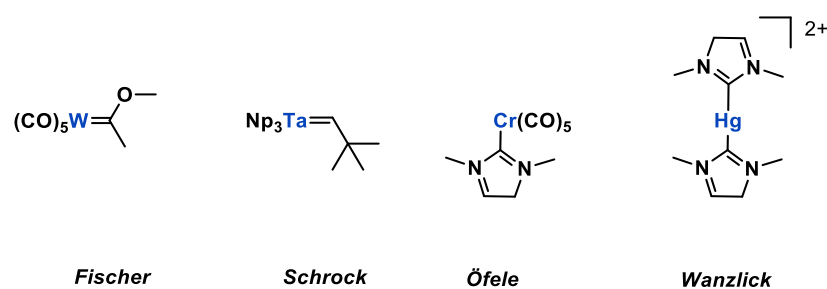
Figure 8. Structures of different carbene complex types.[134-136, 140]

Approximately 30 years later in 1991 *Arduengo et al.* published the first stable, isolated free NHC with two sterically demanding adamantly wingtips.[141] Prior to that, NHCs were considered to be highly reactive, unstable, and not isolatable due to the fact that they tend to dimerize (*Wanzlick* equilibrium).[142] Since *Ardueongo's* report, this class of compounds has emerged as extremely important ligands in organometallic chemistry.[143, 144]
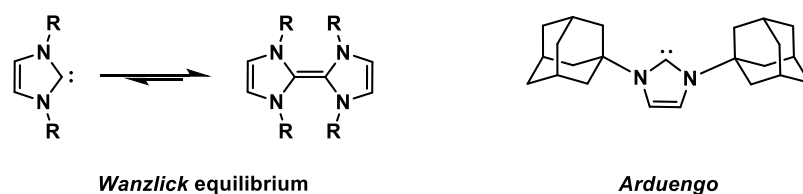
Figure 9. Wanzlick equilibrium (left) and first published free NHC published by Arduengo (right).[143, 144]

NHCs are defined as heterocyclic species containing a carbene carbon and at least one nitrogen atom within the ring structure.[145] In contrast to classical carbenes, NHCs have a singlet ground state electronic configuration with the highest occupied molecular orbital (HOMO) and the lowest unoccupied molecular orbital (LUMO), best described as a formally sp^2-hybridized lone pair and an unoccupied *p*-orbital at the carbene carbon atom.[145-147] The adjacent nitrogen atoms donate their free π-electrons to the unoccupied *p*-orbital, while at the same time withdrawing electron density on the σ-level due to their high electronegativity.[145, 148] This interactions combined are described as +M/-I push-pull effect.[148, 149] The electronic and steric properties can also be fine-tuned by modifying the wingtip- and backbone position of the NHCs.
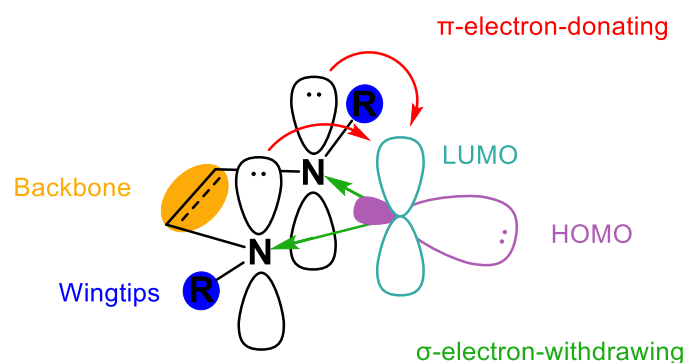
Figure 10. Structural features and modification options of NHCs.

Based on these modification sites, which can support functional groups or other donating moieties, suitable chelating ligands can be developed for catalytic applications.[112, 145, 150] Furthermore, the adjustment of the steric conformation can influence the NHC-metal complexes' stereoselective effect. Introducing an unsaturated backbone can also increase the stability of the NHC by approximately 100 kJ/mol due to partial aromaticity, thereby reducing the need for bulky steric wingtips for stabilization.[145, 151, 152] On the other hand, when a saturated backbone is introduced, electron density becomes concentrated on the C2 carbene carbon due to the lack of π-interactions, increasing the carbene's basicity. As a result, saturated NHCs are slightly stronger σ-donor ligands than their unsaturated counterparts.

NHCs are also valuable alternatives to phosphines, which they are often compared to.[147, 153-155] However, NHCs are significantly stronger σ-donors and do not dissociate from the metal as easily as phosphines often do.[145, 146, 155]

1.2.1. Electronic Properties Determination of NHCs

One of the commonly used methods to determine the donating properties of NHC ligands (L) can be expressed by *Huynh's* electronic parameter (HEP), derived from the complexation of the respective ligand (L) in the *trans* position with a Pd(II)-NHC-complex containing a benzimidazolyidene spectator ligand, which results in a *trans*-[PdBr$_2$(^{i}Pr$_2$-bimy)L] complex (Figure 11).[146, 156, 157]
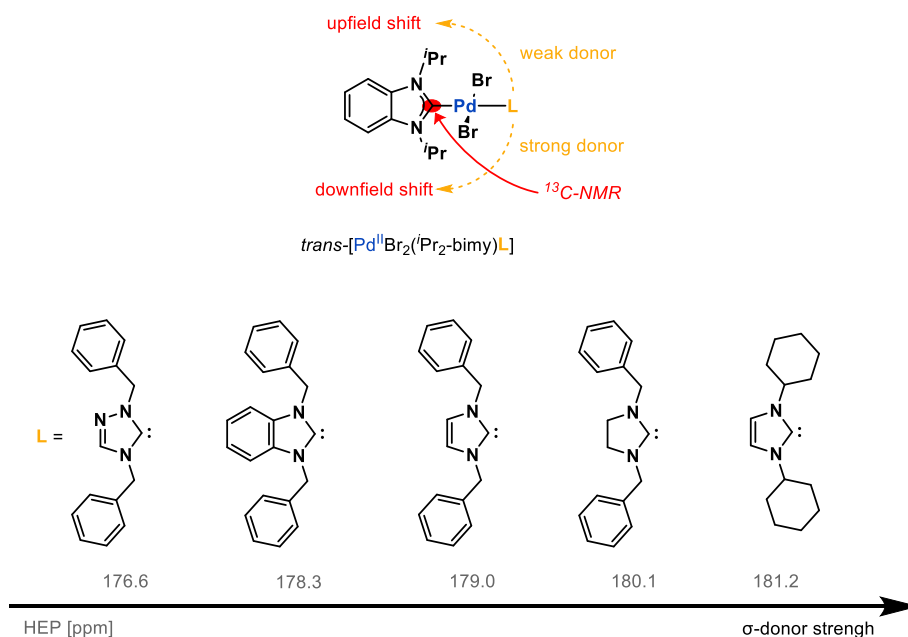
Figure 11. Literature HEP values of some ligands. The stronger the σ-donor strength, the higher the HEP value.[146, 158-160]

The resulting properties of the ligand (L) can be measured *via* the ^{13}C-NMR shift of the carbene carbon signal of the spectator ligand. A strong electron-donating ligand increases the so-called "free carbene" character of the benzimidazolyidene spectator ligand, which leads to a downfield shift of its ^{13}C$_{NHC}$ signal. When a weak electron-donating ligand is applied, the ^{13}C$_{NHC}$ signal of the benzimidazolyidene spectator ligand will stay rather upfield shifted.[146, 149, 157] These shifts are the HEP values and primarily describe the σ-donating ability of the ligand.[146, 161] Furthermore, this principle can also be used for linear Au(I)-NHC complexes, which are in good correlation to the obtained HEP values from the Pd(II)-NHC-complex.[162]

An alternative is the *Tolman* electronic parameter (TEP), derived from the CO stretching frequencies obtained by infrared (IR) vibrational spectroscopy in *cis*-[RhCl(L)(CO$_2$)] (Figure 12) or [Ni(L)(CO)$_3$], which was originally developed for phosphanes but can be used to determine the electron donating ability of NHC ligands in transition metal carbonyl complexes.[146, 163] However, the TEP value only gives information about the net electron density at the metal

center without separating σ-donation from π-interactions.[158, 164] This method has also its limitations and needs to be complemented by ^{77}Se-NMR spectroscopic and computational methods to validate the results.[165, 166]

cis-[Rh^{I}Cl(CO)$_2$L]

L =

| 2070 | 2050 | 2040 | 2037 | 2036 |

TEP [cm^{-1}]   electron donation strength
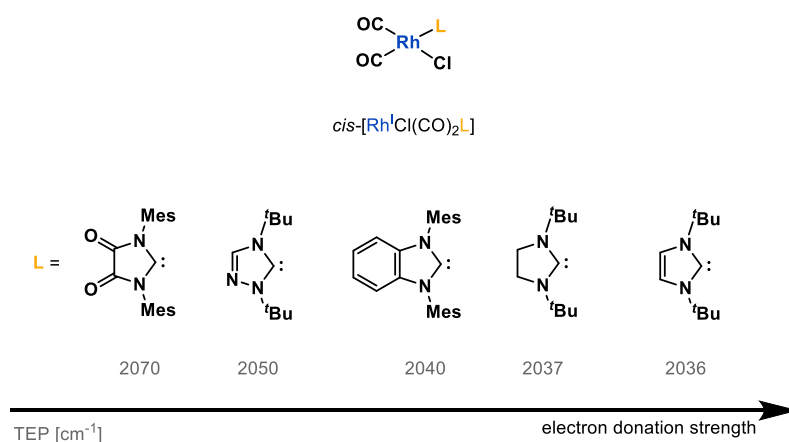
Figure 12. Literature calculated TEP values for *cis*-[RhCl(CO)$_2$L] in CH$_2$Cl$_2$.[146, 157, 158, 167, 168]

In addition to the above-mentioned methods, electrochemical measurements can be conducted to determine the redox potential of metal complexes, which their surrounding ligands can influence. Strong electron-donating ligands facilitate the oxidation of the metal, lowering the redox potential. On the other hand, weak electron-donating or strong accepting ligands increase the redox potential of the respective complex. The electrochemical parameter called *Lever* electronic parameter (LEP) can be determined by measuring the redox potential of *cis*-[MCl(COD)L] (M = Rh or Ir, COD = 1,5-cyclooctadiene) with the respective ligands.[146, 169, 170]

cis-[Rh^{I}Cl(COD)L]

L =

| +0.833 | +0.791 | +0.773/0.875 | +0.683 | + 0.58 |

E$_{1/2}$ [V]

weak electron donation   strong electron donation
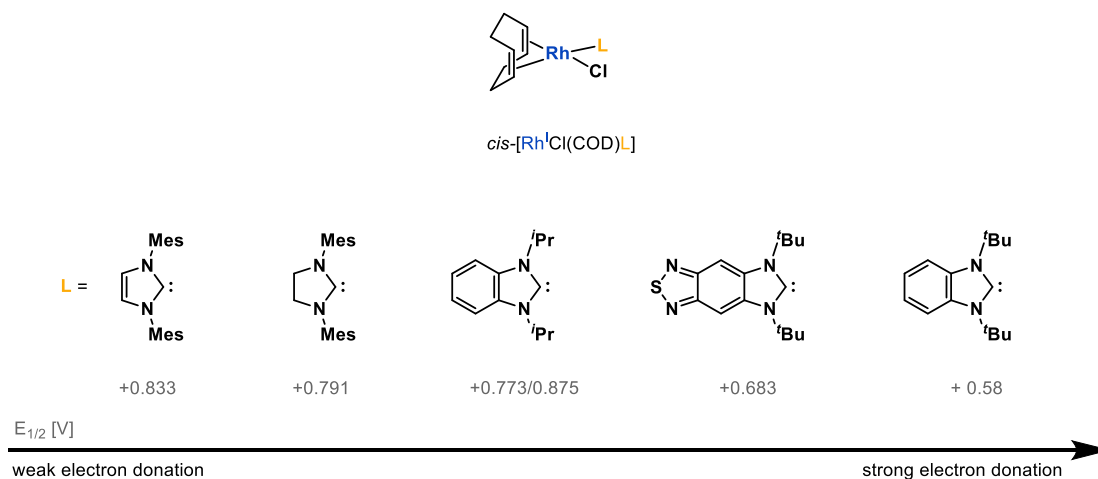
Figure 13. Literature redox potentials of *cis*-[RhCl(COD)L] complexes in CH$_2$Cl$_2$ with Bu$_4$NPF$_6$ as electrolyte.[146]

14

1.2.2. Synthesis of NHC Ligands

NHCs are commonly synthesized from their corresponding imidazolium salts, which can be obtained either by condensation reactions (route **I**) or S_N2 reactions (route **II**) (Scheme 6).[171, 172] This allows for various ligand precursors, which can subsequently be converted into transition metal-NHC complexes *via* different synthetic routes (route **III-VII**) (Scheme 7), such as the transmetalation route (**III**), where Ag_2O is used as an internal base and generates an *in situ* Ag(I) complex. The Ag(I) complexes can subsequently be treated with a metal precursor bearing a halide, which results in the precipitation of insoluble silver halide and the respective NHC complex. An alternative route (**IV**) is the direct metalation of the *in situ* generated carbene using a weak base, such as NaOAc, followed by the formation of the metal-NHC complex. Less commonly employed routes include complex formation *via* the *Wanzlick*-type-dimer (**V**), α-elimination (**VI**), or the reduction of thione with potassium, followed by the NHC complex formation with the respective metal precursor (**VII**).[173-177]

R,R' = wingtip; X = halide, PF_6, OTf …..
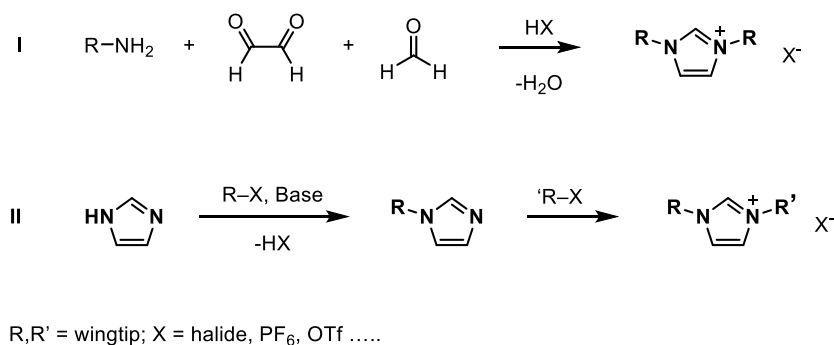
Scheme 6. Synthetic routes (**I**, **II**) for obtaining common NHC precursors *via* condensation (**I**) and alkylation (**II**).[171, 172]
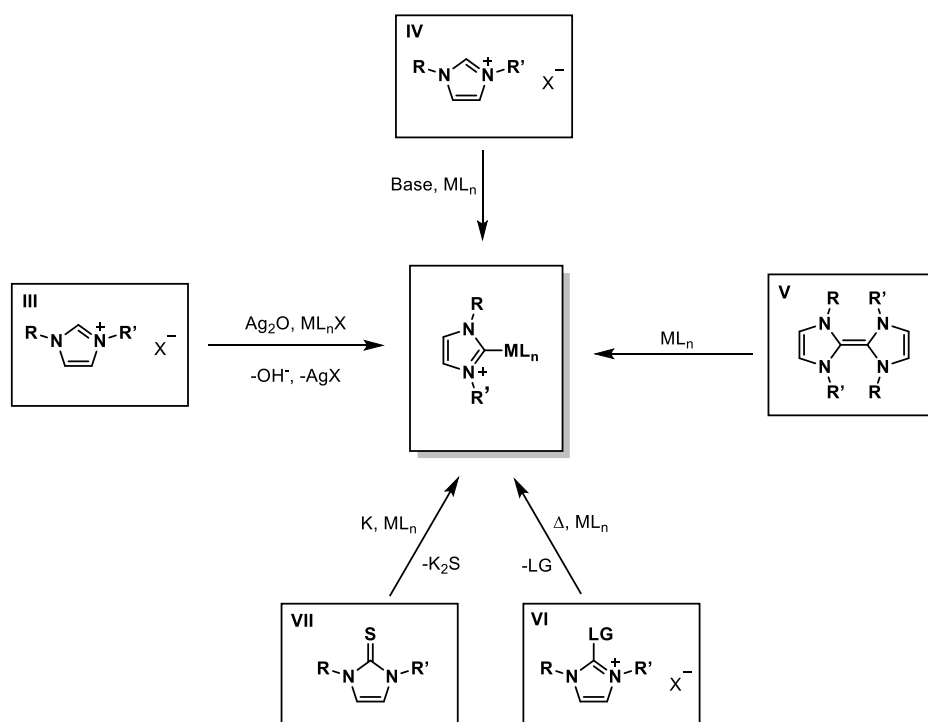
R,R' = wingtip; LG = leaving group; X = halide, PF$_6$, OTf …..

Scheme 7. Common synthetic approaches to transition metal NHC complexes with Ag$_2$O as an external base followed by transmetalation (**III**), complex formation *via* Wanzlick-type-dimer (**IV**), external base (**V**), thermal leaving group (LG) followed by complex formation *via* the free carbene (**VI**), *in situ* reduction of thiourea followed by formation of the transition metal NHC complexes (**VII**).[173-177]

In recent years, progress in this field has shifted from complexes with mono- or bidentate NHC ligands to multidentate ligands with enhanced chelating activity. Particular emphasis has been placed on developing acyclic or macrocyclic tetradentate ligand motifs to enable comparisons with the corresponding class of pure *N*-donor non-heme complexes.[178]

In 2002, *Baker et al.* synthesized the first macrocyclic Ni(II) carbene complex (**14**), which incorporates two NHC units as *C*-donors and two pyridine units as *N*-donors.[179] Three years later, *Hahn et al.* published the first macrocyclic Pt(II) tetra-NHC complex (**15**).[180] However, *Murphy et al.* recognized that the inherent stability of the complex **15** made further transition metalation reactions impossible. In 2007, *Murphy*'s group synthesized a ligand precursor containing four imidazole units bridged by propane, and the resulting complexes showed that the macrocyclic NHC ligand coordinated two metal atoms. Subsequent experiments led to the successful synthesis of a Pd(II) complex (**16**) coordinated by all four NHC units.[181]

In 2011, *Jenkins et al.* reported the first macrocyclic tetra-NHC iron complex (**17**) and investigated its ability to catalyze the aziridination of olefins by aryl azides.[182] In 2013, *Meyer et al.* achieved the first isolation and characterization of an Fe(IV)-oxo species using a macrocyclic tetra-NHC ligand (**18**). This breakthrough highlighted the ability of this ligand class to stabilize

highly valent iron-oxo species and also the possibility that these NHC complexes can be used for oxidation catalysis.[183]
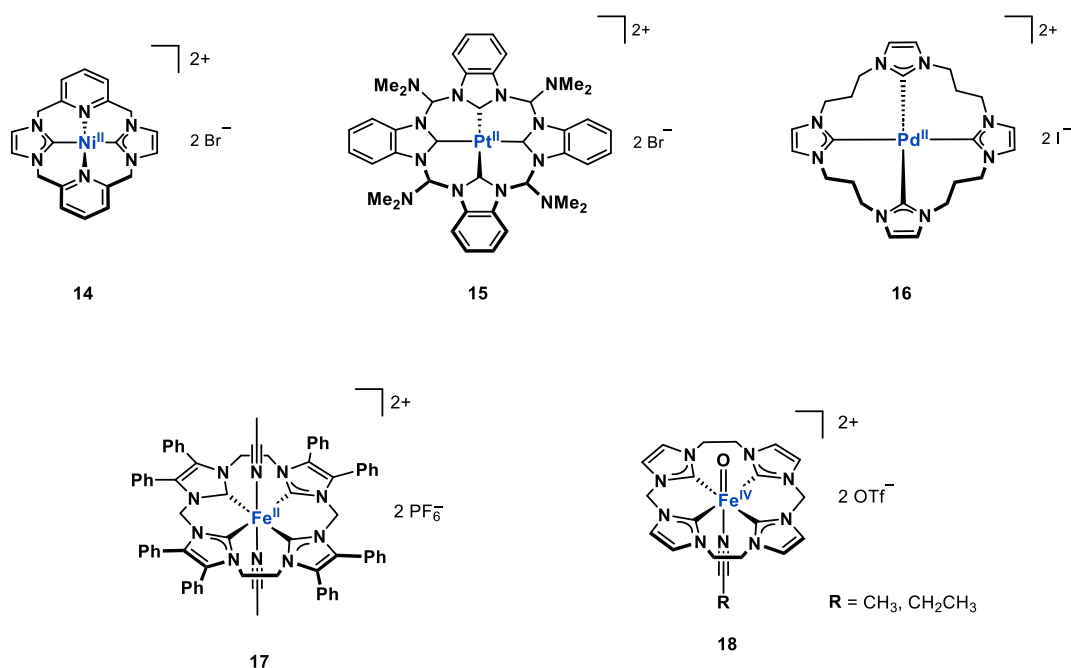
Figure 14: Structural overview of different NHC complexes reported by *Baker et al.* (**14**), *Hahn et al.* (**15**), *Murphy et al.* (**16**), *Jenkins et al.* (**17**), and *Meyer et al.* (**18**).[179-183]

In the following years, *Kühn's* group advanced the field by developing Fe(II) and Fe(III) catalysts using 16-membered macrocyclic tetra-NHC ligands (Figure 7).[131-133, 184] Additionally, they reported various group 10 and 11 metal NHC complexes with the same ligands (Figure 15), investigating their antiproliferative activity and selectivity against cancer cells.[185, 186]
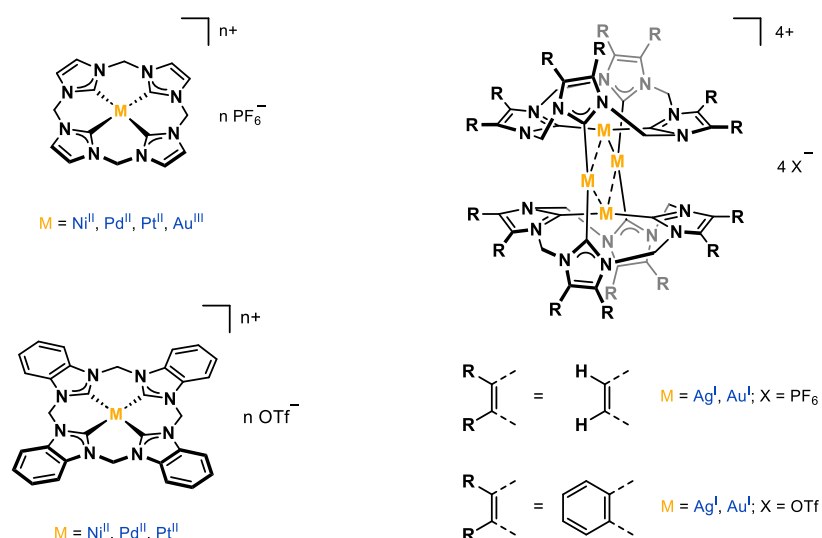
Figure 15. Structural overview of group 10 and 11 NHC complexes reported by *Kühn et al.*.[185, 186]

1.3. Medicinal Chemistry

1.3.1. Chemotherapy and its Challenges

In 2022, there were an estimated 20 million new cancer cases and 9.7 million deaths, according to the World Health Organization (WHO).[187] Cancer, in general, is defined as uncontrollable cell growth resulting in malignant tumors capable of invading nearby tissues.[188-192] The concept of tumor formation involves a multistep process of genetic alteration in healthy cells, giving mutated cells an advantage in terms of proliferation and selective survival. However, despite the significant advancements in cancer research, the exact mechanisms of tumor formation, known as tumorigenesis, remain not fully understood.[193, 194] According to *Hanahan* and *Weinberg*, two key characteristics drive cancer evolution: genomic instability, which leads to genetic diversity and mutations, and the adaptation of cancer cells to evade the body's immune response.[190, 191] Common types of cancer include lung-, breast-, colorectum-, prostate- and stomach-cancer.[195]

Besides radiotherapy, a common treatment of cancer often involves chemotherapy, which is frequently combined with surgery. This therapy employs highly potent cytotoxic agents to target and eliminate rapidly proliferating cancer cells.[196-200] For instance, some agents disrupt the integrity of cell membranes (necrosis), causing the cell to rupture and release its cytoplasm, potentially inducing inflammation in surrounding tissues (autophagy). In contrast, others induce the desired programmed cell death (apoptosis).[201] While there are several ways to kill cancerous cells, the most commonly studied subclasses of chemotherapy for induced apoptosis include alkylating-, antimetabolites-, anthracyclines- and antimitotic-agents (Scheme 8):[192, 202, 203]
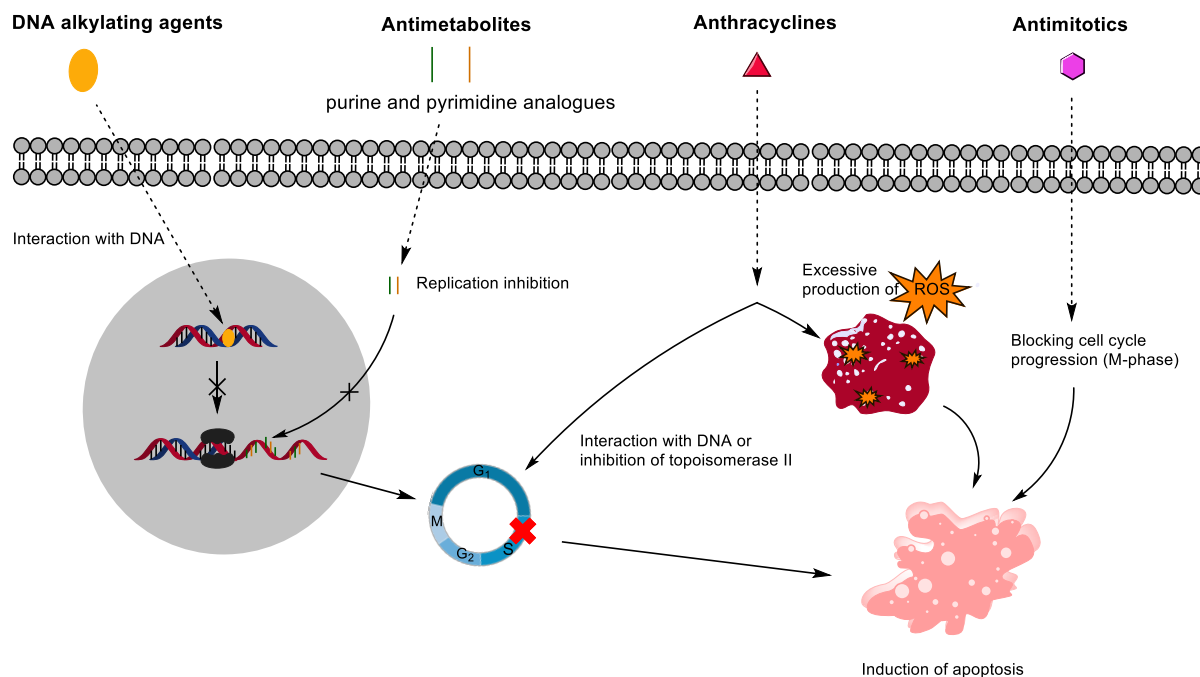
Scheme 8. Simplified representation of the mechanism of action for the main chemotherapy agents used. Including DNA alkylating-, antimetabolite-, anthracycline-, and antimitotic-agents.[203]

- Alkylating agents bind alkyl groups to the N^7-nitrogen atoms of guanine in DNA, preventing replication and leading to cell death.[202] Classic alkylation examples include Cyclophosphamide, Chlormethine or Melphalan (Figure 16).[204-208] Platinum-based drugs like cisplatin and carboplatin, classified as "alkylating-like agents," function similarly by coordinating with the N^7-nitrogen of guanine and thus prevent DNA replication, leading to the inevitable cell death.[209, 210]

- Antimetabolite agents interfere with the cell's metabolic processes by mimicking or inhibiting metabolites essential for DNA synthesis.[211] The most common subclasses include pyrimidine- and purine-analogs:

    Pyrimidine analogs mimic natural pyrimidines and interfere with DNA production, e.g., Cytarabine (Figure 16).[212]

    Purine analogs disrupt the synthesis of purine nucleotides, leading to defective DNA formation, e.g., Mercaptopurine (Figure 16).[213]

- Anthracycline agents are multifunctional agents that target DNA and disrupt cell processes by several mechanisms.[214] These include the Inhibition of topoisomerase II (manages the topology or physical state of the DNA), DNA intercalation, which blocks replication and transcription, and the generation of reactive oxygen species (ROS).[215] [e.g., Doxorubicin (Figure 16)][216]

- Antimitotic agents specifically disrupt the mitotic phase (M-phase) of the cell cycle by interfering with the microtubule dynamics required for cell division of eukaryotic cells.[217] Examples include Vincristine and Paclitaxel (Figure 16).[217, 218]

Alklylating Agents

Cyclophosphamid
Endoxan

Chlorambucil
Leukeran

Melphalan
Alkeran

Antimetabolite Agents

Cytarabine
Alexan

Mercaptopurin
Puri-Nethol

Anthracycline Agent

Doxorubicin
Adriblastin, Adrimedc

Antimitotic Agents

Vincristine
Oncovin

Paclitaxel
Abraxane
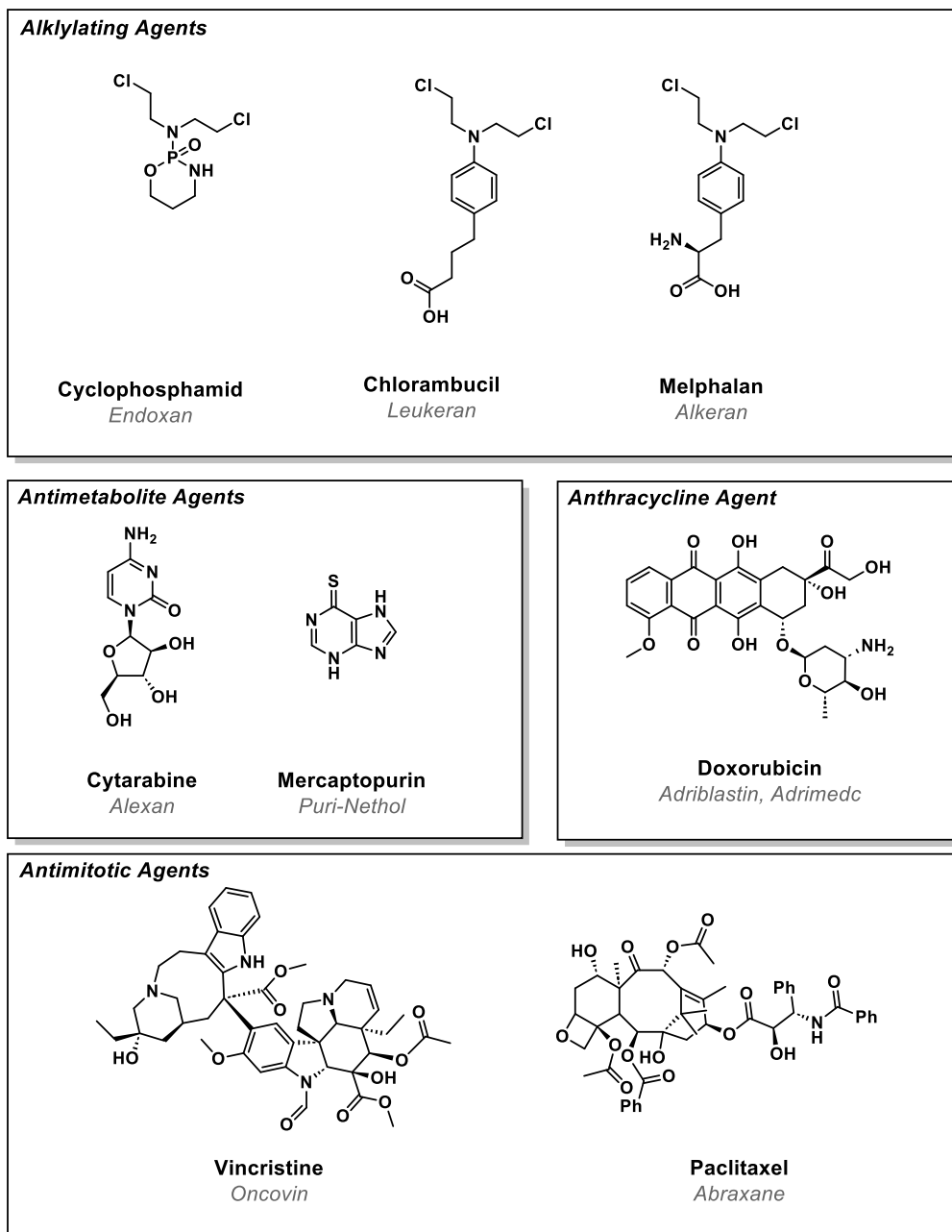
Figure 16. Examples for alkylating-, antimetabolite-, anthracycline-, antimitotic-agents.[203-207, 216-230]

The high reactivity of those cytostatic agents comes with a low selectivity for cancer cells, leading to severe side effects by impacting healthy cells as well. For example, cisplatin, approved by the Food and Drug Administration (FDA) in 1978, can cause nausea, nephrotoxicity, and diarrhea, among other side effects.[231] Prolonged treatments further enable cancer cells to adapt, reducing the effectiveness of cytostatic agents.[232, 233] In addition, classical drug development requires high throughput screening by pharma companies for a certain medical application, which is prone to reproducibility errors and also costly and time-consuming. Therefore, significant effort has been made to design more selective drugs, leading to the development of targeted therapies.[199, 234] This approach involves designing drugs that interact specifically with enzymes, genes, or peptides that are overexpressed or mutated in malignant cells by selectively targeting these molecules while sparing healthy tissues.[199, 235] Three examples of targeted therapy are small molecule inhibitors, monoclonal/conjugated antibodies, and poly(ADP-ribose)-polymerase (PARP) inhibitors.

- Small molecule inhibitors are small molecules designed to penetrate the cell membrane and interact with intracellular targets, such as kinases.[236] For example, Imatinib (Glivec®) inhibits the tyrosine kinase associated with chronic myelogenous leukemia.[237] Additionally, small molecule inhibitors have proven effective against specific mutations in cancer cells such as BRAF (melanoma) or EGFR (lung cancer).[238]

- Monoclonal antibodies cannot cross the cell membrane but can bind to specific receptors on the cell surface. This interaction either blocks signaling pathways or triggers an immune response.[239, 240] A notable example is Trastuzumab (Hereptin®), which targets the overexpressed HER-2 gene in breast cancer.[241] Monoclonal antibodies can also be conjugated with radioactive isotopes (e.g., ^{177}Lu, ^{223}Ra or ^{131}I) or toxic agents to selectively deliver these "payloads" to cancer cells, enhancing the precision of the treatment.[240]

- PARP is an enzyme that repairs single-strand breaks (SSBs) in DNA. If PARP is inhibited, these SSBs accumulate and become double-strand breaks (DSBs) during DNA replication. In "healthy cells," DSBs are repaired by homologous recombination repair pathway (HRR), but in cancer with, e.g., a BRCA1/BRCA2 mutation, this repair pathway is defective, which leads to the accumulation of the damaged DNA, resulting in cell death.[242] Olaparib (Lynparza®) and Niraparib (Zejula®) are examples of PARP inhibitors used for ovarian cancers.[243]
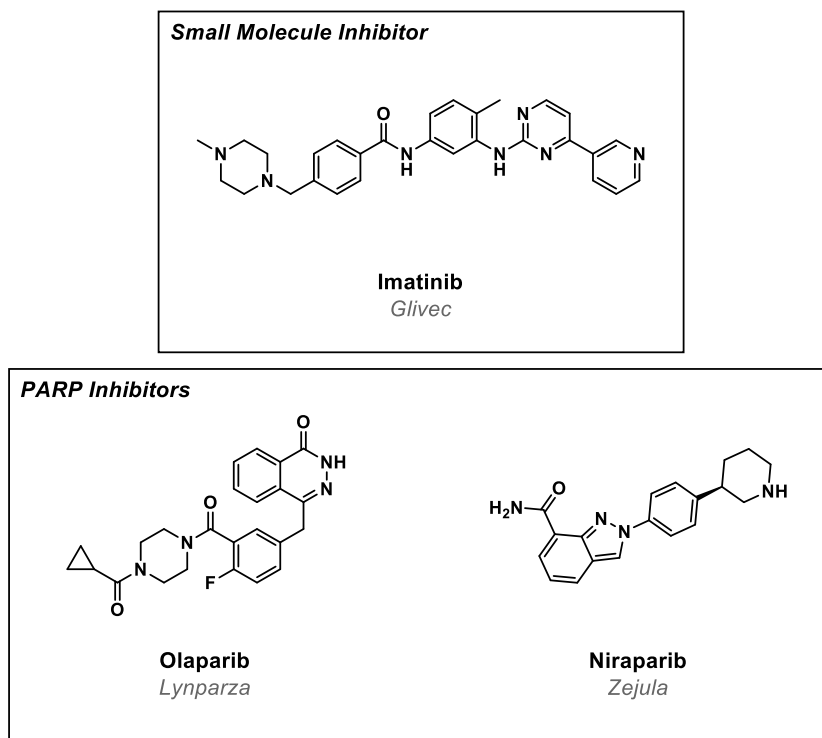
Figure 17: Examples of small molecule and PARP inhibitors.[243, 244]

However, despite these advancements, resistance remains a constant challenge.[196, 245] Consequently, research has also explored alternative strategies, such as the development of new metallodrugs that target distinct mechanisms of action.[246]

1.3.2. Transition Metal NHC Complexes for Potential Anticancer Drugs

One of the most prominent chemotherapeutics known is cisplatin, which is also chemically known as cis-diamminedchloroplatinum(II) and was synthesized in 1844 by *Pyrone*.[247] The antiproliferative activity against *Escherichia coli* (*E. coli*) was accidentally discovered by *Rosenberg* in 1965, and in 1978, cisplatin was approved by the FDA for clinical use.[231, 248-250] Due to the severe side effects of cisplatin and the increasing resistance of cancer cells, several strategies have been explored to address these limitations.

One approach involves the synthesis of platinum-based derivatives, resulting in the development of a wide array of approved platin drugs over the years (Figure 18). Some of the more recent platin drugs, such as Nedplatin, Heptaplatin, Lobaplatin and Dicycloplatin are not worldwide approved.[251-254] However, cisplatin and its derivatives have become less dominant due to resistance and severe side effects.
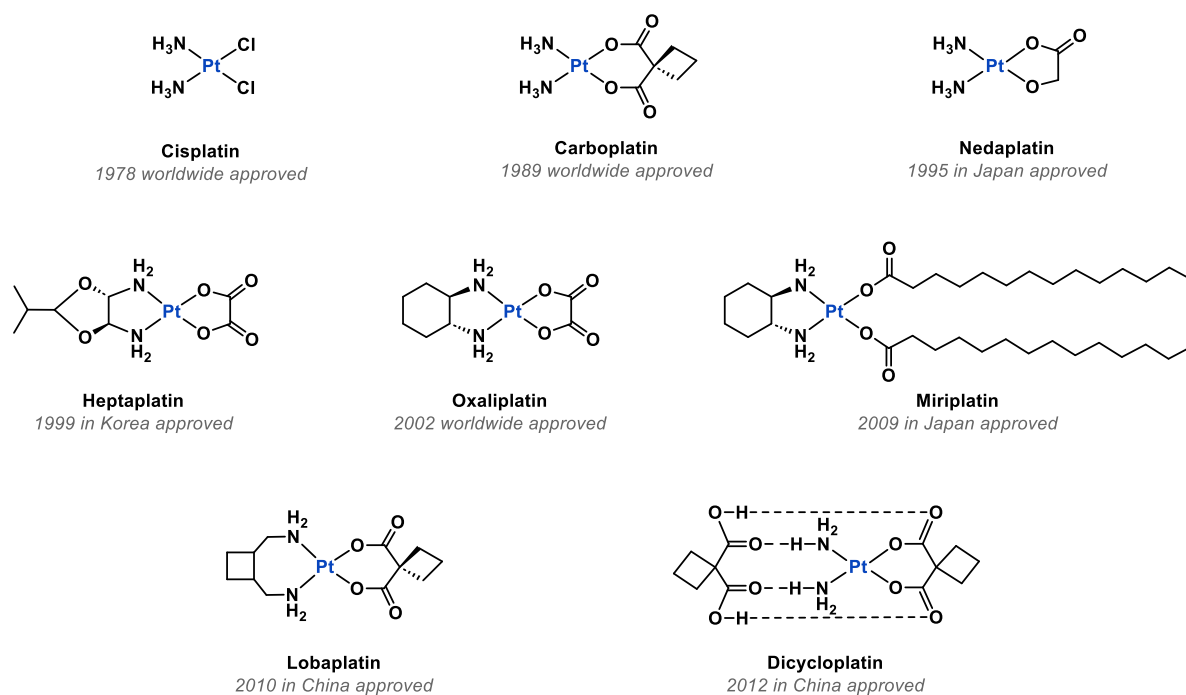
Figure 18. Cisplatin and the main platinum-based drugs, worldwide approved (Cisplatin, Carboplatin and Oxaliplatin) and single nations approved platinum-based drugs (Nedaplatin, Heptaplatin, Miriplatin, Lobaplatin and Dicycloplatin) .[251-256]

Research has also focused on mimicking the electronic properties of Pt(II), prompting investigations into Au(III) for its comparable d^8-configuration and preference for a square-planar geometry. However, Au(III) has been found unsuitable under physiological conditions, as thiols like albumin rapidly reduce it to Au(I).[257, 258]

Further research on Au(I) complexes led to the discovery of Auranofin (Ridaura®)(Figure 19), a linear Au(I) complex approved in 1985 as an orally active antirheumatic agent and has been tested in a phase II clinical study against chronic lymphocytic leukemia.[259, 260] Screening of auranofin also revealed anti-parasitic, anti-bacterial, and anti-viral properties. In 2020, it was also discovered that auranofin "inhibits the novel coronavirus (SARS-COV-2) replication and attenuates inflammation in human cells".[261]
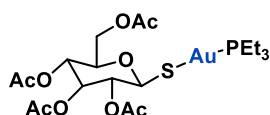
Auranofin
Ridaura

Figure 19. Chemical strucutre of Auranofin (Ridaura®).[259]

Subsequently, the studies on various gold complexes were expanded on the antiproliferative applicability to various cancer cell lines, including cisplatin-resistant cancer cell lines, *in vitro* and *in vivo*.[262-264] Numerous biological studies have shown that most gold compounds form

relatively weak bonds or none with cellular DNA, suggesting a DNA-independent mode of action contrary to cisplatin analogs.[265] This led consequently to a detailed investigation into their mechanism of action.[266-271]

A defining reactivity of gold complexes under physiological conditions bearing at least one labile ligand is their high affinity to thiol and selenol groups. It was discovered that auranofin and its phosphine analogs induce apoptosis primarily *via* a mitochondrial pathway and interact with the enzyme thioredoxin reductase (TrxR), which is overexpressed in cancer cells.[269, 272, 273] TrxR is part of the thioredoxin system, and in total, there are two forms of the system known, TrxR2 and Trx2 (thioredoxin 2), and the cytosolic TxR1 and Trx1, responsible for the formation of reduced disulfide bonds.[269, 270, 274] In addition, Trx acts as an antioxidant by reducing peroxiredoxin (Prx). The thioredoxin system's main purpose is to reduce reactive oxygen species (ROS), like hydrogen peroxide, to harmless water formed in the respiratory chain (Scheme 9).[267, 269-271, 275] By binding to the selenocysteine or cysteine of these proteins, the redox cycles are disrupted, which leads to the accumulation of reactive ROS, leading to apoptosis.[257, 269, 276, 277] The concept of the ROS mechanism is simplified in Scheme 9.
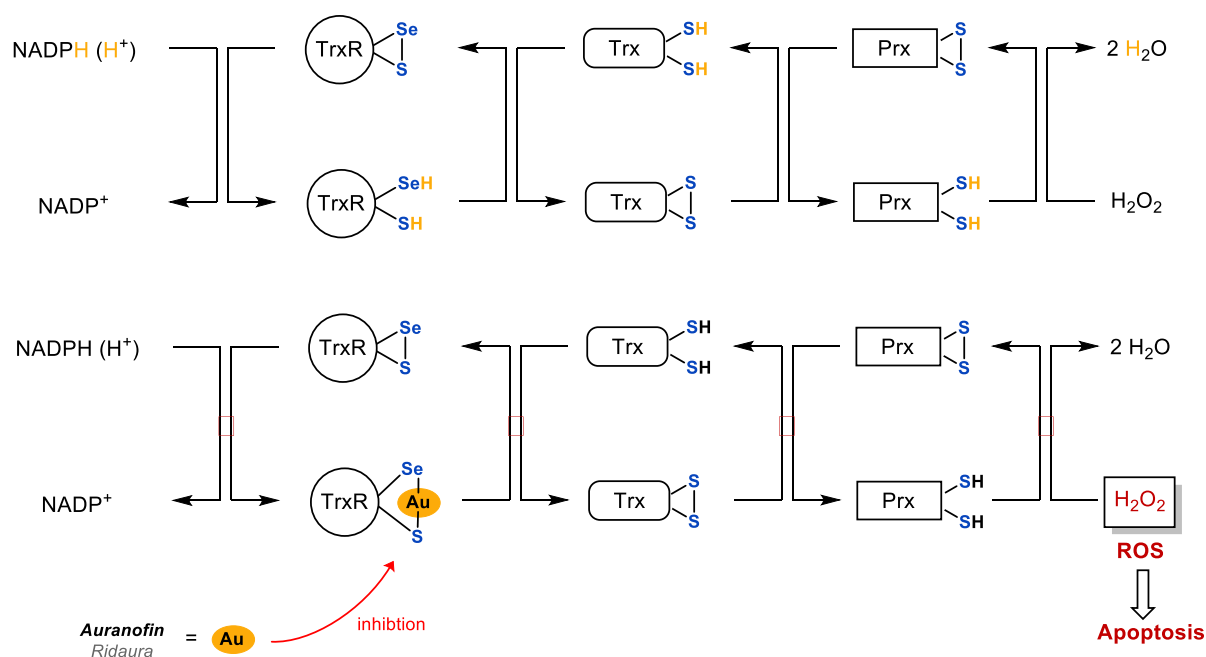
Scheme 9. Concept of the working Trx system (top) and the inhibition with auranofin of the Trx system leading to the accumulation of ROS (bottom).[269, 273]

One major limitation of gold complexes, such as auranofin, is their labile ligands, which can irreversibly bind to transporter proteins like human serum albumin (HSA), or antioxidants such as glutathione (GSH). This deactivation prevents the drug from reaching the malignant cells *in vivo*.[262, 278] The extent of this deactivation is strongly influenced by the stability of the gold complex.[266, 278] Consequently, significant research has been directed toward stabilizing these complexes against premature reactions and finding an optimal balance between reactivity and

stability.[279-281] This balance is crucial, as increased stability against GSH and HAS can also lead to a diminishing targeted interaction with TrxR.[266, 279, 282]

Among the various types of ligands explored, more stable Au(I)-NHC complexes have gained attention as potential anticancer compounds.[278, 283-286] NHC ligands are particularly valuable due to their modular structure, allowing the preparation of wide ligand libraries to determine optimal ligands for electronic- and steric properties and the polarity of the respective complexes.[145] The latter, as reported by *Berners Prize*, plays a crucial role in the cellular uptake through the lyophilic cell membrane, which correlates with the cytotoxicity and the selectivity towards cancer cells compared to non-malignant cells.[287, 288] *Modica-Napolitano et al.* further suggests that the cationic charge and relatively large lipophilic ligands found in these complexes are responsible for a phenomenon referred to as delocalized lipophilic cations (DLCs). Due to the negative membrane potentials, DLCs offer a selectively targeted accumulation of toxic substances in the mitochondria of cancer cells.[289, 290]

However, not all Au(I)-NHC complexes target the mitochondria and the TrxR system. For instance, the caffeine-based Au(I)bis-NHC complex is an efficient and selective DNA quadruplex-interacting agent.[291, 292] In addition, since *Arduengo's* groundbreaking work in 1991, the number of reports on applications in the field of medicinal chemistry for transition metal NHC complexes has significantly increased, demonstrating promising antibacterial- ,antiviral-, anti-proliferative properties and different mechanisms of action, further broadening their potential applications.[141, 257, 285, 293-298]

In conclusion, significant resources are devoted in general to drug discovery research. In 2023, pharma companies like *Merck&Co.* (USD 30.5 billion), *Roche* (USD 14.7 billion), *Novartis* (USD 13.6 billion), *Johnson& Johnson* (USD 11.9 billion USD) invested billions of US-Dollar (USD) in research and development (R&D).[299]

1.3.3. Rising Costs in Drug Development: Addressing Reproducibility

Despite the remarkable progress in synthesizing new drugs and uncovering novel mechanisms in the oncogenic process, the success rate for approval of oncology drugs remains low, with approval rates as low as 20% in 2004.[300] Between July 2017 and July 2022, the FDA approved a total of 67 novel oncology therapeutic products for example, lung cancer (n= 10, 14.9%), breast cancers (n = 8, 11.9%), leukemia (n = 10, 14.9%) and lymphoma (n = 9, 13.4%).[301]

Over time, pharmaceutical R&D has faced a steady decline in productivity.[302] While other industries have seen improved output per dollar invested, drug discovery and development have become increasingly expensive, with the investment required for new drugs approximately doubling every nine years between 1950 and 2010.[303] It was estimated that the actual R&D cost per newly approved drug at 12 major pharmaceutical companies ranged from 3.7 to 11.9 billion USD.[304]

One reason for the rising costs is that every new drug must demonstrate superiority over all existing drugs. Furthermore, health authorities have become more cautious of safety issues, particularly after the incidences involving Cerivastatin and Rofecoxib (Figure 20).[305-308] In addition, clinical trial failure rates have increased considerably within the last two decades, with the highest failure of 90% in oncology.[309]

Cerivastatin
Lipobay
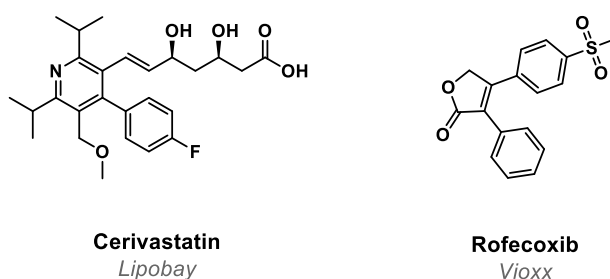
Rofecoxib
Vioxx

Figure 20. Chemical structures of Cerivastatin (Lipobay®) and Rofecoxib (Vioxx®).[310, 311]

Another major contributing factor, common across all sectors of R&D in both large companies and universities, is the "reproducibility of published findings".[312-317]

Recent analyses by the pharmaceutical industry have shown that most of these published studies could not be reproduced under well-controlled and standardized conditions.[314] In 2011, *Prinze et al*.- investigated 57 drug discovery projects in the fields of cardiovascular disease and oncology, concluding that more than two-thirds of them were major discrepancies compared to published data, ultimately leading to project termination. Others have reported reproducibility issues in more than 50% of biomedical literature.[318-320] These estimates should, however, be treated with caution due to the influence of many contributing factors -such as mishandled reagents, poorly defined laboratory protocols, and the challenges involved in recreating and comparing experiments -the economic impact is still significant.[321] *Freedman et*

al. estimated in 2015 that, in the USA alone, 28 billion USD is spent annually on preclinical research that is not reproducible.[322]

Most approaches to addressing the so-called "reproducibility crisis" aim to minimize human errors by focusing on developing and implementing guidelines, standards, and best practices.[323-326] While these measures could enhance reproducibility, they would also make research slower and more costly. An alternative approach involves automated laboratories or platforms, where guidelines are encoded in software, robots, and artificial intelligence (AI) to assist humans in their decisions, improve workflow, and enhance reproducibility.[327-330]

2. Objective

The primary objective of the present thesis is to fine-tune the electronic properties of tetradentate NHC ligand systems used for iron NHC epoxidation catalysis by introducing electron-donating or electron-accepting backbone modifications. Therefore, new ligand systems are developed to optimize the performance of the respective iron NHC catalysts.

Another key objective is synthesizing a series of ligands with saturated and unsaturated backbones and adjustments to cavity sizes to explore their influence on the catalytic activity of corresponding iron-NHC complexes.

Additionally, the thesis also aims to improve the workflow of catalytic experiments. This includes automating tedious tasks such as time-controlled sampling during catalysis or preparing various dilutions for stock solutions or analytics. A "catalysis robot" is designed to perform such tasks to enhance reproducibility and reduce manual workload.

Lastly, the open-chain or tetradentate macrocyclic ligands, originally developed for iron epoxidation catalysis, will also be explored for their potential to synthesize new group 10 or 11 metal complexes and evaluate their antiproliferative activity against various cancer cell lines.

3. Results and Discussion – Publication Summaries - Reprint Permissions

This chapter summarizes the published results of the doctoral thesis.

3.1. Synthesis, Characterization, and Biomedical Evaluation of Ethylene-bridged tetra-NHC Pd(II), Pt(II) and Au(III) Complexes, with Apoptosis-inducing Properties in Cisplatin-resistant Neuroblastoma Cells

Wolfgang R. E. Büchele,[#] Tim P. Schlachta,[#] Andreas L. Gebendorfer, Jenny Pamperin, Leon Richter, Michael J. Sauer, Aram Prokop, Fritz E. Kühn*

RSC Adv. **2024**, *14*, 10244-10254, DOI: 10.1039/D4RA01195C.[331]

[#] Equally contributed to this work.

*Corresponding authors

3.1.1. Publication Summary

The article presents the synthesis, characterization, and biomedical evaluation of novel ethylene-bridged NHC ligands (**19-23**) and their corresponding Pd(II), Pt(II), and Au(III) complexes (**24-31**) (Figure 21).

Two types of macrocyclic ligands were developed: one with an unsaturated imidazole backbone (**19**-**20**) and the other with a saturated imidazoline backbone (**21**-**22**). Furthermore, an open-chained saturated imidazoline ligand (**23**) was developed and forms open-chained tetra carbene Pd(II) and Pt(II) complexes (**30**-**31**) with two coordinated NHC ligands (Figure 21). The ethylene-bridged NHC ligands are analogs to methylene-bridged NHC ligands used for the iron complexes **11a/b**. Structural characterization using single-crystal X-ray diffraction (SC-XRD) revealed that the metal complexes adopt distorted square planar geometries, with ligands in a *syn* conformation and a strongly saddle-shaped structure. Furthermore, NMR analysis showed unexpected downfield carbene carbon signals in the imidazoline complexes, providing insight into their unique electronic properties. In addition, biomedical evaluation demonstrated that the Au(III) complex (**27**) effectively induces apoptosis in cisplatin-resistant SK-N-AS neuroblastoma cells, presumably *via* the mitochondrial and ROS pathways. However, a high concentration of **27** is required. Overall, this work shows the potential of a new set of ligand systems, offering valuable structural, electronic, and biological insights.

19 X = OTf
20 X = PF$_6$

21 X = OTf
22 X = PF$_6$

23

24 M = Pd^{II} ; X = OTf
25 M = Pd^{II} ; X = PF$_6$
26 M = Pt^{II} ; X = OTf
27 M = Au^{III}; X = PF$_6$

28 X = OTf
29 X = PF$_6$

30 M = Pd^{II}
31 M = Pt^{II}
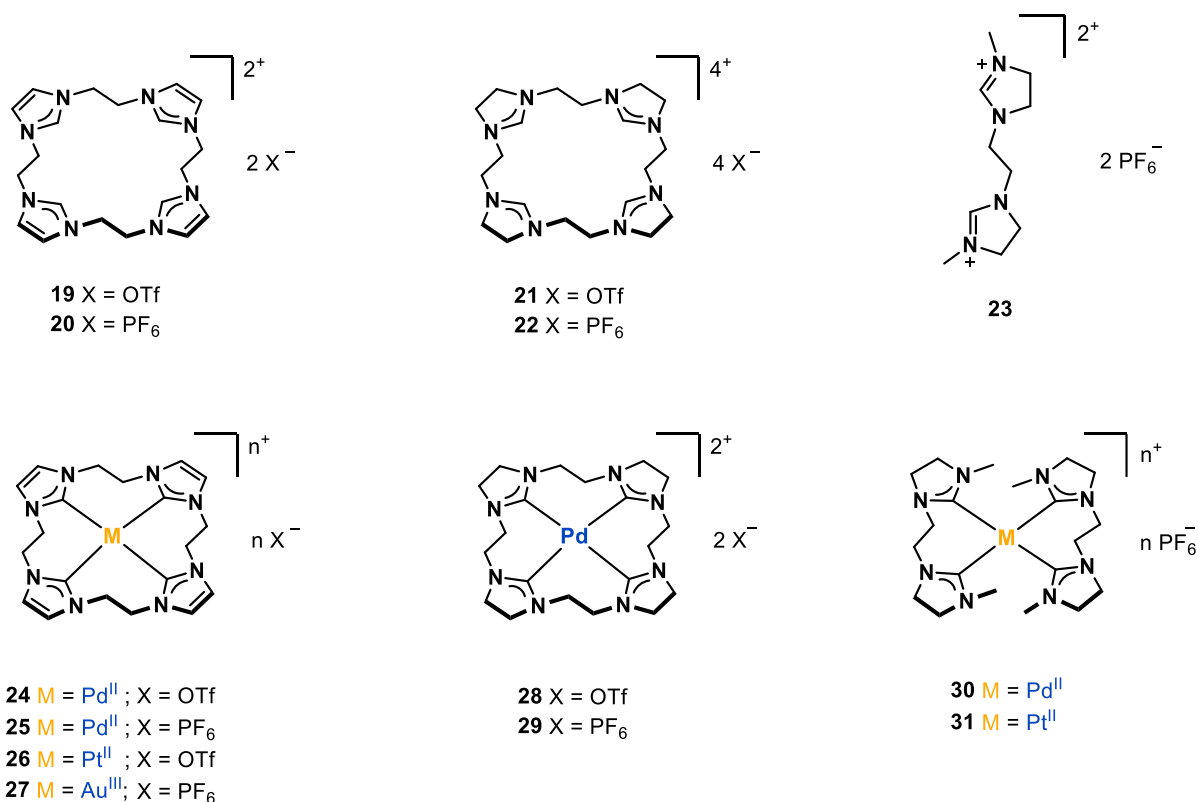
Figure 21. Synthesized tetracarbene ligands with an unsaturated backbone (**19-20**) and the respective transition metal complexes (Pd(II) **24-25**, Pt(II) **26** and Au(III) **27**), saturated backbone ligand (**21-22**) and the respective transition metal complexes (Pd(II) **28-29**), and an open-chained saturated ligand (**23**) and the respective transition metal complexes (Pd(II) **30**, Pt(II) **31**).
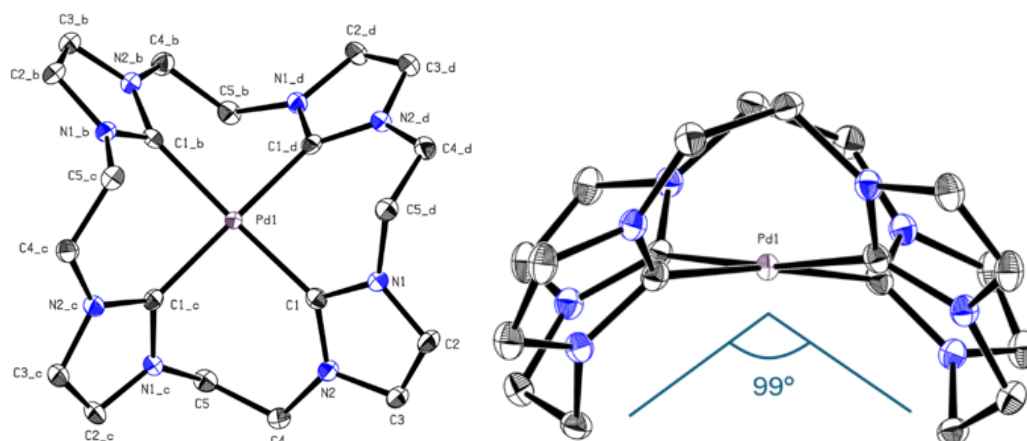
Figure 22. ORTEP-style representation of the cationic fragment of complex **25**. Hydrogen atoms and hexafluorophosphate anions are omitted for clarity. Thermal ellipsoids are shown at a 50% probability level. Top perspective (left), side perspective (right). Selected bond lengths (Å) and angles (°): C1–Pd 2.019(2), C1–Pd1–C1_b 172.03(12), C1–Pd1–C1_d–N2_d 53.62, C5–Pd1–C5_b 98.97°. Reproduced and modified from Ref.[331]
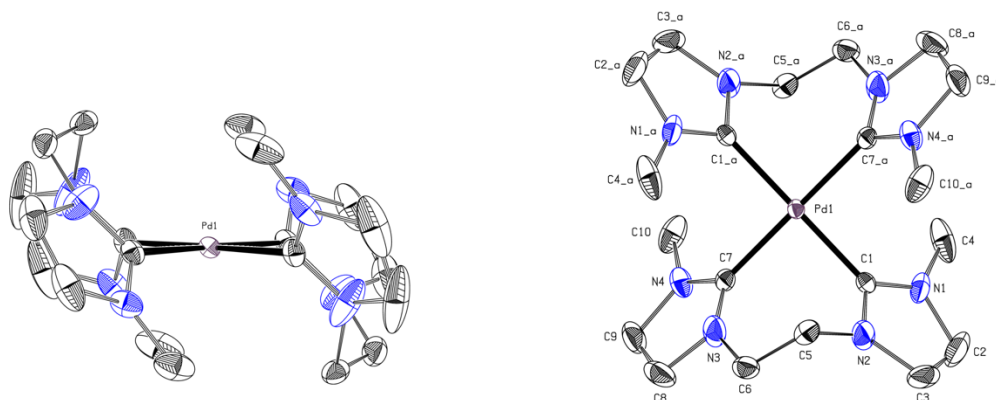
Figure 23. ORTEP-style representation of the cationic fragment of complex **30**. Hydrogen atoms and hexafluoro-phosphate anions are omitted for clarity. Thermal ellipsoids are shown at a 50% probability level**.** Top perspective (left), side perspective (right). Selected bond lengths (Å) and angles (°): C1-Pd1 2.039(2); C7-Pd1 2.038(2); C7_a-Pd1-C7 180.0; C7-Pd1-C1_a 91.64(9); C7-Pd1-C1 88.36(9), C7_a-Pd1-C1_a-N2_a 55.30. Reproduced and modi-fied from Ref.[331]

3.1.2. Reprint Permission

Obtained from https://doi.org/10.1039/D4RA01195C

3.2. MULA, an affordable framework for multifunctional liquid automation in natural- and life sciences with a focus on hardware design, setup, modularity and validation

Leon F. Richter[1], Wolfgang R. E. Büchele[1], Alexander Imhof, Fritz E. Kühn[*]

[1]Equally contributed to this work.

[*]Corresponding authors

3.2.1. Publication Summary

This article describes the development, design, and validation of MULA (Multifunctional Liquid Automation), an affordable and highly customizable liquid-handling system aimed at addressing the limitations of expensive commercial alternatives and a possible DIY solution for the "reproducibility crises". MULA is developed for academic and smaller research laboratories, costing approximately 700€. It integrates a Hamilton gastight micro-syringe for precise liquid handling, including non-aqueous solvents and closed vial systems, making it ideal, e.g., for taking accurately timed samples in catalytic setups. The system operates on a Cartesian motion system with four movable axes (X, Y, Z, and I, which control syringe plunger movement) and features a modular rack system adaptable to different viral arrangements (Figure 24, Figure 25).
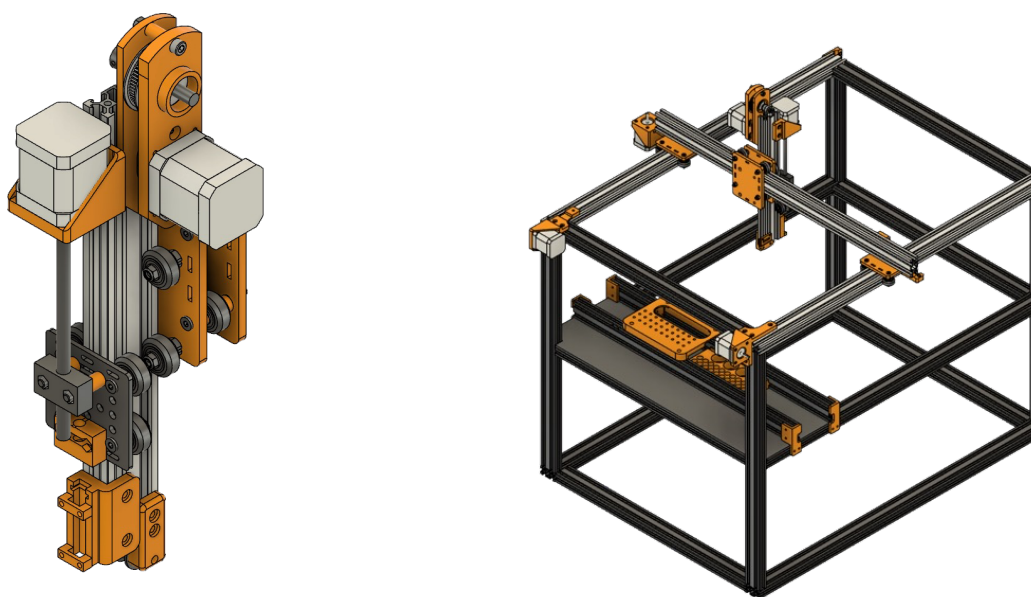
Figure 24. CAD file of the assembled I-, Z-axis, with omitted screws, pulleys, and belts, and the CAD file of MULA with a diagonal view.
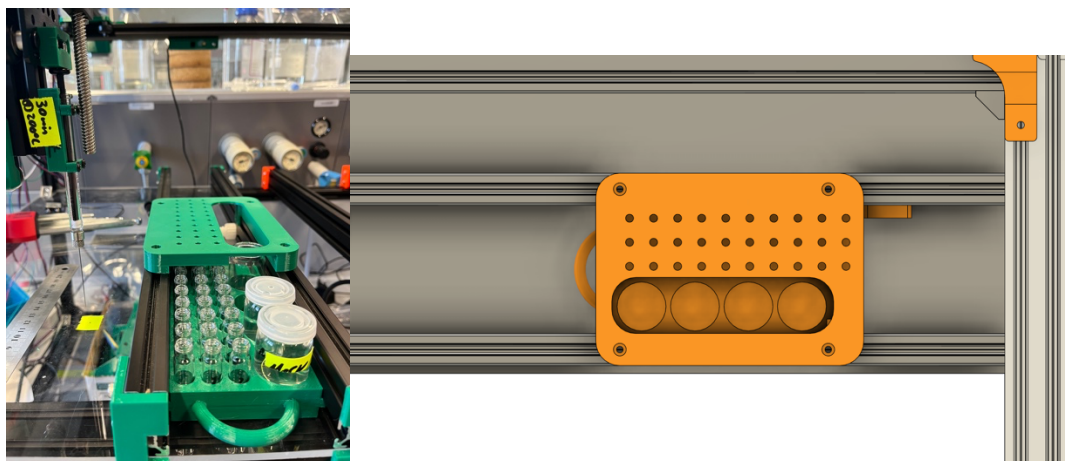
Figure 25. Picture of the employed rack for taking timed catalytic samples (left) and the respective CAD file (right).

Key features of the system include sensorless homing for enhanced reproducibility, compact design, and the use of open-source software (Marlin firmware, Pronterface) for motion control *via* G-code commands. All custom components are 3D-printed, eliminating the need for complex tools like CNC routers or laser cutters, thereby increasing accessibility for smaller labs and private use. Furthermore, all electronic parts, such as the employed *NEMA* 17 stepper motors or the *BTT Octopus 1.1* board, are commercially available. In addition, the modularity of MULA enables easy modifications and upgrades. Also provided in this work are detailed CAD files, instructions, and firmware under a CC BY NC 3.0 license for adoption and further innovation of MULA, enabling research groups to enhance reproducibility and focus on scientific discovery.

3.2.2. Reprint Permission

HardwareX **2024**, *20*, e00581, DOI: 10.1016/j.ohx.2024.e00581[332]

„Please note that, **as the author of this Elsevier article, you retain the right to include it in a thesis or dissertation, provided it is not published commercially. Permission is not required**, but please ensure that you reference the journal as the original source. For more information on this and on your other retained rights, please visit https://www.elsevier.com/about#Author-rights."

Obtained from https://doi.org/10.1016/j.ohx.2024.e00581

Hardware Article

MULA, an affordable framework for multifunctional liquid automation in natural- and life sciences with a focus on hardware design, setup, modularity and validation

Leon F. Richter [1], Wolfgang R.E. Büchele [1], Alexander Imhof, Fritz E. Kühn ✉

Show more ∨

+ Add to Mendeley   ⊷ Share   55 Cite

Abstract

The implementation of automation has already had a considerable impact on chemical and pharmaceutical industrial laboratories. However, academic laboratories have often been more reluctant to adopt such technology due to the high cost of commercial liquid handling systems, although, in many instances, there would be a huge potential to

4. Unpublished Results

This chapter provides a brief overview of the incomplete projects, the available data, and steps required for their completion.

4.1. General Information

Unless otherwise stated, all reactions in this Thesis involving air-sensitive or moisture-sensitive reagents are carried out in flame-dried glassware under argon pressure using *Schlenk* techniques.

Solvents and reagents

Dried solvents for moisture-sensitive reactions are obtained from an MBraun solvent purification system (*MB-SPS-800*) and dried over molecular sieves 3 Å. DMSO was dried being refluxed over CaH_2 and distilled prior to being stored over molecular sieves 4 Å. Solvents used for column chromatography purification or aqueous work-ups are distilled in advance.

All reagents are purchased from commercial sources and used without further purification unless otherwise stated.

Nuclear Magnetic Resonance Spectroscopy

NMR spectra are recorded with a *Bruker Avance DPX 400* or 500-cryo [^{1}H-NMR (400.15 MHz); ^{13}C-NMR (100.53 MHz)] and *Bruker Avance III 400* [^{2}H-NMR (61 MHz); ^{19}F-NMR, (471 MHz). Chemical shifts (d) are given in parts per million [ppm] relative to TMS (tetramethylsilane) and reported relative to the residual signal of the deuterated solvent.[333]

For ^{1}H-NMR: $CDCl_3$ (d = 7.26 ppm), MeOD-d_4 (d = 3.31 ppm), DMSO-d_6 (d = 2.50 ppm) CD_3CN (d = 1.94 ppm) . The signal multiplicity is abbreviated as followed: singlet [s], doublet [d], triplet [t], quartet [q] and multiplet [m]. Coupling constants (*J*) are given in Hertz [Hz].

For ^{13}C-NMR spectra are recorded on the same AV-400 or AV-500-cyro spectrometers operating at 63.9- and 126 MHz respectively with proton decoupling. The chemical shift (d) was given in parts per million [ppm] and is reported to the residual deuterated solvent: $CDCl_3$ (d_c = 77.16 ppm, MeOD-d_4 (d_c = 49.00 ppm), DMSO-d_6: (d_c = 39.52 ppm), CD_3CN: (d_c = 1.32 ppm).

Column Chromatography and Thin Layer Chromatography

Silica gel Si 60 (230-400 mesh, ASTM) with a particle size of 40-63 ym for the column chromatography by the company Merck is used. The corresponding eluent ratios are found in the individual experimental procedures.

Thin layer chromatography silica gel 600G F254 glass plates by Merck are used as the stationary phase. The substances are verified *via* fluorescence detection. Therefore, the TLC-

plates were analyzed under UV-light (λ = 254 nm) and, if necessary, evaluated by the following solutions, heat treatment included (250 °C).

Potassium permanganate-solution [$KMnO_4$]: $KMnO_4$ (2.25 g), K_2CO_3 (15.0 g) and

NaOH (250 mg) in water (250 mL).

Elemental Analysis

The determination of the elemental composition (C/H/N) is carried out at the *Technische Universität München* in the micro-analytical laboratory. The used device is a Vario EL from *Elementar*.

Mass Spectrometry [High-resolution Electrospray ionization (HRESI)]

High-resolution mass spectra (HRMS) are recorded on a *Thermo Finnigan LTQ* FT (HRMS-ESI) with each value obtained within 5 ppm of the calculated mass. ESI-MS were aquired on a *Thermo Fisher Ultimate 3000* using formic acid as eluent additive.

Cyclic voltammetry

CV measurements are recorded using a *Metrohm Autolab potentiostat* employing a gastight three-electrode cell under an argon atmosphere. A glassy carbon electrode was used as the working electrode and polished before each measurement. A graphite stick was used as the counter electrode. The potential was measured against Ag/AgCl (3.4 M KCL) with a scan rate of 100 mV/s, and ferrocene was applied as an internal standard. Tetrabutylammonium hexafluorophosphate (100 mM in MeCN) is used as the electrolyte. The concentration of the complexes is about 5 mM.

4.2.   Epoxidation Iron-Catalysis-Project.

Based on the results of the comparative catalytic study conducted by *Bernd et*. *al*., which revealed that reducing the donor strength of macrocyclic tetra-NHC ligands enhances catalyst stability for iron-based epoxidation catalysis at the cost of an overall lower activity.[133] The decreased activity of the catalyst seems to benefit the epoxidation of more challenging olefins as substrates compared to the benchmark system *cis*-cyclooctene.

Therefore, a new set of ligands has been developed. The resulting calix[4](4,5-diphenyl imidazolium) triflate (**32**) and calix[4](4,5-bis(*para*-fluorophenyl)imidazolium) triflate (**33**), previously synthesized by *Bernd*[334], aim to slightly decrease the NHC donor strength and optimize the respective iron complexes (**34-37**)(Table 1). CV experiments of **34** and **35** showed that both complexes undergo a reversible one-electron oxidation step. While the characterization of the respective ligands and iron complexes is nearly complete, some challenges remain. For instance, despite repeated efforts, a clean elemental analysis of **34** could not be obtained; however, the obtained HR-ESI-MS confirms the purity of the complex **34**. Preliminary epoxidation catalysis of **34** suggests that the π-system of the phenyl rings does not interact with the π-system of the imidazole. This finding is also confirmed by the obtained crystal structure of **34** (Figure 26). In the case of **35**, the crystals obtained still require measurements and refinement for publication.

In addition to **32** and **33**, an ethylene-methylene bridged naphtho[2,3-d]imidazole ligand (**38**) was synthesized and fully characterized to further decrease the NHC donor strength. However, the poor solubility of **38** has made the synthesis of the corresponding Fe(II) complex quite challenging. Efforts to synthesize a purely methylene-methylene-bridged naphtho[2,3-d]imidazole ligand were unsuccessful, due to the resulting steric stress in the system.

Table 1 provides a comprehensive overview of all the available analytical data for compounds **32**-**38**. Moving forward, catalytic experiments with the respective catalysts **34**-**37** should be conducted for publication.

Table 1: Overview of the available analytical data of compounds **32-38**.
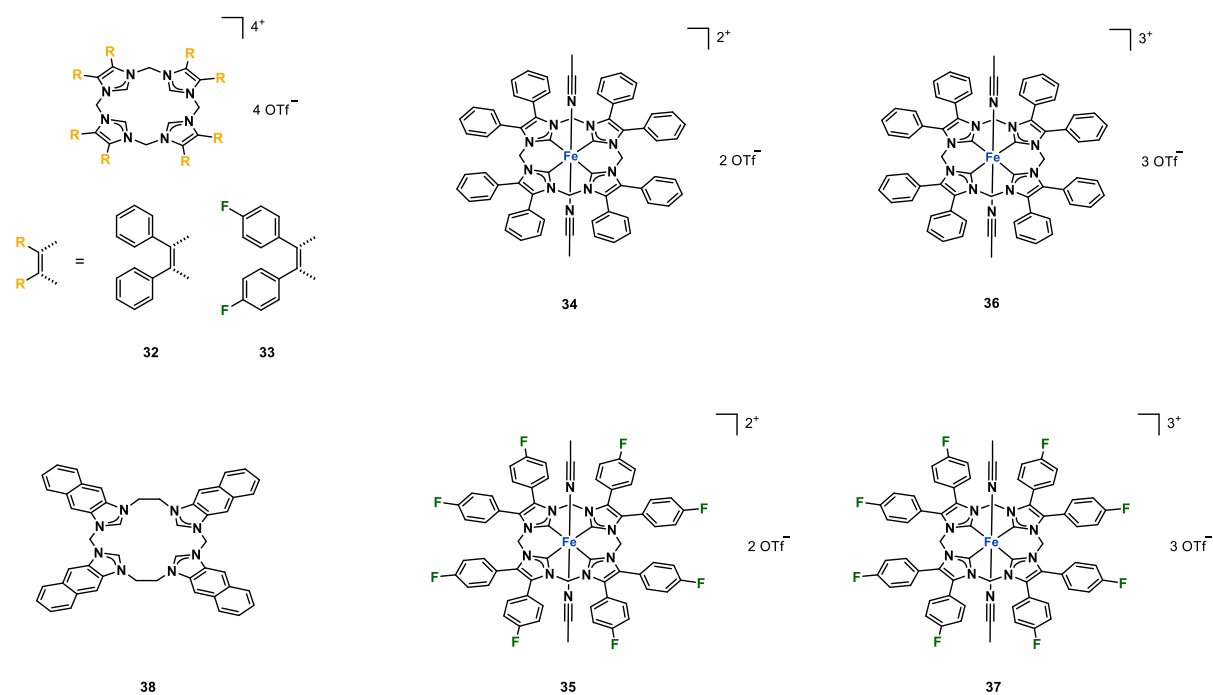
Compound	32	33	34	35	36	37	38
Synthesis	✓	✓	✓	✓	✓	✓	✓
Characterization [NMR]	✓	✓	✓	✓	✓	✓	✓
EA	✓	✗	✗	✓	✗	✓	✓
HR-ESI-MS	✓	✓	✓	✓	/	/	✓
Crystal Structure	/	/	✓	~	/	✓	/
CV	/	/	✓	✓	/	/	/
UV-Vis	/	/	✓	✓	/	/	/
Catalysis	/	/	✗	✗	✗	✗	/

[✓] Data available, [✗] Missing/ not obtained, [/] compound available if needed, [~] partially completed.
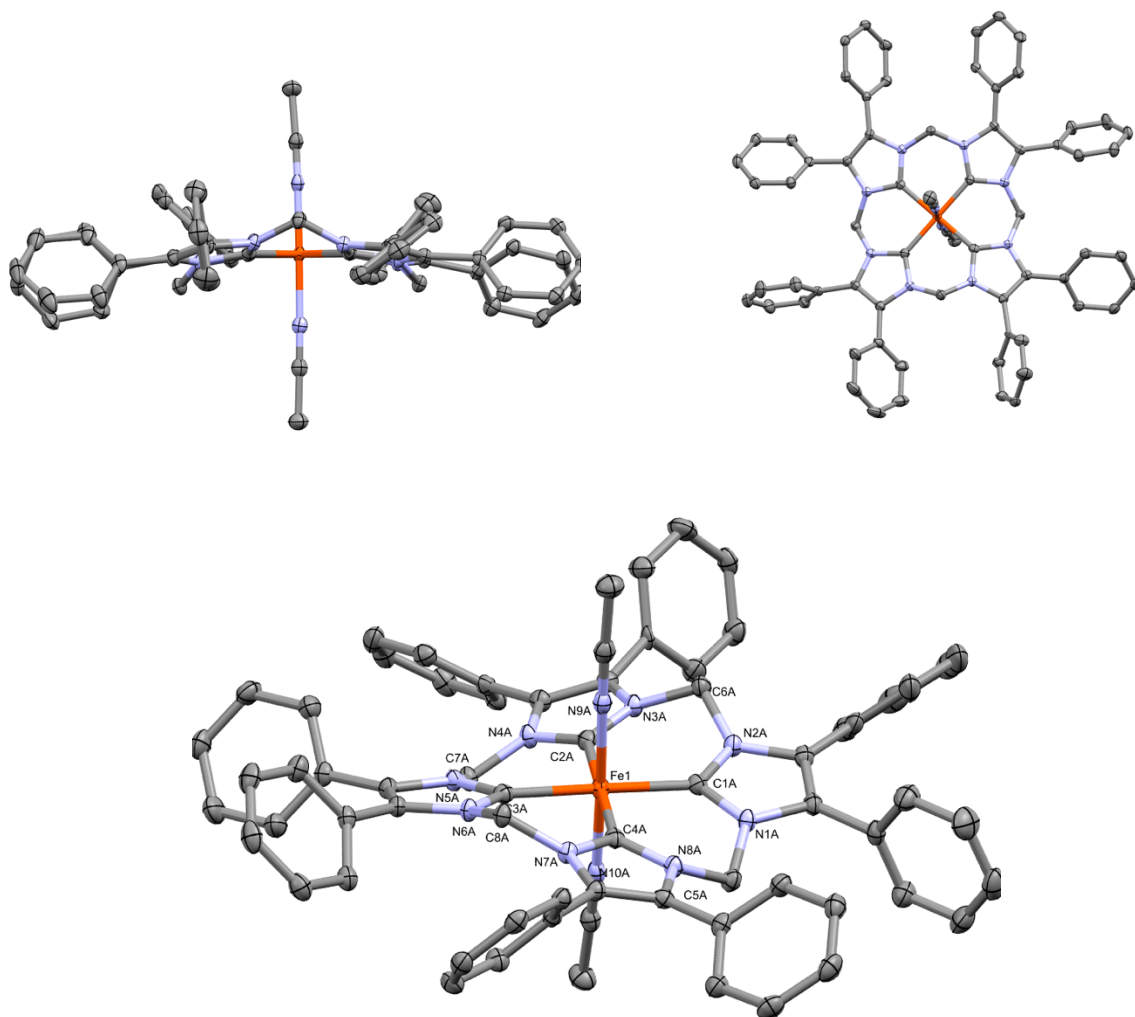
Figure 26. ORTEP-style representation of the cationic fragment of complex **34**. Hydrogen atoms and triflate anions are omitted for clarity. Thermal ellipsoids are shown at a 50% probability level**.** Side perspective (top left), Top perspective (top right) and diagonal perspective (middle). Selected bond lengths (Å) and angles (°): C1A-Fe1 1.924(19); C2A-Fe1 1.929(19); C1A-Fe1-C3A 178.9(8); C2A-Fe1-C3A 90.4(8); C1A-Fe1-C4A 90.1(8); C3A-Fe1-C4A 89.8(8).

4.3. Calix[4](4,5-dimethylimidazolyl)-Project

Building on the work of *Bernd*[334], the characterization of the calix[4](4,5-dimethylimidazolyl) (**39/40**) and the respective group 10 and 11 complexes (**41**-**48**) is nearly complete. The synthesis of the Au(III) complex (**45**) and Cu(I)-complex (**46**), with the structures AuL and Cu_4L_2 respectively, has been successful. Furthermore, crystal structures suitable for publication have been obtained for both complexes (**45** Figure 27, **46** Figure 28).

As a final step, UV-Vis spectra for these complexes need to be measured. Additionally, the ground-state and transition-state geometries for the ligand vibrations need to be calculated using DFT. The following Table 2 provides an overview of the available data for compounds **39-48**.

Table 2 Overview of the available analytical data of compounds **39**-**48**.
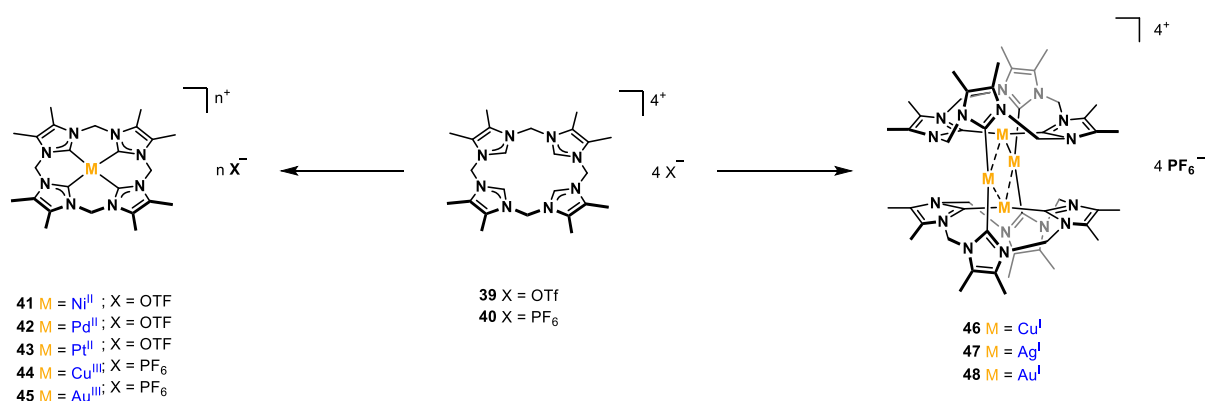
Compound	39	40	41	42	43	44	45	46	47	48
Synthesis	✓	✓	✓	✓	✓	✓	✓	✓	✓	✓
Characterization [NMR]	✓	✓	✓	✓	✓	✓	✓	✓	✓	✓
EA	✓	✓	✓	✓	✓	✓	✓	✓	✓	✓
ESI-MS	/	/	✓	✓	✓	✓	✓	✗	✓	✓
Crystal Structure	/	/	✓	✓	✓	✓	✓	✓	✓	✓
UV-Vis	/	/	✗	✗	✗	✗	✗	✗	✗	✗
DFT	✗	✗	✗	✗	✗	✗	✗	✗	✗	✗
Biological Studies	✓	✓	✗	✓	✗	✗	~	✗	~	~

[✓] Data available, [✗] Missing/ not obtained, [/] compound available if needed, [~] partially completed.
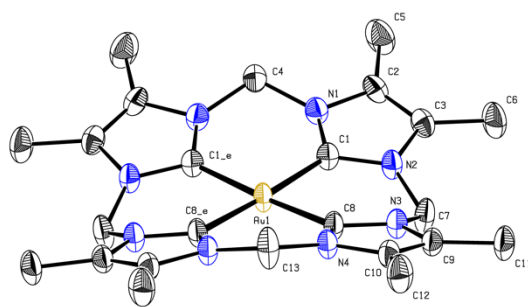
Figure 27. ORTEP-style representation of the cationic fragment of complex **45**. Hydrogen atoms and hexafluorophosphate anions are omitted for clarity. Ellipsoids are shown at a 50% probability level**.**
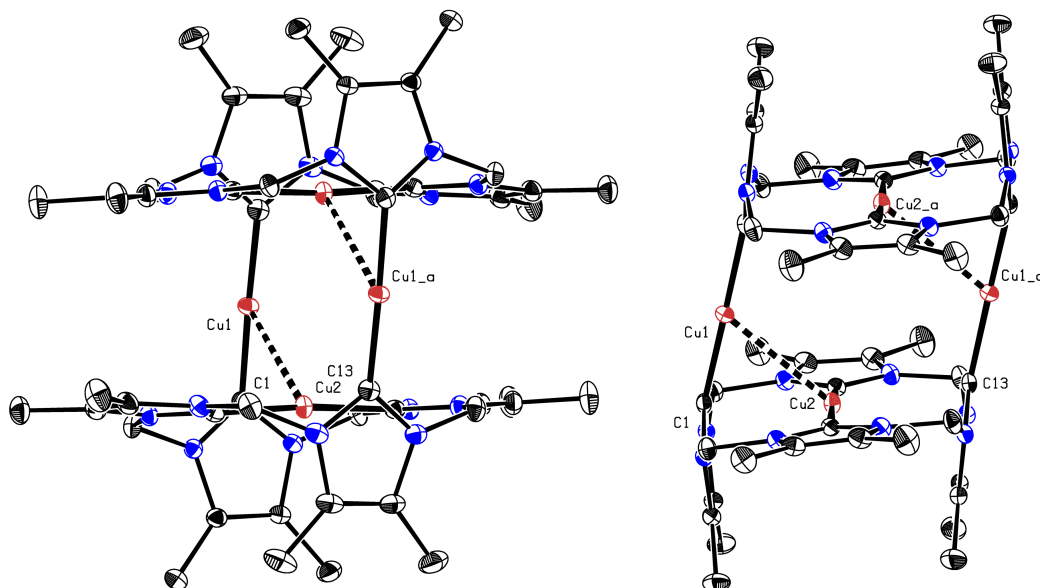
Figure 28. ORTEP style representation of the cationic fragment of **46** with ellipsoids shown at a 50% probability level. Hydrogen atoms and hexafluorophosphate anions are omitted for clarity. The dashed line indicates the metallic interactions.

5. Conclusion and Outlook

onclusion and Outlook

 the course of this thesis, various novel macrocyclic tetra-dentate- and open-chained NHC ligand systems with distinct electronic properties have been synthesized and characterized. These ligands were applied in the synthesis of a range of transition metal complexes, including iron and group 10/11 metals. While the iron complexes were specifically designed for epoxidation catalysis, their catalytic performance remains to be investigated in future studies. In con-

trast, the group 10/11 transition metal complexes were investigated for their potential application in medicinal chemistry, particularly for their antiproliferative effects on cancer cells. Additionally, a pipetting robot called "MULA" has been developed for improving laboratory workflows and enhancing the reproducibility of experimental results.

e benchmark ligand system used for the epoxidation catalysis by *Kühn* (*Inorg. Chem.* **2015**, *54*, 3797-3804) was modified to fine-tune the NHC donor strength and optimize the catalytic properties of the respective iron complexes. The decreased activity of the catalyst seems beneficial for the epoxidation of more challenging olefins as substrates compared to *cis*-cyclooctene. Therefore, phenyl groups and fluorine-substituted phenyl groups have been introduced as backbone modifications to decrease the NHC donor strength *via* the -M effect of the phenyl group and further reduced through the -I effect of the fluorine substitution. Both ligands are purely methylene bridged to provide comparability of the ligands and have been solely utilized for the synthesis of Fe(II) and Fe(III) complexes so far.

ditionally, a methylene-ethylene-bridged ligand harboring a naphtho[2,3-d] imidazolium framework was developed to extend the aromatic system, enhancing stability under oxidative conditions. This ligand is ethylene methylene bridged and was designed to explore whether the trends observed with the benzimidazole system (*J. Catal.* **2020**, *391*, 548-561) would persist.

lely ethylene-bridged ligands with saturated and unsaturated backbones were also synthesized to explore the influence of electronic properties and flexibility in epoxidation catalysis. The ethylene-bridged ligands have also been utilized to synthesize various group 10 and 11 complexes. Pd(II), Pt(II), and Au(III) complexes were obtained with the cyclic saturated ligand and a Pd(II) complex with the unsaturated ligand and applied in a biological study for antiproliferative effects on cancer cells. In addition, Pd(II) and Pt(II) complexes with ethylene-bridged open-chained unsaturated ligands were also tested. The study revealed the Au(III) complex induces apoptosis in SK-N-AS cells (human neuroblastoma cell line) and overcomes cisplatin resistance *in vitro* in cisplatin-resistant SK-N-AS cells, although at a relatively high concentration.

pipetting robot named "MULA" has been developed and validated for accuracy in accordance with DIN EN ISO 8655 standards. Special attention was placed on the easy use and improving the laboratory workflows. For instance, MULA facilitates accurately timed sampling in catalytic setups under oxygen free conditions, enables high-throughput screening to optimize solvent ratios for improved crystal growth, minimizes pipetting errors during repetitive tasks, and ensures precise pipetting for small-scale NMR experiments.

ture research on the epoxidation catalysis topic should focus on the catalytic investigation of the synthesized iron complexes and the synthesis of the respective iron complexes, especially for the saturated and unsaturated backbones systems, to assess the impact of the system

flexibility and the electronic effects. This could be helpful for the development of future strategies for improving the catalytic performance of iron NHC complexes. Additionally, detailed DFT calculations should be considered to analyze whether the electron density on the iron center has such a significant influence or if other parameters might have a considerably greater impact, e.g. the stability of the ligand under oxidative conditions or the ligand flexibility. Also, DFT calculations on the epoxidation mechanism could provide a deeper understanding of the epoxidation and help to develop better strategies to improve the catalytic performance of the iron NHC complexes. In addition, a high-throughput screening of various substrates for the epoxidation catalysis could be conducted with MULA.

rther research in medicinal chemistry should focus on exploring the methylene-ethylene-bridged naphtho[2,3-d] imidazolium system and synthesizing respective silver and gold complexes to leverage the luminescence properties of the ligand. Additionally, future fluorescence studies could provide valuable insight into the underlying mechanism by locating the respective complexes.

reover, the cuprophilic interactions of the synthesized Cu(I) complex based on the 4,5-dimethylimidazole system (*J. Catal*. **2020**, *391*, 548-561) should be investigated for its potential application in the electroreduction of CO_2 to CH_4.

6. Bibliographic Data of Complete Publications

ibliographic Data of Complete Publications

nthesis, characterization, and biomedical evaluation of etyhelene-bridged tetra-NHC Pd(II), Pt(II) and Au(III) complexes, with apoptosis-inducing properties in cisplatin-resistant neuroblastoma cells

Ifgang R. E. Büchele,[#,a] Tim P. Schalchta,[#,a] Andreas L. Gebendorfer,[a] Jenny Pamperin,[c,d] Leon F. Richter,[a] Michael J. Sauer,[a] Aram Prokop,[b,c,d,*] Fritz. E. Kühn[a,*]

Technical University of Munich, School of Natural Sciences, Department of Chemistry and Catalysis Research Center, Molecular Catalysis, Lichtenbergstraße 4, 85749 Garching, Germany

Department of Pediatric Hematology/Oncology, Children's Hospital Cologne, Amsterdamer Straße 59, 50735 Clogne, Germany

Department of Pediatric Oncology/Hematology, Helios Clinics Schwerin, Wismarsche Straße 393-397, 19055 Schwerin, Germany

Department of Human Medicine, MSH Medical School Hamburg, Am Kaiserkai 1, 20457 Hamburg, Germany

[#] Equally contributing authors

Neq[u]ally contributing authors

Equally contributing authors

Corresponding authors

Ref.[331]

ef.[331]

f.[331]

rect link: https://doi.org/10.1039/D4RA01195C

MULA, an affordable framework for multifunctional liquid automation in natural- and life sciences with a focus on hardware design, setup, modularity and validation

on F. Richter[1], **Wolfgang R. E. Büchele**[1], Alexander Imhof, Fritz E. Kühn[*]

echnical University of Munich, TUM School of Natural Sciences, Deparment of Chemistry and Catalysis Research Centre, Molecular Catalysis, Lichtenbergstr. 4, Garching bei München, Germany

chnical University of Munich, TUM School of Natural Sciences, Deparment of Chemistry and Catalysis Research Centre, Molecular Catalysis, Lichtenbergstr. 4, Garching bei München, Germany

[1]Equally contributed to this work.

No[u]ally contributed to this work.

qually contributed to this work.

orresponding authors

Ref.[332]

ef.[332]

f.[332]

rect link: https://doi.org/10.1016/j.ohx.2024.e00581

6.1. Complete List of Publications

]   L. F. Richter,[#] **W. R. E. Büchele**,[#] A. Imhof, F. E. Kühn, „ MULA, an affordable frame-work for multifunctional liquid automation in natural- and life sciences with a focus on hardware design, setup, modularity and validation", *HardwareX* **2024**, *20*, e00581, DOI: 10.1016/j.ohx.2024.e00581.

]   **W. R. E. Büchele**,[#] T. P. Schalchta,[#] A. L. Gebendorfer, J. Pamperin, L. F. Richter, M. J. Sauer, A. Prokop, F.. E. Kühn "Synthesis, characterization, and biomedical evaluation of etyhelene-bridged tetra-NHC Pd(II), Pt(II) and Au(III) complexes, with apoptosis-inducing prop-erties in cisplatin-resistant neuroblastoma cells", *RSC Adv.* **2024**, *14*, 10244-10254, DOI: 1039/D4RA01195C.

 Equally contributing authors

Table 3. Contributions of W. R. E. Büchele to the publications. [#] Equally contributing first authors.

No.	Bibliographic Data	Ref.	Chapter	Author	Contribution, CRediT roles
[2]	*HardwareX* **2024**, *20*, e00581	[331]	3.2	2nd [#]	Writing – original draft, Vali-dation, Project administration, Investigation, Data curation, Conceptualization
[1]	*RSC Adv.* **2024**, *14*, 10244-10254	[332]	3.1	1st	conceptual approach, experi-mental work and related data interpretation, project admin-istration, conception and writ-ing – original draft, writing – review & editing, data cura-tion, formal analysis, investi-gation, methodology, visuali-zation

7. References

[1]   R. Teranishi, E. L. Wick, I. Hornstein, *Flavor Chemistry: Thirty Years of Progress* **1999**, 1-8.

[2]   A. Schuhmacher, M. Hinder, O. Gassmann, *Value Creation in the Pharmaceutical Industry,* Wiley-VCH. Weinheim: **2016**.

[3]   M. Baerns, *Technische chemie,* John Wiley & Sons: **2013**.

[4]   M. Cui, Z. Chai, Y. Lu, J. Zhu, J. Chen, *Resources Chemicals and Materials* **2023**, *2*, 262-276.

[5]   G. Fráter, J. A. Bajgrowicz, P. Kraft, *Tetrahedron* **1998**, *54*, 7633-7703.

[6]   M. Gautschi, J. A. Bajgrowicz, P. Kraft, *Chimia* **2001**, *55*, 379-379.

[7]   R. A. Phillipps, *CHEMICAL INDUSTRIES-NEW YORK-MARCEL DEKKER-* **1999**, 393-412.

[8]   P. Barthe, M. Chaugny, S. Roudier, L. Delgado Sancho, *European Commission* **2015**, *754*.

[9]   K. Weissermel, H.-J. Arpe, *Industrielle Organische Chemie: Bedeutende Vor-und Zwischenprodukte,* VCH-Verlag-Ges.: **1998**.

[10]   GlobalData. October 31, 2023. "Production capacity of ethylene worldwide from 2018 to 2022." Statista, accessed 15.07.2024. https://www.statista.com/statistics/1067372/global-ethylene-production-capacity/.

[11]   GlobalData. October 12, 2023. "Production capacity of propylene worldwide in 2018 and 2022 with a forcast to 2030." Statista, accessed 15.07.2024. https://www.statista.com/statistics/1065879/global-propylene-production-capacity/.

[12]   Y. A. Treger, V. Rozanov, *Review Journal of Chemistry* **2016**, *6*, 83-123.

[13]   K. Lascelles, L. Morgan, D. Nicholls, D. Beyersmann, *Weinheim: Wiley-VCH, DOI* **2005**, *10*, a17_235.

[14]   B. Elvers, *Ullmann's Encyclopedia of Industrial Chemistry,* Verlag Chemie Hoboken, NJ: **1991**.

[15]   J. Herzberger, K. Niederer, H. Pohlit, J. Seiwert, M. Worm, F. R. Wurm, H. Frey, *Chem. Rev.* **2016**, *116*, 2170-2243.

[16]   O. Deutschmann, H. Knözinger, K. Kochloefl, T. Turek, in *Ullmann's Encyclopedia of Industrial Chemistry*.

[17]   V. K. Aggarwal, D. M. Badine, V. A. Moorthie, in *Aziridines and Epoxides in Organic Synthesis*, **2006**, pp. 1-35.

[18]   S. J. Khatib, S. Oyama, *Catalysis Reviews* **2015**, *57*, 306-344.

[19]   H.-J. Arpe, *Industrielle Organische Chemie: Bedeutende Vor-und Zwischenprodukte,* John Wiley & Sons: **2007**.

[20]   C. J. Thibodeaux, W.-c. Chang, H.-w. Liu, *Chem. Rev.* **2012**, *112*, 1681-1709.

[21]   S. D. Gagnon, *Kirk-Othmer Encyclopedia of Chemical Technology* **2000**.

[22]   D. W. Sauter, M. Taoufik, C. Boisson, *Polymers* **2017**, *9*, 185.

[23]   U. Poth, *Vincents Network, Hannover* **2014**.

[24] H. Schnell, *Angew. Chem.* **1956**, *68*, 633-640.

[25] Y. Liu, K. Deng, S. Wang, M. Xiao, D. Han, Y. Meng, *Polymer Chemistry* **2015**, *6*, 2076-2083.

[26] K. Jin, J. H. Maalouf, N. Lazouski, N. Corbin, D. Yang, K. Manthiram, *Journal of the American Chemical Society* **2019**, *141*, 6413-6418.

[27] W. Swodenk, H. Waldmann, *Chem. unserer Zeit* **1978**, *12*, 65-70.

[28] P. Kilty, W. Sachtler, *Catalysis Reviews Science and Engineering* **1974**, *10*, 1-16.

[29] S. Coleman-Kammula, E. T. Duim-Koolstra, *J. Organomet. Chem.* **1983**, *246*, 53-56.

[30] M. Bernhard, J. Anton, F. Schmidt, F. Sandkaulen, M. Pascaly, *Chem. unserer Zeit* **2017**, *51*, 198-209.

[31] T. A. Nijhuis, M. Makkee, J. A. Moulijn, B. M. Weckhuysen, *Industrial & engineering Chemistry research* **2006**, *45*, 3447-3459.

[32] M. Barteau, R. Madix, *Journal of the American Chemical Society* **1983**, *105*, 344-349.

[33] S. Ghosh, S. S. Acharyya, R. Tiwari, B. Sarkar, R. K. Singha, C. Pendem, T. Sasaki, R. Bal, *ACS Catalysis* **2014**, *4*, 2169-2174.

[34] J. Teržan, M. Huš, B. Likozar, P. Djinović, *ACS Catalysis* **2020**, *10*, 13415-13436.

[35] J. F. Schlagintweit, Transition Metal NHC Complexes in Oxidation Catalysis and Medicinal Chemistry, Technische Universität München **2021**.

[36] T. Ressler, A. Walter, J. Scholz, J. P. Tessonnier, D. S. Su, *J. Catal.* **2010**, *271*, 305-314.

[37] R. Noyori, M. Aoki, K. Sato, *Chem. Commun.* **2003**, 1977-1986.

[38] A. Vyskočil, C. Viau, *J. Appl. Toxicol.* **1999**, *19*, 185-192.

[39] A. Thangaraj, M. Eapen, S. Sivasanker, P. Ratnasamy, *Zeolites* **1992**, *12*, 943-950.

[40] T. Ressler, A. Walter, J. Scholz, J.-P. Tessonnier, D. S. Su, *J. Catal.* **2010**, *271*, 305-314.

[41] B. Notari, *Catal. Today* **1993**, *18*, 163-172.

[42] B. Cornils, W. A. Herrmann, J.-H. Xu, H.-W. Zanthoff, *Catalysis from A to Z: a concise encyclopedia,* John Wiley & Sons: **2020**.

[43] G. Parshall, *J. Mol. Catal.* **1978**, *4*, 243-270.

[44] D. Steinborn, *Grundlagen der metallorganischen Komplexkatalyse,* Springer: **2007**.

[45] Q.-H. Xia, H.-Q. Ge, C.-P. Ye, Z.-M. Liu, K.-X. Su, *Chem. Rev.* **2005**, *105*, 1603-1662.

[46] F. E. Kühn, A. M. Santos, P. W. Roesky, E. Herdtweck, W. Scherer, P. Gisdakis, I. V. Yudanov, C. Di Valentin, N. Rösch, *Chemistry–A European Journal* **1999**, *5*, 3603-3615.

[47] S. A. Hauser, M. Cokoja, F. E. Kühn, *Catal. Sci. Technol.* **2013**, *3*, 552-561.

[48] P. Altmann, M. Cokoja, F. E. Kühn, *Eur. J. Inorg. Chem.* **2012**, *2012*, 3235-3239.

[49] C. C. Romão, F. E. Kühn, W. A. Herrmann, *Chem. Rev.* **1997**, *97*, 3197-3246.

[50] L. F. Tietze, C. Güntner, K. M. Gericke, I. Schuberth, G. Bunkoczi, *Eur. J. Org. Chem.* **2005**, *2005*, 2459-2467.

[51]   D. Rowe, *Chemistry and technology of flavours and fragrances,* John Wiley & Sons: **2009**.

[52]   W. J. Choi, C. Y. Choi, *Biotechnology and Bioprocess Engineering* **2005**, *10*, 167-179.

[53]   F. Moschona, I. Savvopoulou, M. Tsitopoulou, D. Tataraki, G. Rassias, *Catalysts* **2020**, *10*, 1117.

[54]   S. Caron, R. W. Dugger, S. G. Ruggeri, J. A. Ragan, D. H. B. Ripin, *Chem. Rev.* **2006**, *106*, 2943-2989.

[55]   T. Katsuki, *J. Am. Chem. Soc* **1980**, *102*, 5974-5976.

[56]   M. Finn, K. B. Sharpless, *Journal of the American Chemical Society* **1991**, *113*, 113-126.

[57]   K. Srinivasan, P. Michaud, J. K. Kochi, *Journal of the American Chemical Society* **1986**, *108*, 2309-2320.

[58]   W. Zhang, J. L. Loebach, S. R. Wilson, E. N. Jacobsen, *Journal of the American Chemical Society* **1990**, *112*, 2801-2803.

[59]   E. N. Jacobsen, W. Zhang, A. R. Muci, J. R. Ecker, L. Deng, *Journal of the American Chemical Society* **1991**, *113*, 7063-7064.

[60]   R. Irie, K. Noda, Y. Ito, N. Matsumoto, T. Katsuki, *Tetrahedron: Asymmetry* **1991**, *2*, 481-494.

[61]   T. Linker, *Angewandte Chemie International Edition in English* **1997**, *36*, 2060-2062.

[62]   W. A. Herrmann, R. W. Fischer, D. W. Marz, *Angew. Chem.* **1991**, *103*, 1706-1709.

[63]   W. A. Herrmann, R. W. Fischer, W. Scherer, M. U. Rauch, *Angewandte Chemie International Edition in English* **1993**, *32*, 1157-1160.

[64]   A. M. Al-Ajlouni, J. H. Espenson, *Journal of the American Chemical Society* **1995**, *117*, 9243-9250.

[65]   A. M. Al-Ajlouni, J. H. Espenson, *The Journal of Organic Chemistry* **1996**, *61*, 3969-3976.

[66]   F. E. Kühn, A. M. Santos, I. S. Gonçalves, C. C. Romão, A. D. Lopes, *Appl. Organomet. Chem.* **2001**, *15*, 43-50.

[67]   I. R. Beattie, P. J. Jones, *Inorg. Chem.* **1979**, *18*, 2318-2319.

[68]   J. H. Espenson, *Adv. Inorg. Chem.* **2003**, *54*, 157-202.

[69]   J. W. Kück, R. M. Reich, F. E. Kühn, *The Chemical Record* **2016**, *16*, 349-364.

[70]   K. A. Joergensen, *Chem. Rev.* **1989**, *89*, 431-458.

[71]   B. S. Lane, K. Burgess, *Chem. Rev.* **2003**, *103*, 2457-2474.

[72]   P. R. O. De Montellano, *Cytochrome P450: structure, mechanism, and biochemistry,* Springer Science & Business Media: **2007**.

[73]   B. Meunier, S. P. De Visser, S. Shaik, *Chem. Rev.* **2004**, *104*, 3947-3980.

[74]   M.-H. Baik, M. Newcomb, R. A. Friesner, S. J. Lippard, *Chem. Rev.* **2003**, *103*, 2385-2420.

[75]   C. E. Tinberg, S. J. Lippard, *Acc. Chem. Res.* **2011**, *44*, 280-288.

[76]   R. Banerjee, J. C. Jones, J. D. Lipscomb, *Annu. Rev. Biochem* **2019**, *88*, 409-431.

[77]   I. G. Denisov, T. M. Makris, S. G. Sligar, I. Schlichting, *Chem. Rev.* **2005**, *105*, 2253-2278.

[78] T. L. Poulos, *Chem. Rev.* **2014**, *114*, 3919-3962.

[79] Y. Liu, J. C. Nesheim, S.-K. Lee, J. D. Lipscomb, *J. Biol. Chem.* **1995**, *270*, 24662-24665.

[80] K. P. Bryliakov, E. P. Talsi, *Coord. Chem. Rev.* **2014**, *276*, 73-96.

[81] A. C. Rosenzweig, C. A. Frederick, S. J. Lippard, P. Nordlund, auml, *Nature* **1993**, *366*, 537-543.

[82] C. M. M. Soe, **2012**.

[83] C. M. Krest, A. Silakov, J. Rittle, T. H. Yosca, E. L. Onderko, J. C. Calixto, M. T. Green, *Nature chemistry* **2015**, *7*, 696-702.

[84] S. Shaik, M. Filatov, D. Schröder, H. Schwarz, *Chemistry–A European Journal* **1998**, *4*, 193-199.

[85] W.-D. Woggon, H.-A. Wagenknecht, C. Claude, *J. Inorg. Biochem.* **2001**, *83*, 289-300.

[86] H. Fujii, *Coord. Chem. Rev.* **2002**, *226*, 51-60.

[87] S. Shaik, S. Cohen, Y. Wang, H. Chen, D. Kumar, W. Thiel, *Chem. Rev.* **2010**, *110*, 949-1017.

[88] R. A. Baglia, J. P. T. Zaragoza, D. P. Goldberg, *Chem. Rev.* **2017**, *117*, 13320-13352.

[89] X. Huang, J. T. Groves, *JBIC Journal of Biological Inorganic Chemistry* **2017**, *22*, 185-207.

[90] A. V. Pandey, C. E. Flück, *Pharmacology & therapeutics* **2013**, *138*, 229-254.

[91] S. Jin, T. M. Makris, T. A. Bryson, S. G. Sligar, J. H. Dawson, *Journal of the American Chemical Society* **2003**, *125*, 3406-3407.

[92] A. B. McQuarters, M. W. Wolf, A. P. Hunt, N. Lehnert, **2014**.

[93] T. H. Yosca, J. Rittle, C. M. Krest, E. L. Onderko, A. Silakov, J. C. Calixto, R. K. Behan, M. T. Green, *Science* **2013**, *342*, 825-829.

[94] J. T. Groves, W. J. Kruper Jr, *Journal of the American Chemical Society* **1979**, *101*, 7613-7615.

[95] J. T. GROVES, S. Krishnan, G. E. AVARIA, T. E. NEMO, ACS Publications, **1980**.

[96] J. T. Groves, G. A. McClusky, *Journal of the American Chemical Society* **1976**, *98*, 859-861.

[97] J. T. Groves, M. Van der Puy, *Journal of the American Chemical Society* **1976**, *98*, 5290-5297.

[98] O. Y. Lyakin, A. M. Zima, D. G. Samsonenko, K. P. Bryliakov, E. P. Talsi, *ACS Catalysis* **2015**, *5*, 2702-2707.

[99] H. Hirao, D. Kumar, S. Shaik, *J. Inorg. Biochem.* **2006**, *100*, 2054-2068.

[100] J. T. Groves, T. E. Nemo, R. S. Myers, *Journal of the American Chemical Society* **1979**, *101*, 1032-1033.

[101] C. K. Chang, F. Ebina, *J. Chem. Soc., Chem. Commun.* **1981**, 778-779.

[102] C. Chang, M.-S. Kuo, *Journal of the American Chemical Society* **1979**, *101*, 3413-3415.

[103] P. E. Ellis Jr, J. E. Lyons, *Coord. Chem. Rev.* **1990**, *105*, 181-193.

[104] J. T. Groves, R. C. Haushalter, M. Nakamura, T. E. Nemo, B. Evans, *Journal of the American Chemical Society* **1981**, *103*, 2884-2886.

[105] B. Meunier, *Chem. Rev.* **1992**, *92*, 1411-1456.

[106] D. Dolphin, T. G. Traylor, L. Y. Xie, *Acc. Chem. Res.* **1997**, *30*, 251-259.

[107] W. Nam, *Acc. Chem. Res.* **2007**, *40*, 522-531.

[108] Y. M. Goh, W. Nam, *Inorg. Chem.* **1999**, *38*, 914-920.

[109] J. Bhuyan, R. Sarkar, S. Sarkar, *Angew. Chem.* **2011**, *123*, 10791-10795.

[110] T. Asakura, in *Methods Enzymol., Vol. 52*, Elsevier, **1978**, pp. 447-455.

[111] W. Nam, Y. O. Ryu, W. J. Song, *JBIC Journal of Biological Inorganic Chemistry* **2004**, *9*, 654-660.

[112] S. M. Hölzl, P. J. Altmann, J. W. Kück, F. E. Kühn, *Coord. Chem. Rev.* **2017**, *352*, 517-536.

[113] S. Kal, S. Xu, L. Que Jr, *Angew. Chem. Int. Ed.* **2020**, *59*, 7332-7349.

[114] A. Lindhorst, S. Haslinger, F. E. Kühn, *Chem. Commun.* **2015**, *51*, 17193-17212.

[115] W. Nam, *Acc. Chem. Res.* **2015**, *48*, 2415-2423.

[116] R. A. Leising, R. E. Norman, L. Que Jr, *Inorg. Chem.* **1990**, *29*, 2553-2555.

[117] I. Prat, D. Font, A. Company, K. Junge, X. Ribas, M. Beller, M. Costas, *Adv. Synth. Catal.* **2013**, *355*, 947-956.

[118] M. H. Lim, J.-U. Rohde, A. Stubna, M. R. Bukowski, M. Costas, R. Y. N. Ho, E. Münck, W. Nam, L. Que, *Proceedings of the National Academy of Sciences* **2003**, *100*, 3665-3670.

[119] J. England, J. O. Bigelow, K. M. Van Heuvelen, E. R. Farquhar, M. Martinho, K. K. Meier, J. R. Frisch, E. Münck, L. Que, *Chem. Sci.* **2014**, *5*, 1204-1215.

[120] B. P. Murch, F. C. Bradley, L. Que, *Journal of the American Chemical Society* **1986**, *108*, 5027-5028.

[121] W. Nam, R. Ho, J. S. Valentine, *Journal of the American Chemical Society* **1991**, *113*, 7052-7054.

[122] G. Olivo, O. Cussó, M. Borrell, M. Costas, *JBIC Journal of Biological Inorganic Chemistry* **2017**, *22*, 425-452.

[123] R. Mas-Ballesté, L. Que, *Journal of the American Chemical Society* **2007**, *129*, 15964-15972.

[124] M. S. Chen, M. C. White, *Science* **2007**, *318*, 783-787.

[125] K. Chen, M. Costas, J. Kim, A. K. Tipton, L. Que, *Journal of the American Chemical Society* **2002**, *124*, 3026-3035.

[126] A. Company, L. Gómez, M. Güell, X. Ribas, J. M. Luis, L. Que, M. Costas, *Journal of the American Chemical Society* **2007**, *129*, 15766-15767.

[127] M. J. Ingleson, R. A. Layfield, *Chem. Commun.* **2012**, *48*, 3579-3589.

[128] J. A. Mata, M. Poyatos, E. Peris, *Coord. Chem. Rev.* **2007**, *251*, 841-859.

[129] A. Raba, M. Cokoja, S. Ewald, K. Riener, E. Herdtweck, A. Pöthig, W. A. Herrmann, F. E. Kühn, *Organometallics* **2012**, *31*, 2793-2800.

[130] J. W. Kück, A. Raba, I. I. E. Markovits, M. Cokoja, F. E. Kühn, *ChemCatChem* **2014**, *6*, 1882-1886.

[131] M. R. Anneser, S. Haslinger, A. Pöthig, M. Cokoja, J.-M. Basset, F. E. Kühn, *Inorg. Chem.* **2015**, *54*, 3797-3804.

[132] J. W. Kück, M. R. Anneser, B. Hofmann, A. Pöthig, M. Cokoja, F. E. Kühn, *ChemSusChem* **2015**, *8*, 4056-4063.

[133] M. A. Bernd, F. Dyckhoff, B. J. Hofmann, A. D. Böth, J. F. Schlagintweit, J. Oberkofler, R. M. Reich, F. E. Kühn, *J. Catal.* **2020**, *391*, 548-561.

[134] K. Öfele, *J. Organomet. Chem.* **1968**, *12*, P42-P43.

[135] H.-W. Wanzlick, H.-J. Schönherr, *Angewandte Chemie International Edition in English* **1968**, *7*, 141-142.

[136] R. R. Schrock, *Journal of the American Chemical Society* **1974**, *96*, 6796-6797.

[137] K. H. Dötz, J. Stendel, *Chem. Rev.* **2009**, *109*, 3227-3274.

[138] J. H. Wengrovius, R. R. Schrock, M. R. Churchill, J. R. Missert, W. J. Youngs, *Journal of the American Chemical Society* **1980**, *102*, 4515-4516.

[139] C. P. Casey, ACS Publications, **2006**.

[140] E. O. Fischer, A. Maasböl, *Angew. Chem.* **1964**, *76*, 645-645.

[141] A. J. Arduengo, R. L. Harlow, M. Kline, *Journal of the American Chemical Society* **1991**, *113*, 361-363.

[142] V. P. Böhm, W. A. Herrmann, *Angew. Chem. Int. Ed.* **2000**, *39*, 4036-4038.

[143] W. A. Herrmann, *Angew. Chem. Int. Ed.* **2002**, *41*, 1290-1309.

[144] M. Teci, E. Brenner, D. Matt, C. Gourlaouen, L. Toupet, *Dalton Trans* **2015**, *44*, 9260-9268.

[145] M. N. Hopkinson, C. Richter, M. Schedler, F. Glorius, *Nature* **2014**, *510*, 485-496.

[146] H. V. Huynh, *Chem. Rev.* **2018**, *118*, 9457-9492.

[147] F. E. Hahn, M. C. Jahnke, *Angew. Chem. Int. Ed.* **2008**, *47*, 3122-3172.

[148] D. Bourissou, O. Guerret, F. P. Gabbaï, G. Bertrand, *Chem. Rev.* **2000**, *100*, 39-92.

[149] T. P. Schlachta, F. E. Kühn, *Chem. Soc. Rev.* **2023**, *52*, 2238-2277.

[150] W. A. Herrmann, M. Elison, J. Fischer, C. Köcher, G. R. Artus, *Angewandte Chemie International Edition in English* **1995**, *34*, 2371-2374.

[151] A. J. Arduengo III, H. R. Dias, R. L. Harlow, M. Kline, *Journal of the American Chemical Society* **1992**, *114*, 5530-5534.

[152] C. Heinemann, T. Müller, Y. Apeloig, H. Schwarz, *Journal of the American Chemical Society* **1996**, *118*, 2023-2038.

[153] W. A. Herrmann, *Angew. Chem. Int. Ed.* **2002**, *41*, 1290-1309.

[154] E. A. B. Kantchev, C. J. O'Brien, M. G. Organ, *Angew. Chem. Int. Ed.* **2007**, *46*, 2768-2813.

[155] F. Glorius, *N-Heterocyclic Carbenes in Transition Metal Catalysis,* Springer-Verlag Berlin Heidelberg: **2007**.

[156] H. V. Huynh, Y. Han, R. Jothibasu, J. A. Yang, *Organometallics* **2009**, *28*, 5395-5404.

[157] M. N. Hopkinson, F. Glorius, in *N-Heterocyclic Carbenes in Organocatalysis*, **2018**, pp. 1-35.

[158] C. Barnett, M. L. Cole, J. B. Harper, *ACS Omega* **2022**, *7*, 34657-34664.

[159] Y. Han, H. V. Huynh, G. K. Tan, *Organometallics* **2007**, *26*, 6447-6452.

[160] D. Yuan, H. V. Huynh, *Organometallics* **2012**, *31*, 405-412.

[161] Q. Teng, H. V. Huynh, *Dalton Trans* **2017**, *46*, 614-627.

[162] S. Guo, H. Sivaram, D. Yuan, H. V. Huynh, *Organometallics* **2013**, *32*, 3685-3696.

[163] C. A. Tolman, *Chem. Rev.* **1977**, *77*, 313-348.

[164] G. Meng, L. Kakalis, S. P. Nolan, M. Szostak, *Tetrahedron Lett.* **2019**, *60*, 378-381.

[165] K. Verlinden, H. Buhl, W. Frank, C. Ganter, *Eur. J. Inorg. Chem.* **2015**, *2015*, 2416-2425.

[166] G. Ciancaleoni, N. Scafuri, G. Bistoni, A. Macchioni, F. Tarantelli, D. Zuccaccia, L. Belpassi, *Inorg. Chem.* **2014**, *53*, 9907-9916.

[167] E. L. Rosen, C. D. Varnado, Jr., A. G. Tennyson, D. M. Khramov, J. W. Kamplain, D. H. Sung, P. T. Cresswell, V. M. Lynch, C. W. Bielawski, *Organometallics* **2009**, *28*, 6695-6706.

[168] M. Braun, W. Frank, G. J. Reiss, C. Ganter, *Organometallics* **2010**, *29*, 4418-4420.

[169] V. N. Nemykin, D. E. Nevonen, W. R. Osterloh, L. S. Ferch, L. A. Harrison, B. S. Marx, K. M. Kadish, *Inorg. Chem.* **2021**, *60*, 16626-16644.

[170] A. B. P. Lever, *Inorg. Chem.* **1990**, *29*, 1271-1285.

[171] P. de Frémont, N. Marion, S. P. Nolan, *Coord. Chem. Rev.* **2009**, *253*, 862-892.

[172] L. Benhamou, E. Chardon, G. Lavigne, S. Bellemin-Laponnaz, V. César, *Chem. Rev.* **2011**, *111*, 2705-2733.

[173] H. M. Wang, I. J. Lin, *Organometallics* **1998**, *17*, 972-975.

[174] F. Glorius, S. Bellemin-Laponnaz, *N-heterocyclic carbenes in transition metal catalysis,* Springer Science & Business Media: **2007**.

[175] W. A. Herrmann, C. Köcher, *Angewandte Chemie International Edition in English* **1997**, *36*, 2162-2187.

[176] N. Kuhn, T. Kratz, *Synthesis* **1993**, *1993*, 561-562.

[177] M. K. Denk, A. Hezarkhani, F. L. Zheng, Wiley Online Library, **2007**.

[178] K. Riener, S. Haslinger, A. Raba, M. P. Högerl, M. Cokoja, W. A. Herrmann, F. E. Kühn, *Chem. Rev.* **2014**, *114*, 5215-5272.

[179] M. V. Baker, B. W. Skelton, A. H. White, C. C. Williams, *Organometallics* **2002**, *21*, 2674-2678.

[180] F. E. Hahn, V. Langenhahn, T. Lügger, T. Pape, D. Le Van, *Angew. Chem. Int. Ed.* **2005**, *44*, 3759-3763.

[181] R. McKie, J. A. Murphy, S. R. Park, M. D. Spicer, S. z. Zhou, *Angew. Chem.* **2007**, *119*, 6645-6648.

[182]   S. A. Cramer, D. M. Jenkins, *J. Am. Chem. Soc.* **2011**, *133*, 19342-19345.

[183]   S. Meyer, I. Klawitter, S. Demeshko, E. Bill, F. Meyer, *Angew. Chem. Int. Ed.* **2013**, *52*, 901-905.

[184]   F. Dyckhoff, J. F. Schlagintweit, M. A. Bernd, C. H. G. Jakob, T. P. Schlachta, B. J. Hofmann, R. M. Reich, F. E. Kühn, *Catal. Sci. Technol.* **2021**, *11*, 795-799.

[185]   M. A. Bernd, E. B. Bauer, J. Oberkofler, A. Bauer, R. M. Reich, F. E. Kühn, *Dalton Trans* **2020**, *49*, 14106-14114.

[186]   E. B. Bauer, M. A. Bernd, M. Schütz, J. Oberkofler, A. Pöthig, R. M. Reich, F. E. Kühn, *Dalton Trans* **2019**, *48*, 16615-16625.

[187]   F. Bray, M. Laversanne, H. Sung, J. Ferlay, R. L. Siegel, I. Soerjomataram, A. Jemal, *CA: A Cancer Journal for Clinicians* **2024**, *74*, 229-263.

[188]   E. Farber, R. Cameron, in *Advances in Cancer Research, Vol. 31* (Eds.: G. Klein, S. Weinhouse), Academic Press, **1980**, pp. 125-226.

[189]   W. Clark, *British journal of cancer* **1991**, *64*, 631-644.

[190]   D. Hanahan, R. A. Weinberg, *cell* **2000**, *100*, 57-70.

[191]   D. Hanahan, R. A. Weinberg, *cell* **2011**, *144*, 646-674.

[192]   S. Sarkar, G. Horn, K. Moulton, A. Oza, S. Byler, S. Kokolus, M. Longacre, *International journal of molecular sciences* **2013**, *14*, 21087-21113.

[193]   B. Vogelstein, K. W. Kinzler, *Nature medicine* **2004**, *10*, 789-799.

[194]   R. A. Weinberg, R. A. Weinberg, *The biology of cancer,* WW Norton & Company: **2006**.

[195]   A. Sochacka-Ćwikła, M. Mączyński, A. Regiec, *Molecules* **2022**, *27*, 2259.

[196]   D. A. Haber, N. S. Gray, J. Baselga, *Cell* **2011**, *145*, 19-24.

[197]   T. Jain, V. Dudeja, *Nature reviews Gastroenterology & hepatology* **2021**, *18*, 99-100.

[198]   V. Schirrmacher, *Int. J. Oncol.* **2019**, *54*, 407-419.

[199]   R. A. De Mello, Á. Tavares, G. Mountzios, **2019**.

[200]   M. K. Kirkwood, A. Hanley, S. S. Bruinooge, E. Garrett-Mayer, L. A. Levit, C. Schenkel, J. E. Seid, B. N. Polite, R. L. Schilsky, *Journal of Oncology Practice* **2018**, *14*, e412-e420.

[201]   R. J. Bold, P. M. Termuhlen, D. J. McConkey, *Surgical oncology* **1997**, *6*, 133-142.

[202]   R. Ralhan, J. Kaur, *Expert Opinion on Therapeutic Patents* **2007**, *17*, 1061-1075.

[203]   D. D. Oliveira, T. J. J. D. Lapierre, F. C. Silva, I. V. Cunha, R. A. Souza, P. A. Matos, G. M. Almeida, C. G. Oliveira, T. G. Araújo, T. M. Tsubone, *Journal of the Brazilian Chemical Society* **2024**, *35*, e-20230128.

[204]   H. Wolff, *Klinische Wochenschrift* **1965**, *43*, 819-821.

[205]   H. H. Tessler, in *Intraocular Inflammation*, Springer, **2016**, pp. 315-321.

[206]   S. Dhillon, *Drugs* **2021**, *81*, 963-969.

[207]   A. Emadi, R. J. Jones, R. A. Brodsky, *Nature Reviews Clinical Oncology* **2009**, *6*, 638-647.

[208]   J. Germanas, A. G. Pandya, *Dermatologic Therapy* **2002**, *15*, 317-324.

[209] D. B. Zamble, S. J. Lippard, *Trends Biochem. Sci* **1995**, *20*, 435-439.

[210] S. Cruet-Hennequart, M. T. Glynn, L. S. Murillo, S. Coyne, M. P. Carty, *DNA Repair* **2008**, *7*, 582-596.

[211] M. Tiwari, *Journal of Cancer Research & Therapeutics* **2012**, *8*.

[212] W. B. Parker, *Chem. Rev.* **2009**, *109*, 2880-2893.

[213] G. H. Elgemeie, *Current pharmaceutical design* **2003**, *9*, 2627-2642.

[214] L. A. Smith, V. R. Cornelius, C. J. Plummer, G. Levitt, M. Verrill, P. Canney, A. Jones, *BMC cancer* **2010**, *10*, 1-14.

[215] G. L. Beretta, F. Zunino, *Anthracycline Chemistry and Biology II: Mode of action, clinical aspects and new drugs* **2008**, 1-19.

[216] S. Rivankar, *Journal of cancer research and therapeutics* **2014**, *10*, 853-858.

[217] R. J. van Vuuren, M. H. Visagie, A. E. Theron, A. M. Joubert, *Cancer chemotherapy and pharmacology* **2015**, *76*, 1101-1112.

[218] S. Dall'Acqua, *Curr. Top. Med. Chem.* **2014**, *14*, 2272-2285.

[219] H.-Z. Lee, B. W. Miller, V. E. Kwitkowski, S. Ricci, P. DelValle, H. Saber, J. Grillo, J. Bullock, J. Florian, N. Mehrotra, *Clinical Cancer Research* **2014**, *20*, 3902-3907.

[220] F. Esma, M. Salvini, R. Troia, M. Boccadoro, A. Larocca, C. Pautasso, *Expert opinion on pharmacotherapy* **2017**, *18*, 1127-1136.

[221] A. C. Krauss, X. Gao, L. Li, M. L. Manning, P. Patel, W. Fu, K. G. Janoria, G. Gieser, D. A. Bateman, D. Przepiorka, *Clinical Cancer Research* **2019**, *25*, 2685-2690.

[222] B. S. Chhikara, K. Parang, *Expert opinion on drug delivery* **2010**, *7*, 1399-1414.

[223] L. Lennard, *European journal of clinical pharmacology* **1992**, *43*, 329-339.

[224] F. O. Smith, G. H. Reaman, in *Pediatric Cancer Therapeutics Development*, Springer, **2022**, pp. 1-8.

[225] C. Carvalho, R. X. Santos, S. Cardoso, S. Correia, P. J. Oliveira, M. S. Santos, P. I. Moreira, *Current medicinal chemistry* **2009**, *16*, 3267-3285.

[226] J. Škubník, V. S. Pavlíčková, T. Ruml, S. Rimpelová, *Biology* **2021**, *10*, 849.

[227] J. F. Holland, C. Scharlau, S. Gailani, M. J. Krant, K. B. Olson, J. Horton, B. I. Shnider, J. J. Lynch, A. Owens, P. P. Carbone, *Cancer research* **1973**, *33*, 1258-1264.

[228] M. Markman, T. M. Mekhail, *Expert opinion on pharmacotherapy* **2002**, *3*, 755-766.

[229] E. A. Perez, *The oncologist* **1998**, *3*, 373-389.

[230] M. Green, G. Manikhas, S. Orlov, B. Afanasyev, A. Makhson, P. Bhar, M. Hawkins, *Annals of oncology* **2006**, *17*, 1263-1268.

[231] K. Barabas, R. Milner, D. Lurie, C. Adin, *Veterinary and comparative oncology* **2008**, *6*, 1-18.

[232] C. A. Rabik, M. E. Dolan, *Cancer treatment reviews* **2007**, *33*, 9-23.

[233] N. Graf, W. H. Ang, G. Zhu, M. Myint, S. J. Lippard, *Chembiochem* **2011**, *12*, 1115-1123.

[234] A.-M. Tsimberidou, *Cancer chemotherapy and pharmacology* **2015**, *76*, 1113-1132.

[235] J. B. Gibbs, *Science* **2000**, *287*, 1969-1973.

[236] P. L. Bedard, D. M. Hyman, M. S. Davids, L. L. Siu, *The Lancet* **2020**, *395*, 1078-1088.

[237] E. Buchdunger, T. O'Reilley, J. Wood, *European journal of cancer* **2002**, *38*, S28-S36.

[238] C. H. Johansson, S. E. Brage, *Pharmacology & therapeutics* **2014**, *142*, 176-182.

[239] P. A. Trail, D. H. King, G. M. Dubowchik, *Cancer Immunology, Immunotherapy* **2003**, *52*, 328-337.

[240] G. P. Adams, L. M. Weiner, *Nat. Biotechnol.* **2005**, *23*, 1147-1157.

[241] J. Albanell, J. Codony, A. Rovira, B. Mellado, P. Gascón, in *New Trends in Cancer for the 21 st Century: Proceedings of the International Symposium on Cancer: New Trends in Cancer for the 21 st Century, held November 10–13, 2002, in Valencia, Spain*, Springer, **2003**, pp. 253-268.

[242] C. J. Lord, A. Ashworth, *Curr. Opin. Pharmacol.* **2008**, *8*, 363-369.

[243] Y. Chen, H. Du, *Biomedicine & Pharmacotherapy* **2018**, *99*, 552-560.

[244] B. Peng, P. Lloyd, H. Schran, *Clinical pharmacokinetics* **2005**, *44*, 879-894.

[245] N. Vasan, J. Baselga, D. M. Hyman, *Nature* **2019**, *575*, 299-309.

[246] I. Yousuf, M. Bashir, F. Arjmand, S. Tabassum, *Coord. Chem. Rev.* **2021**, *445*, 214104.

[247] M. Peyrone, *Justus Liebigs Annalen der Chemie* **1844**, *51*, 1-29.

[248] B. Rosenberg, L. VanCamp, *Cancer research* **1970**, *30*, 1799-1802.

[249] L. Kelland, *Nature Reviews Cancer* **2007**, *7*, 573-584.

[250] S. Dasari, P. B. Tchounwou, *Eur. J. Pharmacol.* **2014**, *740*, 364-378.

[251] F. M. Muggia, A. Bonetti, J. D. Hoeschele, M. Rozencweig, S. B. Howell, *Journal of Clinical Oncology* **2015**, *33*, 4219-4226.

[252] C. H. Yarbro, *Seminars in Oncology Nursing* **1989**, *5*, 63-69.

[253] A. Stein, D. Arnold, *Expert Opinion on Pharmacotherapy* **2012**, *13*, 125-137.

[254] S. Alassadi, M. J. Pisani, N. J. Wheate, *Dalton Trans* **2022**, *51*, 10835-10846.

[255] T. C. Johnstone, K. Suntharalingam, S. J. Lippard, *Chem. Rev.* **2016**, *116*, 3436-3486.

[256] J. J. YU, X. YANG, Q. SONG, M. D. MUELLER, S. C. REMICK, *Anticancer Res.* **2014**, *34*, 455-463.

[257] T. Zou, C. T. Lum, C.-N. Lok, J.-J. Zhang, C.-M. Che, *Chem. Soc. Rev.* **2015**, *44*, 8786-8801.

[258] I. Kostova, *Anti-Cancer Agents in Medicinal Chemistry (Formerly Current Medicinal Chemistry - Anti-Cancer Agents)* **2006**, *6*, 19-32.

[259] M. Chaffman, R. Brogden, R. Heel, T. Speight, G. Avery, *Drugs* **1984**, *27*, 378-424.

[260] C. Roder, M. J. Thomson, *Drugs in R&D* **2015**, *15*, 13-20.

[261] H. A. Rothan, S. Stone, J. Natekar, P. Kumari, K. Arora, M. Kumar, *Virology* **2020**, *547*, 7-11.

[262] C. K. Mirabelli, R. K. Johnson, C. M. Sung, L. Faucette, K. Muirhead, S. T. Crooke, *Cancer research* **1985**, *45*, 32-39.

[263] C. Marzano, V. Gandin, A. Folda, G. Scutari, A. Bindoli, M. P. Rigobello, *Free Radical Biol. Med.* **2007**, *42*, 872-881.

[264] S. Nobili, E. Mini, I. Landini, C. Gabbiani, A. Casini, L. Messori, *Medicinal research reviews* **2010**, *30*, 550-580.

[265] C. I. Yeo, K. K. Ooi, E. R. Tiekink, *Molecules* **2018**, *23*, 1410.

[266] I. Ott, *Coord. Chem. Rev.* **2009**, *253*, 1670-1681.

[267] A. Holmgren, *Antioxidants & redox signaling* **2000**, *2*, 811-820.

[268] V. Gandin, A. P. Fernandes, M. P. Rigobello, B. Dani, F. Sorrentino, F. Tisato, M. Björnstedt, A. Bindoli, A. Sturaro, R. Rella, *Biochem. Pharmacol.* **2010**, *79*, 90-101.

[269] A. Bindoli, M. P. Rigobello, G. Scutari, C. Gabbiani, A. Casini, L. Messori, *Coord. Chem. Rev.* **2009**, *253*, 1692-1707.

[270] S. Gromer, S. Urig, K. Becker, *Medicinal Research Reviews* **2004**, *24*, 40-89.

[271] J. Nordberg, E. S. Arnér, *Free Radical Biol. Med.* **2001**, *31*, 1287-1312.

[272] A. Casini, R. W.-Y. Sun, I. Ott, *Met. Ions Life Sci* **2018**, *18*, 9783110470734-9783110470013.

[273] P. J. Barnard, S. J. Berners-Price, *Coord. Chem. Rev.* **2007**, *251*, 1889-1902.

[274] E. S. Arnér, A. Holmgren, *Eur. J. Biochem.* **2000**, *267*, 6102-6109.

[275] S. Gromer, L. D. Arscott, C. H. Williams, R. H. Schirmer, K. Becker, *J. Biol. Chem.* **1998**, *273*, 20096-20101.

[276] B. Yu, L. Ma, J. Jin, F. Jiang, G. Zhou, K. Yan, Y. Liu, *Toxicology Research* **2018**, *7*, 1081-1090.

[277] P. Nagakannan, E. Eftekharpour, *Free Radical Biol. Med.* **2017**, *108*, 819-831.

[278] S. J. Berners-Price, A. Filipovska, *Metallomics* **2011**, *3*, 863-873.

[279] E. R. Tiekink, *Critical reviews in oncology/hematology* **2002**, *42*, 225-248.

[280] S. J. Berners-Price, P. J. Barnard, *Ligand Design in Medicinal Inorganic Chemistry* **2014**, 227-256.

[281] J. L. Hickey, R. A. Ruhayel, P. J. Barnard, M. V. Baker, S. J. Berners-Price, A. Filipovska, *Journal of the American Chemical Society* **2008**, *130*, 12570-12571.

[282] P. Zou, M. Chen, J. Ji, W. Chen, X. Chen, S. Ying, J. Zhang, Z. Zhang, Z. Liu, S. Yang, *Oncotarget* **2015**, *6*, 36505.

[283] X. Cheng, P. Holenya, S. Can, H. Alborzinia, R. Rubbiani, I. Ott, S. Wölfl, *Molecular cancer* **2014**, *13*, 1-15.

[284] O. z. Karaca, V. Scalcon, S. M. Meier-Menches, R. Bonsignore, J. M. Brouwer, F. Tonolo, A. Folda, M. P. Rigobello, F. E. Kühn, A. Casini, *Inorg. Chem.* **2017**, *56*, 14237-14250.

[285] L. Oehninger, R. Rubbiani, I. Ott, *Dalton Trans* **2013**, *42*, 3269-3284.

[286] M. J. Matos, C. Labão-Almeida, C. Sayers, O. Dada, M. Tacke, G. J. L. Bernardes, *Chemistry – A European Journal* **2018**, *24*, 12250-12253.

[287] M. V. Baker, P. J. Barnard, S. J. Berners-Price, S. K. Brayshaw, J. L. Hickey, B. W. Skelton, A. H. White, *Dalton Trans* **2006**, 3708-3715.

[288] J. L. Hickey, R. A. Ruhayel, P. J. Barnard, M. V. Baker, S. J. Berners-Price, A. Filipovska, *Journal of the American Chemical Society* **2008**, *130*, 12570-12571.

[289] J. S. Modica-Napolitano, J. R. Aprille, *Advanced Drug Delivery Reviews* **2001**, *49*, 63-70.

[290] L. B. Chen, *Annual review of cell biology* **1988**, *4*, 155-181.

[291] L. Stefan, B. Bertrand, P. Richard, P. Le Gendre, F. Denat, M. Picquet, D. Monchaud, *ChemBioChem* **2012**, *13*, 1905-1912.

[292] B. Bertrand, L. Stefan, M. Pirrotta, D. Monchaud, E. Bodio, P. Richard, P. Le Gendre, E. Warmerdam, M. H. de Jager, G. M. M. Groothuis, M. Picquet, A. Casini, *Inorg. Chem.* **2014**, *53*, 2296-2303.

[293] M. Mora, M. C. Gimeno, R. Visbal, *Chem. Soc. Rev.* **2019**, *48*, 447-462.

[294] I. Ott, in *Inorganic and Organometallic Transition Metal Complexes with Biological Molecules and Living Cells*, Elsevier, **2017**, pp. 147-179.

[295] T. Zou, C.-N. Lok, P.-K. Wan, Z.-F. Zhang, S.-K. Fung, C.-M. Che, *Curr. Opin. Chem. Biol.* **2018**, *43*, 30-36.

[296] C.-P. Tan, Y.-Y. Lu, L.-N. Ji, Z.-W. Mao, *Metallomics* **2014**, *6*, 978-995.

[297] I. Ott, in *Adv. Inorg. Chem., Vol. 75*, Elsevier, **2020**, pp. 121-148.

[298] S. M. Meier-Menches, A. Casini, *Bioconjugate Chem.* **2020**, *31*, 1279-1288.

[299] Brian Buntz. 2024. "Top pharma companies ranked by 2023 R&D spend." accessed 29.10.2024. https://www.drugdiscoverytrends.com/top-pharma-companies-2023-rd-spend/.

[300] E. H. Rubin, D. G. Gilliland, *Nature Reviews Clinical Oncology* **2012**, *9*, 215-222.

[301] C. Ge, K. Guo, Y. Li, G. Li, H. Zhang, J. Yang, Y. Liu, C. Yin, S. Liu, S. Xie, X. Chen, *eClinicalMedicine* **2023**, *59*.

[302] I. Khanna, *Drug Discovery Today* **2012**, *17*, 1088-1102.

[303] C. G. Begley, L. M. Ellis, *Nature* **2012**, *483*, 531-533.

[304] M. Herper, *Vol. 189*, FORBES INC 60 FIFTH AVE, NEW YORK, NY 10011 USA, **2012**, pp. 38-38.

[305] P. A. Dieppe, S. Ebrahim, R. M. Martin, P. Jüni, *Vol. 329*, British Medical Journal Publishing Group, **2004**, pp. 867-868.

[306] C. D. Furberg, B. Pitt, *Trials* **2001**, *2*, 205.

[307] A. Colpo.

[308] J. M. Brophy, *Indian Journal of Medical Ethics* **2016**, *1*, 224-226.

[309] M. Hay, D. W. Thomas, J. L. Craighead, C. Economides, J. Rosenthal, *Nat. Biotechnol.* **2014**, *32*, 40-51.

[310] W. Mück, *Clinical Pharmacokinetics* **2000**, *39*, 99-116.

[311] J. L. Hillson, D. E. Furst, *Expert Opinion on Pharmacotherapy* **2000**, *1*, 1053-1066.

[312]   F. S. Collins, L. A. Tabak, *Nature* **2014**, *505*, 612-613.

[313]   C. G. Begley, J. P. A. Ioannidis, *Circulation Research* **2015**, *116*, 116-126.

[314]   F. Fidler, J. Wilcox, **2018**.

[315]   J. E. Boylan, *IMA Journal of Management Mathematics* **2016**, *27*, 107-108.

[316]   A. Mobley, S. K. Linder, R. Braeuer, L. M. Ellis, L. Zwelling, *PloS one* **2013**, *8*, e63221.

[317]   M. Koo, S.-C. Lin, *Heliyon* **2024**, *10*.

[318]   N. A. Vasilevsky, M. H. Brush, H. Paddock, L. Ponting, S. J. Tripathy, G. M. LaRocca, M. A. Haendel, *PeerJ* **2013**, *1*, e148.

[319]   J. K. Hartshorne, A. Schachner, *Frontiers in computational neuroscience* **2012**, *6*, 8.

[320]   N. Schaduangrat, S. Lampa, S. Simeon, M. P. Gleeson, O. Spjuth, C. Nantasenamat, *Journal of cheminformatics* **2020**, *12*, 1-30.

[321]   M. G. O. Lorenz, *SLAS Technology* **2004**, *9*, 262-267.

[322]   L. P. Freedman, I. M. Cockburn, T. S. Simcoe, *PLoS biology* **2015**, *13*, e1002165.

[323]   B. Miles, P. L. Lee, *SLAS TECHNOLOGY: Translating Life Sciences Innovation* **2018**, *23*, 432-439.

[324]   J. L. Almeida, K. D. Cole, A. L. Plant, *PLoS biology* **2016**, *14*, e1002476.

[325]   A. Capes-Davis, R. M. Neve, *PLoS biology* **2016**, *14*, e1002477.

[326]   M. Yu, **2019**.

[327]   G. Schneider, *Nature reviews drug discovery* **2018**, *17*, 97-113.

[328]   M. Nettekoven, A. W. Thomas, *Current medicinal chemistry* **2002**, *9*, 2179-2190.

[329]   J. Jiménez-Luna, F. Grisoni, N. Weskamp, G. Schneider, *Expert opinion on drug discovery* **2021**, *16*, 949-959.

[330]   K.-K. Mak, Y.-H. Wong, M. R. Pichika, *Drug discovery and evaluation: safety and pharmacokinetic assays* **2024**, 1461-1498.

[331]   W. R. Büchele, T. P. Schlachta, A. L. Gebendorfer, J. Pamperin, L. F. Richter, M. J. Sauer, A. Prokop, F. E. Kühn, *RSC Adv.* **2024**, *14*, 10244-10254.

[332]   L. F. Richter, W. R. E. Büchele, A. Imhof, F. E. Kühn, *HardwareX* **2024**, *20*, e00581.

[333]   G. R. Fulmer, A. J. M. Miller, N. H. Sherden, H. E. Gottlieb, A. Nudelman, B. M. Stoltz, J. E. Bercaw, K. I. Goldberg, *Organometallics* **2010**, *29*, 2176-2179.

[334]   M. A. Bernd, Marcocyclic Tetra-dentate NHC Complexes for Catalysis and Medicinal Chemistry, PhD thesis, Technical University of Munich (Garching, Germany), **2021**.

Synthesis, characterization, and biomedical evaluation of ethylene-bridged tetra-NHC Pd(II), Pt(II) and Au(III) complexes, with apoptosis-inducing properties in cisplatin-resistant neuroblastoma cells†

Wolfgang R. E. Büchele, [iD] ‡[a] Tim P. Schlachta, [iD] ‡[a] Andreas L. Gebendorfer,[a] Jenny Pamperin,[cd] Leon F. Richter, [iD] [a] Michael J. Sauer,[a] Aram Prokop*[bcd] and Fritz E. Kühn [iD] *[a]

Synthesis and characterization of the first two cyclic ethylene-bridged tetradentate NHC ligands, with an unsaturated (imidazole) and saturated backbone (2-imidazoline), are described. Complexes of both ligands containing palladium(II) have been obtained. For platinum(II) and gold(III), only the unsaturated tetracarbene complexes could be isolated. The attempts to synthesize a methylene-bridged 2-imidazoline macrocycle are also described. Furthermore, a novel bisimidazolinium ligand precursor and its open-chain Pd[II] and Pt[II] tetracarbene complexes are obtained. Finally, it is shown that the unsaturated gold(III) tetracarbene is able to induce apoptosis in malignant SK-N-AS neuroblastoma cells via the mitochondrial and ROS pathway and overcomes resistance to cisplatin in vitro.

Introduction

N-heterocyclic carbenes (NHCs), first described in 1991,[1] have found many applications.[2] There are several structural features that allow the tuning of their electronic properties. Ring size, the adjacent heteroatoms, N-substituents, and the backbone can be modified. Changing one or more structural properties of a NHC ligand can lead to significantly different reactivities and stabilities of the resulting complexes.[3] Often several NHC units are combined in multidentate ligands, making use of the chelating effect, and a plethora of multidentate NHC metal complexes has been reported.[4,5]

Our group has developed several bidentate and cyclic tetradentate NHC ligands. The respective transition metal complexes have been applied e.g. in medicinal chemistry[6,7] and epoxidation catalysis.[3] While the bidentate ligands can form open-chain tetracarbene complexes,[8,9] the tetradentate ligands give cyclic tetracarbene compounds. Most commonly applied in our recent examinations is the calix[4]imidazolium ligand precursor (a, Fig. 1).[10] Its iron complex (c) can be used as olefin epoxidation catalyst achieving unprecedented activity.[3] Coinage metal tetracarbene complexes (and metal NHC complexes in general[11–17]) have been investigated regarding their antiproliferative activity and selectivity against cancer cells (b, d–f, Fig. 1).[6,7]

[a]Technical University of Munich, School of Natural Sciences, Department of Chemistry and Catalysis Research Center, Molecular Catalysis, Lichtenbergstraße 4, 85748 Garching, Germany. E-mail: fritz.kuehn@ch.tum.de; Tel: +49 89 289 13477

[b]Department of Pediatric Hematology/Oncology, Children's Hospital Cologne, Amsterdamer Straße 59, 50735 Cologne, Germany

[c]Department of Pediatric Oncology/Hematology, Helios Clinics Schwerin, Wismarsche Straße 393-397, 19055 Schwerin, Germany. E-mail: aram.prokop@helios-gesundheit.de

[d]Department of Human Medicine, MSH Medical School Hamburg, Am Kaiserkai 1, 20457 Hamburg, Germany

‡ These authors contributed equally to this work.
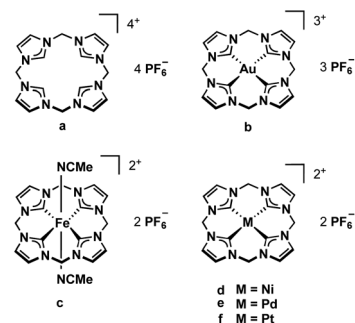
Fig. 1 Tetracarbene ligand precursor a and derived transition metal complexes b–f.

In this study, the scope of multidentate NHC ligands is extended with an ethylene-bridged bisimidazolinium ligand precursor and two cyclic ethylene-bridged tetradentate NHC ligands, with an unsaturated (imidazole) and saturated backbone (2-imidazoline). Pd[II], Pt[II] and Au[III] tetracarbene complexes containing the novel ligands are synthesized, characterized and applied in preliminary medicinal studies regarding their activity in inducing apoptosis in malignant cells. Finally, the synthetic attempts to a calix[4]imidazolinium macrocycle (structurally analog to **c** but with a saturated backbone) are described, because there is an increasing demand for reliable training data, including data on negative outcomes, for machine learning systems in chemistry.[18]

Especially the two new macrocyclic ligand precursors are intended to lay the foundation for electronic comparisons induced by the different backbone in future studies. The unsaturated backbone of the imidazole moiety causes partial aromaticity, increasing NHC stability by *ca.* 100 kJ mol^{-1}.[19–21] A saturated backbone, in turn, can lead to higher basicity because the electron density is more concentrated on the C2 carbene carbon atom due to the lack of π-interactions.[22]

Results and discussion

The synthesis of a saturated macrocyclic ligand precursor similar to **c**, but containing 2-imidazoline moieties instead of imidazole, calix[4]imidazolinium, was pursued parallel to the synthesis of the other ligand precursors. However, the synthesis was not successful with the chosen synthetic approaches as described in the ESI.†

Synthesis and characterization of H$_2$L3

H$_2$L3 is based on the literature known ethylene-bridged imidazoline moiety (**1**).[23] Alkylation of **1** with MeI in MeCN at 82 °C, followed by an anion exchange with NH$_4$PF$_6$ in water, gives **H$_2$L3** in 91% yield (Fig. 2).

Synthesis and characterization of H$_4$L5/6 and H$_4$L8/L9

For the preparation of **H$_4$L5/6** and **H$_4$L8/9**, a slightly modified literature procedure for similar macrocycles was used (Fig. 3).[10] Ring closure to form the macrocyclic imidazolium salt **a** is commonly achieved with CH$_2$(OTf)$_2$,[3] but also CH$_2$Br$_2$ is reported.[24] Here the ethylene-bridged imidazoline **1** (ref. 23) and the ethylene-bridged imidazole **7** (ref. 25) are reacted with ethylene bistriflate (**4**) under dry conditions at −45 °C over a period of 5 h in dry MeCN for **H$_4$L5** and **H$_4$L8** (see ESI†).
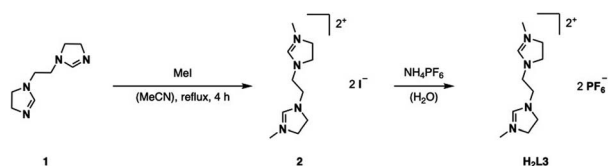
Fig. 2 Synthesis of ligand precursor H$_2$L3 *via* alkylation and anion exchange.
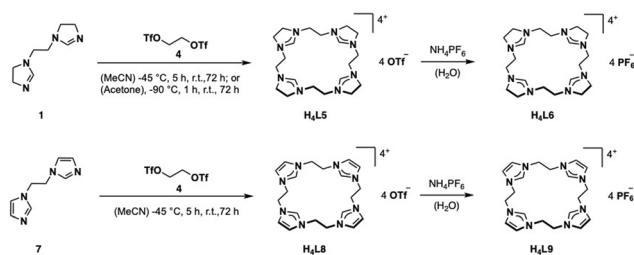
Fig. 3 Synthesis of ligand precursors H$_4$L5/6 and H$_4$L8/9 *via* ring closure with ethylene bistriflate and anion exchange.

The synthesis of **H$_4$L5** and **H$_4$L8** yields a mixture of a 20-membered macrocycle (87% **H$_4$L5** and 90% **H$_4$L8**, as determined by NMR), consisting of four imidazole (C[4]) units, and a 30-membered macrocycle (13% **H$_4$L5**, 10% **H$_4$L8**) consisting of six imidazole (C[6]) units (see ESI†). Separation attempts of C[4] and C[6] *via* column chromatography, precipitation or sublimation were not successful. However, by increasing the cooling period during the addition of the ethylene bistriflate at −45 °C to a total of 5 h, the purity of the kinetically preferred C[4] unit could be easily increased up to 98% C[4] for **H$_4$L5** and in case of **H$_4$L8** an increase up to 100% (ESI†). Due to the absence of similar macrocyclic imidazolinium compounds, **H$_4$L5** is compared to **a** and **H$_4$L8** in the following.[3]

Relative to **a**, all signals of **H$_4$L5** and **H$_4$L8** are upfield shifted, indicating a higher electronic density due to the +I effect of the ethylene bridge leading to an increased shielding effect in the NMR.[10,26] The higher upfield shift of **H$_4$L5** compared to **H$_4$L8** can be explained by the electronic inducing effect of the saturated bond.[20,26,27]

Unlike in ^{1}H-NMR, each individual ^{13}C signal of **H$_4$L8** in DMSO-d$_6$ is in the same range as the signals obtained for the macrocyclic compound **a**.[10] However, in case of **H$_4$L5**, opposite to the ^{1}H-NMR, the C2 carbon resonance at 159.16 ppm is downfield shifted compared to **H$_4$L8** and **a** (**H$_4$L8**, $\Delta\delta \leq$ 22.08 ppm, **a**, $\Delta\delta \leq$ 22.0 ppm), thus contradicting expectations. According to literature and as described by H. V. Huynh, the hypothetical free carbene of the imidazoline ligand **H$_4$L5** should be a stronger σ-donor than **H$_4$L8**, so an enhanced upfield shift of the C2 signal of **H$_4$L5** should have been detectable.[20,28,29] Interestingly this expectation is not met here, and apparently other factors play a role. Every other resonance in the ^{13}C-NMR is upfield shifted.[10]

Salt metathesis of the formed macrocyclic salts can be performed with NH$_4$PF$_6$ to increase the solubility in organic solvents and as additional purification step.[3,30] Thus, an anion exchange in water towards PF$_6^-$ is conducted with **H$_4$L5** and **H$_4$L8**, resulting in **H$_4$L6** (81%) and **H$_4$L9** (88%).

Synthesis and characterization of complexes (Pd/PtL3, PdL5/6, Pd/PtL8, Pd/AuL9)

A well-established route to obtain NHC complexes is to convert the corresponding imidazolium salts with group 10 metal acetates. In this reaction, the acetate serves as an internal base capable of deprotonating imidazolium- and imidazolinium

salts to form NHCs, which subsequently coordinate to the metal.[6,31–33] An alternative route is *via* a silver transmetalation.[34] In the first approaches, attempts were made to synthesize the respective Ag^I complex with **H$_2$L3** to obtain a dinuclear structure similar to already published open chain bis-NHC-complexes.[9,25,35] However, no product formation was observed in our case. Either no reaction took place or complex signals were observed in the aliphatic region of $\delta = 1.9$–4.4 ppm in the ^{1}H-NMR after purification, indicating the decomposition of **H$_2$L3**. Several other conditions with different Ag^I-salts and addition of sodium acetate as internal base at different temperatures were tested without success. A possible problem might be the stability of the Ag^I-complex. Another issue might be hydrolysis of imidazolines under acidic and basic conditions.[36,37] It has been proposed in literature that the moisture in the solvent can react with sodium acetate to generate hydroxide ions which can attack the electrophilic center of the C2 carbon and lead to ring-opening products, rather than nucleophilic attacking the acidic proton at the C2 carbon.[38] Therefore, the next attempts were conducted under moisture-free reaction conditions by using dried solvents. Even the direct metalation with palladium(II) acetate or palladium(II) chloride under dry reaction conditions did not lead to the desired product. The focus was then shifted to a combination of the transmetalation route using Ag$_2$O *in situ* with the direct metalation, by applying the respective metal precursor and sodium acetate as a mild base in dry solvents (Fig. 4).

The absence of the acidic imidazolinium proton signal and appearance of characteristic carbene carbon signals confirms the successful formation of **PdL3** and **PtL3**. Unfortunately, despite several attempts, a clean elemental analysis for **PtL3** could not be obtained. Also, the ^{1}H-NMR of **PtL3** shows some impurities, which could not be identified and no ^{195}Pt isotope coupling phenomena was observed in the ^{13}C-NMR.

The carbene carbon signal of **PdL3** at 194.29 ppm in DMSO-d$_6$ [**PtL3**; 188.38 ppm in CD$_3$CN], is surprisingly downfield shifted compared to other Pd(II) bis-NHCs reported in literature.[39,40] Due to the theoretically stronger σ-donation of the imidazolinylidene ligand **H$_2$L3** compared to its unsaturated analog, an upfield shift of the ^{13}C$_{NHC}$ signal was expected. Literature indicates that the significant downfield shift of the carbene carbon resonance from imidazolium to imidazolinium compounds is a general phenomenon.[38,41,42] Another interesting fact is that the analytic data, including HR-ESI-MS and elemental analysis, are not supporting a dinuclear complex or a mono-carbene complex as expected, but indicate that **PdL3** has rather a [**Pd(L3)$_2$**](PF$_6$)$_2$ structure similar to **e**. This is further
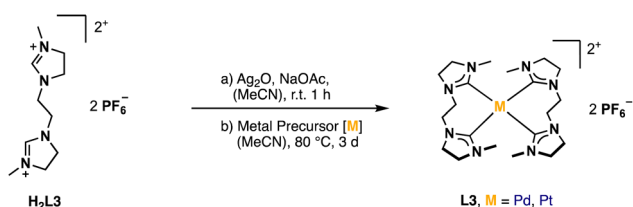
Fig. 5 ORTEP-style representation of the cationic fragment of complex **PdL3**. Hydrogen atoms and hexafluorophosphate anions are omitted for clarity. Thermal ellipsoids are shown at a 50% probability level. Selected bond lengths (Å) and angles (°): C1–Pd1 2.039(2); C7–Pd1 2.038(2); C7_a–Pd1–C7 180.0; C7–Pd1–C1_a 91.64(9); C7–Pd1–C1 88.36(9), C7_a–Pd1–C1_a–N2_a 55.30.

confirmed by single-crystal X-ray diffraction (SC-XRD). The **PdL3** complex displays a distorted square planar structure. Two **L3** ligands coordinate to the Pd center, resulting in an open-chain tetracarbene complex of similar geometry like the cyclic complex **e**.[34] The Pd–C (2.039 Å, 2.038 Å) distances are in good accord with palladium(II) NHC complexes reported in literature.[34,39] The alkyl groups of the ligand **L3** adopt a *syn* conformation in the solid state, while the imidazole rings are tilted by 55.30° out of the palladium square plane (Fig. 5).

The **PtL3** complex exhibits a similarly distorted square planar structure compared to **PdL3**. The Pt–C (2.033 Å, 2.039 Å) distances are comparable to similar literature known group 10 NHC compounds.[43–47] The alkyl groups of **L3** also adopt a *syn* conformation, while the imidazole rings are tilted by 50.53° out of the palladium square plane as in **PdL3** (Fig. 6).

Complex PdL5/6 and PdL8/9

Since **H$_4$L5** and **H$_4$L8** are quite similar to other macrocycles (**a**), it seemed suitable to synthesize **PdL5** and **PdL8** according to alike compounds *via* the direct metalation route.[32] Therefore, **H$_4$L8** was first converted with Pd(OAc)$_2$ in a mixture of dry

Fig. 6 ORTEP-style representation of the cationic fragment of complex **PtL3**. Hydrogen atoms and hexafluorophosphate anions are omitted for clarity. Thermal ellipsoids are shown at a 50% probability level. Selected bond lengths (Å) and angles (°): Pt1–C1 2.0337(18); Pt1–C7 2.039 (6), C1_a–Pt1–C1 180.00(7); C1–Pt1–C7_a 91.2(5); C1–Pt1–C7 88.8(5), C7_a–Pd1–C1_a–N2_a 50.53°.

Fig. 4 General synthesis of Pd/PtL3.
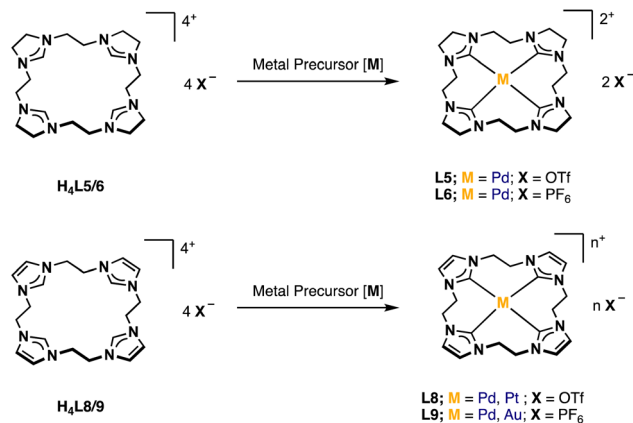
Fig. 7 General synthesis of **PdL5/6**, **Pd/PtL8** and **Pd/AuL9**.
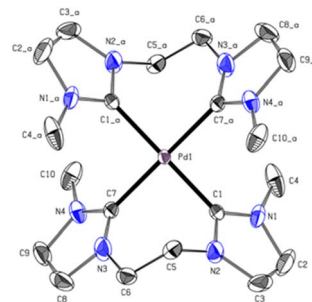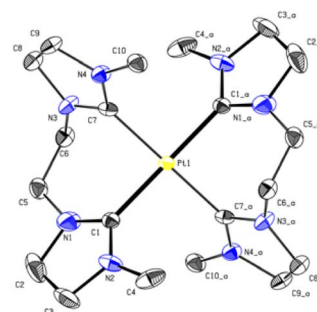

Fig. 8 ORTEP-style representation of the cationic fragment of complex **PdL9**. Hydrogen atoms and hexafluorophosphate anions are omitted for clarity. Thermal ellipsoids are shown at a 50% probability level. Selected bond lengths (Å) and angles (°): C1–Pd 2.019(2), C1–Pd1–C1_b 172.03(12), C1–Pd1–C1_d–N2_d 53.62, C5–Pd1–C5_b 98.97°.

DMSO/MeCN (1 : 1) at 40 °C for 16 h.[34] However, no product formation was observed after work-up. Several other conditions such as increasing temperature and reaction time led to the absence of the imidazolium protons and the formation of new product signals in the ^{1}H-NMR after 4 d at 80 °C. Still these intensities were very low, and no product could be isolated. Another approach was tried *via* the transmetalation route with Ag^I salts, but this also led to no product formation. Finally, both **PdL8** (50%, Fig. 7) and **PdL5** (3%) could be obtained by applying the same reaction conditions as for the already synthesized complexes **PdL3** and **PtL3**. The yield of the imidazolinylidene tetracarbene complex could be increased to 46%, by using **H$_4$L6** instead of **H$_4$L5**, resulting in **PdL6**.

Again, the absence of the acidic position 2 proton signals in the ^{1}H-NMR and appearance of the carbene carbon peaks confirm the formation of Pd(II) carbene complexes. The observed chemical shift of **PdL8** is in the typical range of Pd(II) tetra-NHC compounds and indicates the formation of a complex with similar coordination sphere as **e**.[6,34,45] The ^{1}H-NMR of **PdL5** in CD$_3$CN shows three signals, with two of them in a similar range to **PdL8** and one upfield shifted signal of the backbone protons. As already mentioned in the discussion of **H$_4$L5**, the ^{13}C-NMR of **PdL5** is contrary to expectations. The carbene carbon of **PdL5** (191.30 ppm) is surprisingly strong downfield shifted compared to **PdL8** (165.84 ppm) and in a similar range to the carbene carbon of **PdL3** (195.6 ppm in CD$_3$CN). Literature indicates that the significant downfield shift of the carbene carbon resonance from imidazole to imidazoline compounds is a general phenomenon.[38,41,42] The uncertainty of a ^{13}C-NMR measurement is expected to be below 0.1 ppm; by using three times the weighted standard deviation, a difference of >0.4 ppm is required for a significant difference that exceeds the statistic uncertainty.[3,48] Therefore, **PdL5** (191.30 ppm in CD$_3$CN) and **PdL8** (165.84 ppm in CD$_3$CN) show a sufficiently different chemical shift to allow its discussion. In general, the normal NHC unit (without any modification) of the tetracarbene ligands is in a range of rather low to negligible π-backdonation, hence the changes in electronic properties are dominated by the σ-donation of the tetracarbenes.[3,29] According to literature, the imidazoline ligand **L5** should be in general
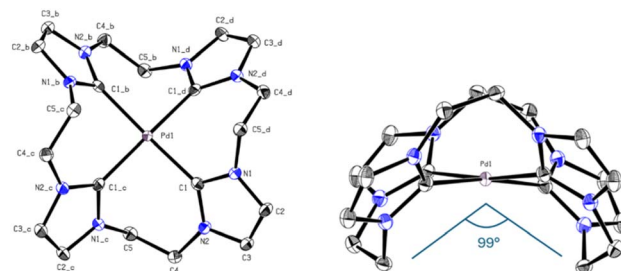
a stronger σ-donor than **L8**, so an enhanced upfield shift of the carbene signal would have been detectable.[3,20,28,29] Interestingly, this expectation is also not met here, and apparently other factors may play a role, as already observed with **PdL3** and **PtL3**. Therefore, further investigations on this subject, *e.g.* by means of DFT calculations, have to be carried out, since only conjectures can be made with the present analytical data. The elemental analysis and HR-ESI-MS for **PdL8** are in accord with a composition [**Pd(L8)**](OTf)$_2$ similar to **e**. It needs to be noted that no clean elemental analysis of **PdL6** could be obtained. However, the elemental analysis and HR-ESI-MS of **PdL6** are in accordance with the composition [**PdL6**](PF$_6$)$_2$. Due to unsatisfying results in crystallization of **PdL8**, an anion exchange in water towards PF$_6^-$ was conducted, resulting in **PdL9** (41%). Single crystals suitable for SC-XRD were obtained by slow diffusion of Et$_2$O into MeCN solution of **PdL9**. As expected, the Pd(II) ion is coordinated in a nearly square planar fashion with C–Pd–C angles deviating from 180° by ∼8°, thus lifting the metal slightly above the carbene carbon atom plane (Fig. 8). However, due to the C$_2$-bridge, the ligand is strongly bent (C5–Pd1–C5_b = 98.97°) and adopts a crisp-shape, while tilting the imidazole rings 53.62° in an alternating pattern out of the palladium square plane.[49] The Pd–C distance (2.019 Å) is comparable to those of other cyclic Pd(II) tetracarbene compounds reported in literature.[6,34,43,45–47]

In the following Table 1 the M–C$_{carbene}$ bond lengths [Å], the C$_{carbene}$–M–C$_{carbene}$ angle [°], the tilt of the NCN unit [°] of the complexes **Pd/PtL3** and **PdL9** and additionally the C$_{bridge}$–M–C$_{bridge}$ angle [°] for **PdL9** are summarized.

Table 1 Summary of the M–C$_{carbene}$ bond lengths [Å], the C$_{carbene}$–M–C$_{carbene}$ angle [°], the tilt of the NCN unit [°] of the complexes Pd/PtL3 and PdL9 and the C$_{bridge}$–M–C$_{bridge}$ angle [°] for **PdL9**

Compound	PdL3	PtL3	PdL9
M–C$_{carbene}$ [Å]	2.038|2.039	2.033|2.039	2.019
C$_{carbene}$–M–C$_{carbene}$ [°]	180	180	172.03
Tilt NCN unit [°]	55.30	50.53	53.62
C$_{bridge}$–M–C$_{bridge}$ [°]	—	—	98.97

Complex PtL8

Applying the same reaction conditions and work-up methods to $Pt(MeCN)_2Cl_2$ instead of $Pd(OAc)_2$ results in the formation of **PtL8** (25%, Fig. 7). The absence of acidic proton signals in the ^{1}H-NMR and the appearance of the carbene ^{13}C-peak at 159.39 ppm in CD_3CN confirms the formation of the respective Pt(II) complex. The chemical shift of the carbene carbon is in accordance with Pt(II) tetra-NHC complexes previously reported in literature and is slightly shifted to the upfield compared to **PdL8** ($^{13}C_{NHC}$ in CD_3CN at 165.84 ppm) by 6.45 ppm.[43,46,50] No ^{195}Pt isotope coupling was observed. The ^{1}H-NMR in CD_3CN shows similar signals compared to **PdL8**, where the bridge protons also split into two multiplets at 5.01 and 4.44 ppm. In addition, HR-ESI-MS is in accordance to a similar composition as **PdL8**. Despite multiple attempts, no single crystals suitable for SC-XRD were obtained. However, the discussed analytical data strongly support a similar structure compared to **PdL8** and similarly structured tetracarbene ligand.[6,34]

Complex AuL9

For the synthesis of **AuL9** (Fig. 7), the same reaction conditions were applied as reported in the literature for similar complexes.[51] Therefore, **H₄L8** was converted with $KAuCl_4$ and NaOAc in dry DMSO under exclusion of light at 100 °C for 5 h. After the work-up, including an ion exchange to PF_6^- as a purification step, **AuL9** (47%) was obtained. The absence of acidic proton signals in the ^{1}H-NMR and the appearance of a new ^{13}C-peak at 146.03 ppm in CD_3CN confirm the formation of the respective Au(III) complex. The chemical shift of the carbene carbon is in accord with Au(III) tetracarbene complex (**e**) previously reported in literature and slightly downfield shifted by 1.79 ppm when compared to **e**.[51] Furthermore, the backbone carbons are also slightly downfield shifted by 0.68 ppm. The ^{1}H-NMR in CD_3CN shows similar signals compared to complex **PdL8** and **PtL8** with the backbone protons at 7.47 ppm and the bridge protons as two multiplets in close proximity at 4.83 and 4.71 ppm. Both elemental analysis[52] and HR-ESI-MS are in agreement with the composition $[\textbf{Au(L15)}](PF_6)_3$. Although no single crystals suitable for SC-XRD were obtained, the discussed analytical data strongly support the coordination of one tetracarbene ligand similar to **PdL9**.

Biological evaluation

Induction of apoptosis as cell death type

PdL3, **PdL8**, **AuL9** and their respective protonated ligand precursors were tested for their apoptotic effects on Nalm-6 cells (human B cell precursor leukemia cell line) and SK-N-AS cells (human neuroblastoma cell line) at different concentrations and quantified by the nuclear DNA fragmentation by flow cytometry analysis. **PdL3** and **PdL8** as well as the ligand precursors do not show any apoptosis inducing effects in Nalm-6 cells and SK-N-AS cells (see ESI†). **AuL9** shows no apoptotic effect in Nalm-6 cells, but significant apoptosis induction by **AuL9** is detected in SK-N-AS cells (Fig. 9A); therefore, the effect of **AuL9** in SK-N-AS cells was further characterized.
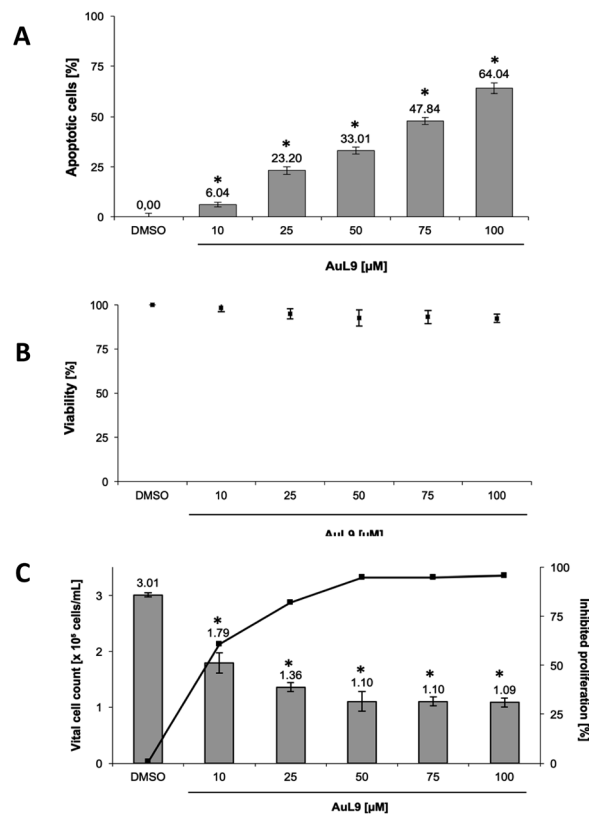
Fig. 9 (A) **AuL9** induces apoptosis in SK-N-AS cells. The cells were treated with different concentrations of **AuL9** and incubated for 96 h. Nuclear DNA fragmentation was analyzed. (B) To exclude unspecific cytotoxic effects, such as necrotic cell death, the viability of SK-N-AS cells was determined by measurement of LDH release into the medium after 2 h of incubation with different concentrations of **AuL9**. No significant LDH release could be detected in cells treated with **AuL9** up to a concentration of 100 μM. Values are given as mean% of DMSO control ± SD ($n = 3$). (C) The inhibition of proliferation of **AuL9** treated SK-N-AS cells was measured after 48 h using the CASY Cell-Counter System. A significant inhibition of cell growth was observed at concentrations as low as 10 μM. Inhibition of proliferation is given in mean% of control ± SD ($n = 3$); *: $p < 0.05$ vs. DMSO, t-test.

To exclude necrotic effects of **AuL9**, lactate dehydrogenase (LDH) leakage from SK-N-AS cells after 2 h incubation with **AuL9** was measured. LDH is released from the cell in case of necrosis and can be detected in the cell culture medium in case of loss of cell integrity and thus serves as a necrosis indicator.[53] **AuL9** shows no significant non-specific cytotoxic effects on SK-N-AS cells in the relevant concentration range up to 100 μM (Fig. 9B).

In addition to apoptosis induction, it was tested whether **AuL9** can inhibit the proliferation of malignant cells. For this purpose, SK-N-AS cells were incubated with different concentrations of **AuL9** for 48 hours. The proliferation inhibition was determined by comparing the total cell number of vital cells of the DMSO control with the total cell number of vital cells of the treated cells. The results show that **AuL9** inhibits cell proliferation of SK-N-AS cells in a dose-dependent manner (Fig. 9C). A concentration of 50 μM **AuL9** causes nearly 100% inhibition of proliferation, indicating G1 arrest.

For the investigation of the mechanism of action of **AuL9**, the mitochondrial membrane potential of SK-N-AS cells was measured after 48 h incubation with **AuL9**. It was shown that the mitochondrion and thus the intrinsic apoptosis pathway plays at least a partial role in the effect of **AuL9** (Fig. 10A).

To further characterize the role of mitochondria in **AuL9**-induced apoptosis, the apoptosis pathway mediated by reactive oxygen species (ROS) was investigated. Therefore, *N*-acetylcysteine (NAC) as a known ROS inhibitor and H_2O_2, which belongs to the ROS, as a positive control was investigated. It was shown that apoptosis induction could be significantly inhibited by NAC. It can therefore be concluded that the generation of ROS plays a role in the **AuL9**-induced apoptosis (Fig. 10B). However, it is not possible in the present state to be sure how the ROS are generated and whether **AuL9** directly leads to an increased ROS production or triggers pathways that result in the generation of ROS.

Overcoming cisplatin resistance

Cisplatin is a well-known chemotherapeutic agent for the treatment of many different types of cancer.[54] The development of resistance in tumor cells is a major problem in therapy and is usually the limiting factor in the cure of cancer patients.[55]

Fig. 11 SK-N-AS and SK-N-AS cisplatin resistant cells were treated with different concentrations of **AuL15** and incubated for 96 h. It is shown that **AuL9** was also effective in inducing apoptosis in cisplatin resistant cells, thus overcoming resistance. 8.25 μM cisplatin has been used as a positive control to prove resistance. Nuclear DNA fragmentation was analyzed by flow cytometric analysis. Values are mean% of apoptotic cells ± SD ($n = 3$); *: $p < 0.05$ vs. DMSO, *t*-test.

Therefore, it is of great importance for drug development that new agents are able to overcome cytostatic drug resistance. In addition to SK-N-AS cells, **AuL9** was tested on cisplatin resistant SK-N-AS cells and cisplatin resistance overcoming could be demonstrated (Fig. 11). In a previous characterization of the cisplatin resistant SK-N-AS cells, procaspase-8 under expression was shown.[56] The cisplatin resistance overcoming of SK-N-AS cells indicates that procaspase-8 has a minor role in **AuL9**-induced apoptosis.

Conclusion and outlook

A synthetic approach to a calix[4]imidazolinium macrocycle as saturated analog to **a** is presented. The synthesis of two new macrocyclic ligand systems, being bridged by ethylene groups and containing imidazoline (**H₄L5/6**) and imidazole moieties (**H₄L8/9**) are discussed. In addition, a novel bisimidazolinium ligand precursor (**H₂L3**) is described. All complexes (**Pd/PtL3**, **PdL5/6**, **Pd/PtL8**, **Au/PdL9**) with their respective ligands synthesized in this work are not accessible *via* the direct metalation of the respective ligand, due to irreproducible or unreliable results, except for **AuL9**. Even the route *via* the silver salt transmetalation does not lead to reliable results. The silver complexes of the respective ligands could not be isolated, probably due to instability of the respective complexes. Therefore, a modified synthetic method has been established. Here, *in situ* transmetalation with silver oxide is used in combination with the metal precursor and an excess of sodium acetate as a mild base, resulting in the corresponding complexes. Furthermore, the complexes **PdL3**, **PdL8**, **AuL9** and their respective ligands were tested for their ability to induce apoptosis on Naml-6 and SK-N-AS cells. According to the experiments performed, the data suggest that **AuL9** is capable of inducing apoptosis in malignant cells *via* the mitochondrial and ROS pathway. However, so far, an effect could only be observed on SK-N-AS neuroblastoma cells. In addition, a relatively high dose of **AuL9** is required to induce apoptosis in neuroblastoma cells, which could be challenging for clinical applicability. **AuL9** is able to overcome resistance to cisplatin in

Fig. 10 (A) The mitochondrial membrane potential in SK-N-AS cells was impaired by **AuL15** treatment, which implicates mitochondrial pathway involvement in apoptosis induction. The mitochondrial membrane potential was measured by flow cytometric analysis in SK-N-AS cells after 48 h of incubation with different concentrations of **AuL15** and staining with the cationic dye JC-1. Values are mean% of cells with low mitochondrial membrane potential ± SD ($n = 3$); *: $p < 0.05$ vs. DMSO, *t*-test. B The induction of apoptosis in SK-N-AS cells in response to **AuL15** treatment was shown to be dependent on the ROS mediated pathway. The cells were incubated for 72 h with 50 μM H_2O_2 as a positive control or different concentrations of **AuL15** with or without pretreatment of the cells with the ROS inhibitor *N*-acetylcysteine (NAC, 5 mM) 1.5 h prior to substance addition. Nuclear DNA fragmentation was analyzed by flow cytometric analysis. Values are mean% of apoptotic cells ± SD ($n = 3$); *: $p < 0.05$ vs. DMSO, *t*-test.

neuroblastoma cells (SK-N-AS) *in vitro*. Further characterization experiments would be required to determine the exact mechanism of action of **AuL9**, for example identification of molecular targets that are involved in the **AuL9** induced apoptosis, as well as the selectivity for cancer cells.

Experimental section

General procedures and analytical methods

Unless otherwise stated, all manipulations were performed under normal atmosphere without dried and degassed chemicals. All syntheses regarding the complexes were conducted under the exclusion of light. Every work-up was performed under normal atmosphere without dried and degassed chemicals; the complexes' work-ups were conducted in addition under the exclusion of light unless otherwise stated. Purification, in case of the Pt and Pd complexes, is achieved by dissolving the crude product in MeCN and filtering it through basic aluminum oxide to remove impurities. Acidic aluminum oxide promotes the decomposition of the complexes while pH-neutral aluminum oxide leads in smaller yields.[6] All obtained complexes are air- and water stable; however, **PtL3**, **PtL8** and **AuL9** decompose after extensive exposition to light. Solvents were obtained water-free from a MBraun solvent purification system and stored over molecular sieves (3 Å). The procedures for novel compounds obtained during the synthetic approaches to the saturated macrocyclic ligand precursor, containing 2-imidazoline moieties instead of 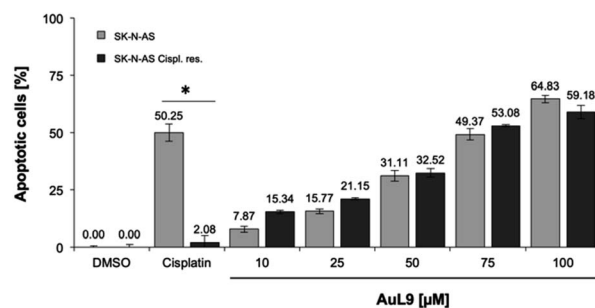imidazole, calix[4]imidazolinium, (2-imidazoline, *N*-benzyl-2-imidazoline, 3,3′-methylenebis(1-benzyl-2-imidazolinium)dibromide, N^1,N^1,N^2,N^2-tetrabenzylethane-1,2-diamine, *tert*-butyl (2-aminoethyl)carbamate, *tert*-butyl 2-imidazoline-1-carboxylate) are stated in the ESI.† *N*-Benzylethylenediamine (**12**),[57–59] ethylenebis(trifluoromethanesulfonate) (**4**),[60] 1,1′-ethylene-di-2-imidazoline (**1**)[23] and 1,1′-ethylenebis-1*H*-imidazolyl (**7**)[25,61] were synthesized according to literature procedures. All other reagents were purchased from commercial suppliers and used without further purification. NMR spectra were recorded on a Bruker Avance DPX 400 (¹H-NMR, 400 MHz; ¹³C-NMR, 100 MHz; ¹⁹F-NMR, 376 MHz) and chemical shifts are given in δ values in ppm (parts per million) relative to TMS (tetramethylsilane) and reported relative to the residual signal of the deuterated solvent.[62] Elemental analysis (C/H/N) were obtained by the Microanalytical Laboratory at Technische Universität München. Electrospray ionization mass spectrometry (ESI-MS) data were acquired on a Thermo Fisher Ultimate 3000 and with higher resolution (HR-ESI-MS) on Exactive Plus Orbitrap from Thermo Fisher.

Synthetic procedures

Alkylbisimidazoline diiodide (2). 1 (5.00 g, 30.0 mmol, 1.00 eq.) is dissolved in MeCN (300 mL) and MeI (213 g, 1.50 mol, 50.0 eq.) is added. The resulting reaction mixture is heated to reflux for 4 h. After cooling to ambient temperature, all volatile compounds are removed *in vacuo*. The resulting crude material is redissolved in a small amount of MeCN (5 mL) and an off-

white solid is precipitated after the addition of Et₂O (40 mL). The crude material is collected *via* centrifugation and washed with (3 × 5 mL) Et₂O. After removal of all volatile compounds *in vacuo*, **2** is obtained as an off-white solid (11.1 g, 24.7 mmol, 82%). ¹H-NMR (400 MHz, DMSO-d_6) δ (ppm) = 8.54 (s, 2H, N–C*H*–N), 3.91 (s, 8H, CH₃–N–C*H₂*–C*H₂*), 3.70 (s, 4H, C*H₂*–C*H₂*), 3.12 (s, 6H, C*H₃*). ¹³C-NMR (101 MHz, DMSO-d_6) δ (ppm) = 159.12 (N–*C*H–N), 50.96 ($C_{(backbone)}$), 48.70 ($C_{(backbone)}$), 45.02 (*C*H₂–*C*H₂), 35.08 (*C*H₃). Elemental analysis: for C₁₀H₂₀I₂N₄ (%) anal. calc.: C: 26.68, H: 4.48, N: 12.45, found: C: 26.66, H: 4.48, N: 12.39.

Alkylbisimidazolinium hexafluorophosphate (H₂L3). 2 (100 mg, 222 μmol, 1.00 eq.) is dissolved in H₂O (1 mL) and added to a solution of NH₄PF₆ (217 mg, 1.33 mmol, 6.00 eq.) in H₂O (1 mL). The resulting white precipitate is collected, washed three times with H₂O (2 mL, 2 mL, 1 mL) and dried subsequently *in vacuo*. Without further purification, the titled compound **H₂L3** is obtained as a white solid (98 mg, 202 mmol, 91%). ¹H-NMR (400 MHz, DMSO-d_6) δ (ppm) = 8.39 (s, 2H, N–C*H*–N), 3.88 (s, 8H, CH₃–N–C*H₂*–C*H₂*), 3.67 (s, 4H, C*H₂*–C*H₂*), 3.11 (s, 6H, C*H₃*). ¹³C-NMR (101 MHz, DMSO-d_6) δ (ppm) = 158.77 (N–*C*H–N), 50.36 ($C_{(backbone)}$), 48.12 ($C_{(backbone)}$), 44.55 (*C*H₂–*C*H₂), 34.43 (*C*H₃). ¹⁹F-NMR (376 MHz, DMSO-d_6) δ (ppm) = −70.15 (d, $^1J_{P-F}$ = 713 Hz, PF₆⁻). Elemental analysis: for C₁₀H₂₀F₁₂N₄P₂ (%) anal. calc.: C: 24.70, H: 4.15, N: 11.52, found: C: 24.28, H: 4.01, N: 11.17.

Calix[4](–Et–Et–)imidazoliniumtrifluoromethanesulfonate (H₄L5). 1 (1.00 g, 6.17 mmol, 2.00 eq.) is dissolved in dry MeCN (1.5 L), cooled to −45 °C and a solution of **4** (2.02 g, 6.20 mmol, 2.01 eq.) in dry MeCN (50 mL) is added dropwise over 6 h. After the addition, the reaction mixture is stirred for 72 h at ambient temperature. All volatile compounds are removed *in vacuo* and the resulting crude material is dried subsequently *in vacuo*. Without further purification the titled compound **H₄L5** is obtained as an off-white solid (1.50 g, 1.54 mmol, 50%). Note: everything is conducted under inert conditions. ¹H-NMR (400 MHz, DMSO-d_6) δ (ppm) = 8.46 (s, 4H, N–C*H*–N), 3.95 (s, 16H, C*H₂*(bridge/backbone)), 3.74 (s, 16H, C*H₂*(bridge/backbone)). ¹³C-NMR (101 MHz, DMSO-d_6) δ (ppm) = 159.16 (N–*C*H–N), 120.80 (q, $^1J_{19F-13C}$ = 320 Hz, OTf⁻), 48.15 (*C*H₂(bridge/backbone)), 44.54 (*C*H₂–*C*H₂(bridge/backbone)). ¹⁹F-NMR (376 MHz, DMSO-d_6) δ (ppm) = −77.74 (C*F₃*). Elemental analysis for C₂₄H₃₆N₈O₁₂F₁₂S₄ (%) anal. calc.: C 29.27; H 3.68; N 11.38; S 13.02 found: C 29.37; H 3.67; N 11.01; S 13.12.

Calix[4](–Et–Et–)imidazoliniumhexafluorophosphate (H₄L6). H₄L5 (300 mg, 304 μmol, 1.00 eq.) is dissolved in H₂O (50 mL) and added to a solution of NH₄PF₆ (223 mg, 1.37 mmol, 4.50 eq.) in H₂O (50 mL). The resulting white precipitate is collected, washed three times with H₂O (10 mL, 7 mL, 5 mL), Et₂O (3 mL, 2 mL) and dried subsequently *in vacuo*. Without further purification, the titled compound **H₄L6** is obtained as a white solid (240 mg, 248 μmol, 81%). However, a small amount of OTf⁻ is still detectable in the ¹⁹F-NMR. ¹H-NMR (400 MHz, DMSO-d_6): δ (ppm) = 8.44 (s, 4H, N–C*H*–N), 3.93 (s, 16H, C*H₂*(backbone)/C*H₂*,(bridge)), 3.72 (s, 16H, C*H₂*,(bridge)/C*H₂*,(backbone)). ¹H-NMR (400 MHz, CD₃CN): δ (ppm) = 7.98–7.82 (m, 4H, N–C*H*–N), 4.00–3.82 (m, 16H, C*H₂*,(backbone)/C*H₂*,(bridge)), 3.73–3.65

(m, 16H, $CH_{2,(bridge)}/CH_{2,(backbone)}$). ^{19}F-NMR (376 MHz, CD$_3$CN): δ (ppm) = −72.45 (d, $^1J_{P-F}$ = 713 Hz, PF$_6^-$). ESI-MS: m/z = calc. for [**H$_4$L6**−PF$_6^-$]$^+$: 823.20 ([M−PF$_6^-$]$^+$); found: 822.94; calc. for [**H$_4$L6**-2PF$_6^-$]$^+$: 339.11 ([**H$_4$L6**-2PF$_6^-$]$^+$); found: 339.12.

Calix[4](−Et−Et−)imidazoliumtrifluoromethanesulfonate (H$_4$L8). 7 (1.00 g, 6.17 mmol, 2.00 eq.) is dissolved in dry MeCN (1.5 L), cooled to −30 °C and a solution of **4** (2.02 g, 6.20 mmol, 2.01 eq.) in dry MeCN (100 mL) is added dropwise over 5 h. After the addition, the reaction mixture is stirred for 72 h at ambient temperature. All volatile compounds are removed *in vacuo* and the resulting crude material is washed eight times with cold acetone (10 mL, 5 mL, 5 mL, 3 mL, 3 mL, 2 mL, 2 mL, 1 mL) and dried subsequently *in vacuo*. Without further purification, the titled compound **H$_4$L8** is obtained as a white solid (1.50 g, 1.54 mmol, 50%). ^{1}H-NMR (400 MHz, CD$_3$CN) δ (ppm) = 8.57 (t, ^4J = 1.6 Hz, 4H, N−C*H*−N), 7.39 (d, ^4J = 1.7 Hz, 8H, C*H*), 4.71 (s, 16H, C*H*$_2$). ^{13}C-NMR (101 MHz, CD$_3$CN) δ (ppm) = 138.49 (N−*C*H−N), 124.49 (H*C*=*C*H), 121.80 (q, $^1J_{^{19}F-^{13}C}$ = 320 Hz, OTf$^-$), 50.14 (*C*H$_2$−*C*H$_2$). ^{19}F-NMR (376 MHz, CD$_3$CN) δ (ppm) = −79.32 (C*F*$_3$). ^{1}H-NMR (400 MHz, DMSO-d$_6$) δ (ppm) = 9.00 (t, ^4J = 1.7 Hz, 4H, N−C*H*−N), 7.57 (d, ^4J = 1.6 Hz, 8H, C*H*), 4.74 (s, 16H, C*H*$_2$). ^{13}C-NMR (101 MHz, DMSO-d$_6$) δ (ppm) = 137.08 (N−*C*H−N), 123.28 (H*C*=*C*H), 120.66 (q, $^1J_{^{19}F-^{13}C}$ = 320 Hz, OTf$^-$), 49.24 (*C*H$_2$−*C*H$_2$). Elemental analysis for C$_{24}$H$_{28}$N$_8$O$_{12}$F$_{12}$S$_4$ (%) anal. calc.: C 29.54; H 2.84; N 11.54; S 13.13 found: C 29.54; H 2.84; N 11.54; S 13.25. ESI-MS: m/z [**H$_4$L8**−4OTf$^-$]$^{4+}$ calc.: 95.06, found: 94.91, [**H$_4$L8**−3OTf$^-$]$^{3+}$ calc.: 176.39, found 176.36, [**H$_4$L8**−2OTf$^-$]$^{2+}$ calc.: 339.07, found: 339.22, [**H$_4$L8**−1OTf$^-$]$^{1+}$ calc.: 827.03, found 826.93.

Calix[4](−Et−Et−)imidazoliumhexafluorophosphate (H$_4$L9). **H$_4$L8** (3.20 g, 3.28 mmol, 1.00 eq.) is dissolved in H$_2$O (300 mL) and added to a solution of NH$_4$PF$_6$ (3.20 g, 19.66 mmol, 6.00 eq.) in H$_2$O (50 mL). The resulting white precipitate is collected, washed three times with H$_2$O (10 mL, 7 mL, 5 mL) and dried subsequently *in vacuo*. Without further purification, the titled compound **H$_4$L9** is obtained as a white solid (2.80 g, 2.85 mmol, 88%). ^{1}H-NMR (400 MHz, CD$_3$CN) δ (ppm) = 8.44 (t, ^4J = 1.6 Hz, 4H, N−C*H*−N), 7.33 (d, ^4J = 1.7 Hz, 8H, C*H*), 4.70 (s, 16H, C*H*$_2$). ^{19}F-NMR (376 MHz, CD$_3$CN) δ (ppm) = −72.30 (d, $^1J_{FP}$ = 713 Hz, PF$_6^-$). ^{1}H-NMR (400 MHz, DMSO-d$_6$) δ (ppm) = 9.00 (s, 4H, N−C*H*−N), 7.55 (d, ^4J = 1.6 Hz, 8H, C*H*), 4.73 (s, 16H, C*H*$_2$). ^{13}C-NMR (101 MHz, DMSO-d$_6$) δ (ppm) = 137.26 (N−*C*H−N), 123.49 (H*C*=*C*H), 49.44 (*C*H$_2$−*C*H$_2$). Elemental analysis for C$_{20}$H$_{28}$N$_8$F$_{24}$P$_4$ (%) anal. calc.: C 25.01; H 2.94; N 11.67; S 0.00 found: C 25.08; H 2.90; N 11.31; S 0.00.

Pd[C^{Et}C$_{imi}$(Me)$_2$C^{Et}C$_{imi}$(Me)$_2$]hexafluorophosphate (PdL3). Ag$_2$O (150 mg, 648 μmol, 1.05 eq.) is added to a solution of **H$_2$L3** (300 mg, 617 μmol, 1.00 eq.) and NaOAc (202 mg, 2.47 mmol, 4.00 eq.) in dry MeCN (15 mL) and stirred for 1 h at ambient temperature, followed by the addition of Pd(OAc)$_2$ (145 mg, 648 μmol, 1.05 eq.). The resulting reaction mixture is heated to 80 °C for 3 d. After cooling to ambient temperature, the reaction mixture is filtered over a short plug of basic aluminum oxide. The filter column is eluted with MeCN (20 mL) and all volatile compounds are removed *in vacuo*. The resulting crude material is resuspended in MeCN (5 mL) and centrifuged. Upon the addition of Et$_2$O (20 mL) to the supernatant, a white solid is precipitated. The crude material is collected *via* centrifugation, washed with Et$_2$O (3 × 5 mL), redissolved in MeCN (5 mL) and precipitated with Et$_2$O (15 mL). After drying *in vacuo*, the titled compound **PdL3** is obtained as an off-white solid (140 mg, 178 μmol, 29%). Single crystals suitable for SC-XRD were obtained by slow diffusion of Et$_2$O into MeCN solution of **PdL3**. ^{1}H-NMR (400 MHz, CD$_3$CN) δ (ppm) = 4.32−4.22 (m, 4H, C*H*$_{2(backbone)}$), 3.71−3.51 (m, 20H, C*H*$_2$−C*H*$_2$, C*H*$_{2(backbone)}$), 2.97 (s, 12H, C*H*$_3$). ^{13}C-NMR (101 MHz, CD$_3$CN) δ (ppm) = 195.6 (N−*C*−N), 51.72 (*C*$_{(bridge)}$, *C*$_{(backbone)}$), 51.26 (*C*$_{(bridge)}$, *C*$_{(backbone)}$), 46.5 (*C*H$_2$), 37.62 (*C*H$_3$). ^{19}F-NMR (376 MHz, CD$_3$CN): δ (ppm) = −72.94 (d, $^1J_{P-F}$ = 706 Hz, PF$_6$). ^{1}H-NMR (400 MHz, DMSO-d$_6$) δ (ppm) = 4.35−4.13 (m, 4H, C*H*$_{2(backbone)}$), 3.82−3.57 (m, 20H, C*H*$_2$−C*H*$_2$, C*H*$_{2(backbone)}$), 2.95 (s, 12H, C*H*$_3$). ^{13}C-NMR (101 MHz, DMSO-d$_6$) δ (ppm) = 194.29 (N−*C*−N), 50.94 (*C*$_{(bridge)}$, *C*$_{(backbone)}$), 50.56 (*C*$_{(bridge)}$, *C*$_{(backbone)}$), 45.76 (*C*H$_2$), 37.17 (*C*H$_3$). Elemental analysis: for C$_{20}$H$_{36}$F$_{24}$N$_8$P$_4$Pd$_1$ (%) anal. calc.: C: 30.60, H: 4.62, N: 14.28, found: C: 30.93, H: 4.55, N: 14.14, S: 0.00. HR-ESI-MS: m/z [**PdL3**−2PF$_6^-$]$^{2+}$ calc.: 247.1044, found: 247.1039, [**PdL3**−PF$_6^-$]$^+$ calc.: 639.1735, found: 639.1720.

Pt[C^{Et}C$_{imi}$(Me)$_2$C^{Et}C$_{imi}$(Me)$_2$]hexafluorophosphate (PtL3). Ag$_2$O (150 mg, 648 μmol, 1.05 eq.) is added to a solution of **H$_2$L3** (300 mg, 617 μmol, 1.00 eq.) and NaOAc (202 mg, 2.47 mmol, 4.00 eq.) in dry MeCN (15 mL) and stirred for 1 h at ambient temperature, followed by the addition of PtCl$_2$ (145 mg, 648 μmol, 1.05 eq.). The resulting reaction mixture is heated to 80 °C for 3 d. After cooling to ambient temperature, the reaction mixture is filtered over a short plug of basic aluminum oxide. The filter column is eluted with MeCN (20 mL) and all volatile compounds are removed *in vacuo*. The resulting crude material is resuspended in MeCN (5 mL) and centrifuged. Upon the addition of Et$_2$O (20 mL) to the supernatant, a white solid is precipitated. The crude material is collected *via* centrifugation, washed with Et$_2$O (3 × 5 mL) and redissolved in MeCN (5 mL) and precipitated with Et$_2$O (15 mL). After drying *in vacuo*, the titled compound **PtL3** is obtained as an off-white solid (23 mg, 26 μmol, 4%). Single crystals suitable for SC-XRD were obtained by slow diffusion of Et$_2$O into MeCN solution of **PtL3**. Note; a clean EA could not be obtained, and the NMR includes impurities. ^{1}H-NMR (400 MHz, CD$_3$CN) δ (ppm) = 4.35−4.26 (m, 4H, C*H*$_{2(backbone)}$), 3.72−3.51 (m, 20H, C*H*$_2$−C*H*$_2$, C*H*$_{2(backbone)}$), 2.94 (s, 12H, C*H*$_3$). ^{13}C-NMR (101 MHz, CD$_3$CN) δ (ppm) = 188.38 (N−*C*−N), 51.47 (d, *C*$_{(bridge)}$, *C*$_{(backbone)}$), 46.39 (*C*H$_2$), 37.44 (*C*H$_3$).

Pd[(cC^{Et}CC^{Et}C$_{imi}$)OTf] (PdL5). Ag$_2$O (155 mg, 670 μmol, 2.20 eq.) is added to a solution of **H$_4$L5** (300 mg, 305 μmol, 1.00 eq.) and NaOAc (200 mg, 2.42 mmol, 8.00 eq.) in dry MeCN/DMSO (12 mL 1:1) and stirred for 1 h at ambient temperature, followed by the addition of Pd(OAc)$_2$ (71.8 mg, 320 μmol, 1.05 eq.). The resulting reaction mixture is heated to 80 °C for 3 d and is filtered, after cooling to ambient temperature, over a short plug of basic aluminum oxide. The filter column is eluted with MeCN (100 mL) and all volatile compounds are removed *in vacuo*. The resulting oily solution (still approx. 6 mL of DMSO remaining) is resuspended in MeCN (6 mL) and centrifuged. Upon the addition of Et$_2$O (25 mL) to the supernatant, a brown/black solid is precipitated. After another addition of Et$_2$O (120 mL) a white

solid is precipitated. The white crude material is collected *via* centrifugation, washed with Et_2O (3×5 mL) and redissolved in MeCN (5 mL). After purification [3 times dissolving in MeCN (4 mL) and precipitating with Et_2O (~15 mL)] and removing all volatile compounds *in vacuo*, the titled compound **PdL5** is obtained as an off-white solid (7.00 mg, 8.87 µmol, 3%). ^{1}H-NMR (400 MHz, CD_3CN): δ (ppm) = 4.10–4.00 (m, 8H, $CH_{2,(bridge)}$), 3.76–3.54 (m, 16H, $CH_{2,(backbone)}$), 3.52–3.45 (m, 8H, $CH_{2,(bridge)}$). ^{13}C-NMR (101 MHz, CD_3CN): δ (ppm) = 191.3 (N–C–N), 51.0 ($CH_{2,(bridge)}$/$CH_{2,(backbone)}$), 47.4 ($CH_{2,(backbone)}$/$CH_{2,(bridge)}$). ^{19}F-NMR (376 MHz, CD_3CN): δ (ppm) = −79.33 (CF_3). ESI-MS: m/z = calc. for $[\textbf{PdL5}–OTf^-]^+$: 639.13 ($[\textbf{PdL5}–OTf^-]^+$); found: 639.44; calc. for $[\textbf{PdL5}–2OTf^-]^+$: 245.09 ($[M–2OTf^-]^+$); found: 245.20.

Pd[($cC^{Et}CC^{Et}C_{imi})PF_6$] (PdL6). PdL6 is synthesized analog to **PdL5**; by converting $\textbf{H}_4\textbf{L6}$ (230 mg, 238 µmol, 1.00 eq.) with Ag_2O (121 mg, 522 µmol, 2.20 eq.) in dry MeCN (4 mL) while stirring for 1 h at ambient temperature, followed by the addition of NaOAc (156 mg, 1.90 mmol, 8.00 eq.), $Pd(OAc)_2$ (56.0 mg, 249 µmol, 1.05 eq.) and is heated at 75 °C for 4 d. After purification [3 times dissolving in MeCN (4 mL) and precipitating with Et_2O (~15 mL)] and removing all volatile compounds, **PdL6** is obtained as a pale-yellow solid (85.0 mg, 109 µmol, 46%). ^{1}H-NMR (400 MHz, CD_3CN): δ (ppm) = 4.13–4.02 (m, 8H, $CH_{2,(bridge)}$), 3.78–3.60 (m, 16H, $CH_{2,(backbone)}$), 3.52–3.46 (m, 8H, $CH_{2,(bridge)}$). ^{19}F-NMR (376 MHz, CD_3CN): δ (ppm) = −72.78 (d, $^1J_{P31-F19}$ = 707 Hz, PF_6) elemental analysis for $C_{20}H_{32}F_{12}N_8P_2Pd$ (%) anal. calc.: C 30.76; H 4.13; N 14.13; found: C 29.50; H 4.07; N 14.35. ESI-MS: m/z = calc. for $[\textbf{PdL6}–PF_6^-]^+$: 635.14 ($[M–PF_6^-]^+$); found: 635.21. HR-ESI-MS: m/z $[\textbf{PdL6}–2PF_6^-]^{2+}$ calc.: 245.0887, found: 245.0890, $[\textbf{PdL6} + H_2O–2PF_6^-]^{2+}$ calc.: 254.0940, found: 254.0944, $[\textbf{PdL6}–PF_6^-]^+$ calc.: 635.1422, found: 635.1425, $[\textbf{PdL6} + H_2O–PF_6^-]^+$ calc.: 653.1527, found: 653.1534.

Pd[($cC^{Et}CC^{Et}C$)OTf] (PdL8). Ag_2O (74.7 mg, 322 µmol, 1.05 eq.) is added to a solution of $\textbf{H}_4\textbf{L8}$ (320 mg, 307 µmol, 1.00 eq.) and NaOAc (202 mg, 2.46 mmol, 4.00 eq.) in dry MeCN (15 mL) and stirred for 1 h at ambient temperature, followed by the addition of $Pd(OAc)_2$ (72.4 mg, 322 µmol, 1.05 eq.). The resulting reaction mixture is heated at 80 °C for 4 d. After cooling to ambient temperature, the reaction mixture is filtered over a short plug of basic aluminum oxide. The filter column is eluted with MeCN (50 mL) and all volatile compounds are removed *in vacuo*. The resulting crude material is resuspended in MeCN (5 mL) and centrifuged. Upon the addition of Et_2O (20 mL) to the supernatant, a white solid is precipitated. The crude material is collected *via* centrifugation, washed with Et_2O (3×5 mL) and redissolved in MeCN (5 mL). After the precipitation with Et_2O (15 mL) and drying *in vacuo*, the titled compound **PdL8** is obtained as an off-white solid (119 mg, 153 µmol, 50%). ^{1}H-NMR (400 MHz, CD_3CN) δ (ppm) = 7.20 (s, 8H, CH), 5.02–4.93 (m, 8H, CH_2), 4.47–4.39 (m, 8H, CH_2). ^{13}C-NMR (101 MHz, CD_3CN) δ (ppm) = 165.84 (N–C–N), 123.77 (CH), 49.11 (s, CH_2–CH_2). ^{1}H-NMR (400 MHz, DMSO-d_6) δ (ppm) = 7.52 (s, 8H, CH), 5.05–4.95 (m, 8H, CH_2), 4.52–4.42 (m, 8H, CH_2). ^{13}C-NMR (101 MHz, DMSO-d_6) δ (ppm) = 163.80 (N–C–N), 123.32 (CH), 48.14 (CH_2–CH_2). Elemental analysis for $C_{20}H_{28}N_8F_{24}P_4$ + 1 MeCN (%) anal. calc.: C 35.07; H 3.31; N 15.33; S 7.80 found: C 35.26; H 3.21; N 15.73; S 7.82. HR-ESI-MS: m/z $[\textbf{PdL8}–2OTf^-]^{2+}$ calc.:

241.0574, found: 241.0570, $[\textbf{PdL8}–OTf^-]^+$ calc.: 631.0674, found: 631.0658.

Pd[($cC^{Et}CC^{Et}C$)PF_6] (PdL9). PdL8 (95 mg, 122 µmol, 1.00 eq.) is dissolved in H_2O (35 mL), after the addition of NH_4PF_6 (50.0 mg, 305 µmol, 2.5 eq.) a white precipitate is collected *via* centrifuge and washed three times with H_2O (5 mL, 3 mL, 3 mL) and Et_2O (10 mL, 5 mL, 3 mL). After drying *in vacuo*, the titled compound **PdL9** is obtained as an off-white solid (39 mg, 50 µmol, 41%). Single crystals suitable for SC-XRD were obtained by slow diffusion of Et_2O into MeCN solution of **PdL8**. ^{1}H-NMR (400 MHz, CD_3CN) δ (ppm) = 7.22 (s, 8H, CH), 4.97 (m, 8H, CH_2), 4.43 (m, 8H, CH_2). ^{19}F-NMR (376 MHz, CD_3CN) δ (ppm) = −72.93 (d, $^1J_{FP}$ = 713 Hz, PF_6^-). HR-ESI-MS: m/z $[\textbf{PdL9}–2PF_6^-]^{2+}$ calc.: 241.0574, found: 241.0570, $[\textbf{PdL9}–PF_6^-]^+$ calc.: 627.0796, found: 627.0782.

Pt[($cC^{Et}CC^{Et}C$)OTf] (PtL8). Ag_2O (209 mg, 900 µmol, 2.20 eq.) is added to a solution of $\textbf{H}_4\textbf{L8}$ (400 mg, 410 µmol, 1.00 eq.) and NaOAc (202 mg, 2.46 mmol, 4.00 eq.) in dry MeCN (30 mL) and stirred for 1 h at ambient temperature, followed by the addition of $Pt(MeCN)_2Cl_2$ (156 mg, 450 µmol, 1.10 eq.). The resulting reaction mixture is heated to 80 °C for 3 d and is filtered, after cooling to ambient temperature, over a short plug of basic aluminum oxide. The filter column is eluted with MeCN (50 mL) and all volatile compounds are removed *in vacuo*. The resulting crude material is resuspended in MeCN (5 mL) and centrifuged. Upon the addition of Et_2O (20 mL) to the supernatant, a white solid is precipitated. The crude material is collected *via* centrifugation, washed with Et_2O (3×5 mL) and redissolved in MeCN (5 mL). After the precipitation with Et_2O (15 mL) and drying *in vacuo*, the titled compound **PtL8** is obtained as an off-white solid (90 mg, 103 µmol, 25%). ^{1}H-NMR (400 MHz, CD_3CN) δ (ppm) = 7.19 (s, 8H, CH), 5.11–4.94 (m, 8H, CH_2), 4.50–4.38 (m, 8H, CH_2). ^{1}H-NMR (400 MHz, DMSO-d_6) δ (ppm) = 7.49 (s, 8H, CH), 5.06–4.97 (m, 8H, CH_2), 4.54–4.44 (m, 8H, CH_2). ^{13}C-NMR (101 MHz, CD_3CN) δ (ppm) = 159.39 (N–CH–N), 123.58 (HC=CH), 48.86 (CH_2–CH_2). ^{19}F-NMR (376 MHz, CD_3CN) δ (ppm) = −79.27 (CF_3). HR-ESI-MS: m/z $[\textbf{PtL8}–2OTf^-]^{2+}$ calc.: 285.5881, found: 285.5864, $[\textbf{PtL8}–OTf^-]^+$ calc.: 720.1287, found: 720.1264.

Au[($cC^{Et}CC^{Et}C$)PF_6] (AuL9). $\textbf{H}_4\textbf{L8}$ (500 mg, 458 µmol, 1.00 eq.), $KAuCl_4 \times 2H_2O$ (209 mg, 505 µmol, 1.05 eq.), and NaOAc (197 mg, 2.41 mmol, 5.00 eq.) are suspended in dry DMSO (5 mL). The resulting reaction mixture is stirred for 5 h at 100 °C and filtered at ambient temperature. MeCN (5 mL) is added to the filtrate. After the addition of Et_2O (30 mL) to the solution, white solid precipitated. It is washed with MeCN (3×5 mL) and DCM (2×5 mL) and after the removal of all volatiles *in vacuo*, the solid is dissolved in H_2O (2 mL) and added dropwise to a solution of NH_4PF_6 (353 mg, 2.17 mmol, 4.00 eq.) in H_2O (5 mL). The resulting white precipitate is collected and washed with H_2O (3×5 mL) and after removal of all volatiles *in vacuo*, the titled compound **AuL9** (230 mg, 228 mmol, 47%) is obtained as a white solid. ^{1}H-NMR (400 MHz, CD_3CN) δ (ppm) = 7.47 (s, 8H, CH), 4.89–4.77 (m, 8H, CH_2), 4.76–4.66 (m, 8H, CH_2). ^{13}C-NMR (101 MHz, CD_3CN) δ (ppm) = 146.03 (N–CH–N), 125.92 (HC=CH), 48.58 (CH_2–CH_2). Elemental analysis for $C_{20}H_{24}$-$AuF_{18}N_8P_3 \times 0.1$ MeCN (%) anal. calc.: C 24.62; H 2.70; N 11.11;

S 0.00 found: C 24.82; H 2.78; N 11.15; S 0.57. HR-ESI-MS: m/z $[\textbf{AuL9}{-}3PF_6^-]^{3+}$ calc.: 191.0591, found: 191.0587, $[\textbf{AuL9}{-}PF_6^-]^+$ calc.: 863.1068, found: 863.1038.

Conflicts of interest

There are no conflicts to declare.

Notes and references

1 A. J. Arduengo, R. L. Harlow and M. Kline, *J. Am. Chem. Soc.*, 1991, **113**, 361–363, DOI: **10.1021/ja00001a054**.

2 P. Bellotti, M. Koy, M. N. Hopkinson and F. Glorius, *Nat. Rev. Chem*, 2021, **5**, 711–725, DOI: **10.1038/s41570-021-00321-1**.

3 T. P. Schlachta and F. E. Kühn, *Chem. Soc. Rev.*, 2023, **52**, 2238–2277, DOI: **10.1039/D2CS01064J**.

4 A. Biffis, M. Baron and C. Tubaro, in *Adv. Organomet. Chem.*, ed. P. J. Pérez, Academic Press, 2015, vol. 63, pp. 203–288, DOI: **10.1016/bs.adomc.2015.02.002**.

5 V. Charra, P. de Frémont and P. Braunstein, *Coord. Chem. Rev.*, 2017, **341**, 53–176, DOI: **10.1016/j.ccr.2017.03.007**.

6 M. A. Bernd, E. B. Bauer, J. Oberkofler, A. Bauer, R. M. Reich and F. E. Kühn, *Dalton Trans.*, 2020, **49**, 14106–14114, DOI: **10.1039/D0DT02598D**.

7 E. B. Bauer, M. A. Bernd, M. Schütz, J. Oberkofler, A. Pöthig, R. M. Reich and F. E. Kühn, *Dalton Trans.*, 2019, **48**, 16615–16625, DOI: **10.1039/C9DT03183A**.

8 J. F. Schlagintweit, C. H. G. Jakob, K. Meighen-Berger, T. F. Gronauer, A. Weigert Muñoz, V. Weiß, M. J. Feige, S. A. Sieber, J. D. G. Correia and F. E. Kühn, *Dalton Trans.*, 2021, **50**, 2158–2166, DOI: **10.1039/D0DT04114A**.

9 C. H. G. Jakob, B. Dominelli, J. F. Schlagintweit, P. J. Fischer, F. Schuderer, R. M. Reich, F. Marques, J. D. G. Correia and F. E. Kühn, *Chem.–Asian J.*, 2020, **15**, 4275–4279, DOI: **10.1002/asia.202001104**.

10 M. R. Anneser, S. Haslinger, A. Pöthig, M. Cokoja, J.-M. Basset and F. E. Kühn, *Inorg. Chem.*, 2015, **54**, 3797–3804, DOI: **10.1021/ic503043h**.

11 G. Moreno-Alcántar, P. Picchetti and A. Casini, *Angew. Chem., Int. Ed.*, 2023, **62**, e202218000, DOI: **10.1002/anie.202218000**.

12 M. Mora, M. C. Gimeno and R. Visbal, *Chem. Soc. Rev.*, 2019, **48**, 447–462, DOI: **10.1039/C8CS00570B**.

13 M. G. Karaaslan, A. Aktaş, C. Gürses, Y. Gök and B. Ateş, *Bioorg. Chem.*, 2020, **95**, 103552, DOI: **10.1016/j.bioorg.2019.103552**.

14 L. Oehninger, R. Rubbiani and I. Ott, *Dalton Trans.*, 2013, **42**, 3269–3284, DOI: **10.1039/C2DT32617E**.

15 I. Ott, in *Inorganic and Organometallic Transition Metal Complexes with Biological Molecules and Living Cells*, ed. K. K.-W. Lo, Academic Press, 2017, pp. 147–179, DOI: **10.1016/B978-0-12-803814-7.00005-8**.

16 I. Ott, in *Adv. Inorg. Chem.*, ed. P. J. Sadler and R. van Eldik, Academic Press, 2020, vol. 75, pp. 121–148, DOI: **10.1016/bs.adioch.2019.10.008**.

17 S. Nayak and S. L. Gaonkar, *ChemMedChem*, 2021, **16**, 1360–1390, DOI: **10.1002/cmdc.202000836**.

18 Nature Editorial, *Nature*, 2023, **617**, 438, DOI: **10.1038/d41586-023-01612-x**.

19 C. Heinemann, T. Müller, Y. Apeloig and H. Schwarz, *J. Am. Chem. Soc.*, 1996, **118**, 2023–2038, DOI: **10.1021/ja9523294**.

20 M. N. Hopkinson, C. Richter, M. Schedler and F. Glorius, *Nature*, 2014, **510**, 485–496, DOI: **10.1038/nature13384**.

21 T. P. Schlachta, Master's thesis, Technical University of Munich, Garching, Germany, 2020.

22 M. Scholl, S. Ding, C. W. Lee and R. H. Grubbs, *Org. Lett.*, 1999, **1**, 953–956, DOI: **10.1021/ol990909q**.

23 P. S. Athey and G. E. Kiefer, *J. Org. Chem.*, 2002, **67**, 4081–4085, DOI: **10.1021/jo016111d**.

24 Y. Chun, N. J. Singh, I. C. Hwang, J. W. Lee, S. U. Yu and K. S. Kim, *Nat. Commun.*, 2013, **4**, 1797, DOI: **10.1038/ncomms2758**.

25 Z. Li, E. R. R. Mackie, P. Ramkissoon, J. C. Mather, N. Wiratpruk, T. P. Soares da Costa and P. J. Barnard, *Dalton Trans.*, 2020, **49**, 12820–12834, DOI: **10.1039/D0DT02225J**.

26 J. W. Emsley, J. Feeney and L. H. Sutcliffe, *High Resolution Nuclear Magnetic Resonance Spectroscopy*, Elsevier, 2013, vol. 2.

27 R. J. Abraham, M. Canton and L. Griffiths, *Magn. Reson. Chem.*, 2001, **39**, 421–431.

28 P. de Frémont, N. Marion and S. P. Nolan, *Coord. Chem. Rev.*, 2009, **253**, 862–892, DOI: **10.1016/j.ccr.2008.05.018**.

29 H. V. Huynh, *Chem. Rev.*, 2018, **118**, 9457–9492, DOI: **10.1021/acs.chemrev.8b00067**.

30 T. P. Schlachta, G. G. Zámbó, M. J. Sauer, I. Rüter, C. A. Hoefer, S. Demeshko, F. Meyer and F. E. Kühn, *J. Catal.*, 2023, **426**, 234–246, DOI: **10.1016/j.jcat.2023.07.018**.

31 W. A. Herrmann, G. Gerstberger and M. Spiegler, *Organometallics*, 1997, **16**, 2209–2212.

32 P. De Fremont, N. Marion and S. P. Nolan, *Coord. Chem. Rev.*, 2009, **253**, 862–892.

33 J. F. Schlagintweit, L. Nguyen, F. Dyckhoff, F. Kaiser, R. M. Reich and F. E. Kühn, *Dalton Trans.*, 2019, **48**, 14820–14828.

34 P. J. Altmann, D. T. Weiss, C. Jandl and F. E. Kühn, *Chem.–Asian J.*, 2016, **11**, 1597–1605, DOI: **10.1002/asia.201600198**.

35 B. Dominelli, G. M. Roberts, C. Jandl, P. J. Fischer, R. M. Reich, A. Pöthig, J. D. G. Correia and F. E. Kühn, *Dalton Trans.*, 2019, **48**, 14036–14043, DOI: **10.1039/C9DT03035B**.

36 M. M. Watts, *J. Am. Oil Chem. Soc.*, 1990, **67**, 993–995.

37 M. A. Kalam, K. Haraguchi, S. Chandani, E. L. Loechler, M. Moriya, M. M. Greenberg and A. K. Basu, *Nucleic Acids Res.*, 2006, **34**, 2305–2315, DOI: **10.1093/nar/gkl099**.

38 C.-Y. Liao, K.-T. Chan, C.-Y. Tu, Y.-W. Chang, C.-H. Hu and H. M. Lee, *Chem.–Eur. J.*, 2009, **15**, 405–417, DOI: **10.1002/chem.200801296**.

39 W. A. Herrmann, M. Elison, J. Fischer, C. Köcher and G. R. J. Artus, *Angew Chem. Int. Ed. Engl.*, 1995, **34**, 2371–2374, DOI: **10.1002/anie.199523711**.

40 D. T. Weiss, P. J. Altmann, S. Haslinger, C. Jandl, A. Pöthig, M. Cokoja and F. E. Kühn, *Dalton Trans.*, 2015, **44**, 18329–18339, DOI: **10.1039/C5DT02386F**.

41 R. Dorta, E. D. Stevens, N. M. Scott, C. Costabile, L. Cavallo, C. D. Hoff and S. P. Nolan, *J. Am. Chem. Soc.*, 2005, **127**, 2485–2495, DOI: **10.1021/ja0438821**.

42 M. Süßner and H. Plenio, *Chem. Commun.*, 2005, 5417–5419, DOI: **10.1039/B512008J**.

43 F. E. Hahn, V. Langenhahn, T. Lügger, T. Pape and D. Le Van, *Angew. Chem., Int. Ed.*, 2005, **44**, 3759–3763, DOI: **10.1002/anie.200462690**.

44 R. McKie, J. A. Murphy, S. R. Park, M. D. Spicer and S.-z. Zhou, *Angew. Chem., Int. Ed.*, 2007, **46**, 6525–6528, DOI: **10.1002/anie.200702138**.

45 Z. Lu, S. A. Cramer and D. M. Jenkins, *Chem. Sci.*, 2012, **3**, 3081–3087, DOI: **10.1039/C2SC20628E**.

46 C. S. t. Brinke and F. Ekkehardt Hahn, *Dalton Trans.*, 2015, **44**, 14315–14322, DOI: **10.1039/C5DT02115D**.

47 H. M. Bass, S. A. Cramer, A. S. McCullough, K. J. Bernstein, C. R. Murdock and D. M. Jenkins, *Organometallics*, 2013, **32**, 2160–2167, DOI: **10.1021/om400043z**.

48 H. V. Huynh, Y. Han, R. Jothibasu and J. A. Yang, *Organometallics*, 2009, **28**, 5395–5404, DOI: **10.1021/om900667d**.

49 P. J. Altmann and A. Pöthig, *Chem. Commun.*, 2016, **52**, 9089–9092, DOI: **10.1039/C6CC00507A**.

50 H. M. Bass, S. A. Cramer, J. L. Price and D. M. Jenkins, *Organometallics*, 2010, **29**, 3235–3238, DOI: **10.1021/om100625g**.

51 E. B. Bauer, M. A. Bernd, M. Schütz, J. Oberkofler, A. Pöthig, R. M. Reich and F. E. Kühn, *Dalton Trans.*, 2019, **48**, 16615–16625.

52 It needs to be noted that the elemental analysis still includes MeCN as an impurity.

53 F. K.-M. Chan, K. Moriwaki and M. J. De Rosa, in *Immune Homeostasis: Methods and Protocols*, ed. A. L. Snow and M. J. Lenardo, Humana Press, Totowa, NJ, 2013, pp. 65–70, DOI: **10.1007/978-1-62703-290-2_7**.

54 S. Dasari and P. B. Tchounwou, *Eur. J. Pharmacol.*, 2014, **740**, 364–378, DOI: **10.1016/j.ejphar.2014.07.025**.

55 N. Vasan, J. Baselga and D. M. Hyman, *Nature*, 2019, **575**, 299–309, DOI: **10.1038/s41586-019-1730-1**.

56 J. F. Schlagintweit, C. H. G. Jakob, N. L. Wilke, M. Ahrweiler, C. Frias, J. Frias, M. König, E.-M. H. J. Esslinger, F. Marques, J. F. Machado, R. M. Reich, T. S. Morais, J. D. G. Correia, A. Prokop and F. E. Kühn, *J. Med. Chem.*, 2021, **64**, 15747–15757, DOI: **10.1021/acs.jmedchem.1c01021**.

57 A. Frost and A. Carlson, *J. Org. Chem.*, 1959, **24**, 1581–1582, DOI: **10.1021/jo01092a614**.

58 D. E. Goldberg and K. C. Patel, *J. Inorg. Nucl. Chem.*, 1972, **34**, 3583–3584, DOI: **10.1016/0022-1902(72)80260-4**.

59 L. W. Jenneskens, J. Mahy, E. M. M. de Brabander-van den Berg, I. van der Hoef and J. Lugtenburg, *Recl. Trav. Chim. Pays-Bas*, 1995, **114**, 97–102, DOI: **10.1002/recl.19951140305**.

60 E. Lindner, G. von Au and H. J. Eberle, *Chem. Ber.*, 1981, **114**, 810–813.

61 Z. Li, E. R. Mackie, P. Ramkissoon, J. C. Mather, N. Wiratpruk, T. P. S. da Costa and P. J. Barnard, *Dalton Trans.*, 2020, **49**, 12820–12834.

62 G. R. Fulmer, A. J. M. Miller, N. H. Sherden, H. E. Gottlieb, A. Nudelman, B. M. Stoltz, J. E. Bercaw and K. I. Goldberg, *Organometallics*, 2010, **29**, 2176–2179, DOI: **10.1021/om100106e**.

Hardware Article

MULA, an affordable framework for multifunctional liquid automation in natural- and life sciences with a focus on hardware design, setup, modularity and validation

Leon F. Richter [1], Wolfgang R.E. Büchele [1], Alexander Imhof, Fritz E. Kühn [*]

Technical University of Munich, TUM School of Natural Sciences, Department of Chemistry and Catalysis Research Centre, Molecular Catalysis, Lichtenbergstr. 4, Garching bei München, Germany

ARTICLE INFO

ABSTRACT

The implementation of automation has already had a considerable impact on chemical and pharmaceutical industrial laboratories. However, academic laboratories have often been more reluctant to adopt such technology due to the high cost of commercial liquid handling systems, although, in many instances, there would be a huge potential to automate repetitive tasks, resulting in elevated productivity. We present here a detailed description of the setup, validation, and utilization of a multifunctional liquid automation (MULA) system that can be used to automate various chemical and biological tasks. Considering that such a setup must be highly customizable, we also designed MULA with respect to modularity, providing detailed insight as far as possible. Including all 3D-printed parts and the used Hamilton gastight micro syringe, the total construction cost is approximately 700 €. This allows us to achieve a highly reliable and accurate system that exceeds the precision of a classical air displacement pipette while still retaining the ability to use closed vial (septa) setups. To encourage other groups to adopt this setup, detailed instructions and tips for every step of the process are provided, along with the complete CAD design of MULA and control code, which are freely available for download under the CC BY NC 3.0 license.

Specifications table.

Hardware name	MULA (Multifunctional liquid automation)
Subject area	• Engineering and materials science • Chemistry and biochemistry • Medical (e.g., pharmaceutical science) • Biological sciences (e.g., microbiology and biochemistry)
Hardware type	• Biological sample handling and preparation • Syringe manipulation

(continued on next page)

* Corresponding author.
E-mail address: fritz.kuehn@ch.tum.de (F.E. Kühn).
[1] Equally contributing authors.

(*continued*)

Hardware name	MULA (Multifunctional liquid automation)
	• Liquid and gas handling
Closest commercial analog	No commercial analog is available.
Open source license	CC BY NC 3.0
Cost of hardware	700 €
Source file repository	https://doi.org/10.17632/3m3t4f9ft3

1. Hardware in context

In the past decade, the development of automated systems has become increasingly important in daily laboratory operations, particularly for highly repetitive experiments like high throughput liquid handling work, which are prone to errors resulting especially from human influence.[1–6] A significant challenge faced by chemists and life scientists is achieving reproducible results.[7,8] A *meta*-analysis published in 2015 for the years 2011 to 2014 revealed that less than half of the data produced is reproducible, leading to substantial costs and time-consuming experiments, especially in drug research.[9] In the United States alone, over 28 billion[8,9] dollars are spent on non-reproducible preclinical research. However, even small enhancements in reproducibility or consistency could yield significant returns on investments in terms of cost reductions and time spent on drug development [8].

One potential solution is the deployment of liquid-handling robots, which offer consistent performance and operate 24/7. These robots boost throughput, document each step, lower labor costs, ensure a safer lab operation, and provide high precision and accuracy. [1,4] While companies like *Hamilton*, *Chemspeed Technologies*, *Mettler Toledo*, *Tecan* and *AmigoChem* already offer such robots, they require a significant budget and space for implementation and are optimized for rather specialized tasks.[4,10–12] If the assignment changes often, those robots are rarely appropriate and lack flexibility for easy modification or variation. Additionally, personnel must be trained for each company's specific system, as competing systems usually have no compatibility. In addition, technical support tends to prioritize larger industries more often than smaller university labs. When these robots require maintenance, they are usually not easy to fix, and the costs can be substantial, creating a significant burden for smaller groups with limited budgets. Furthermore, the customers can be very frustrated about the large downtimes of machines that are crucial for experiments. Simultaneously, there has been a rise in the use of G-code devices, including 3D printers, computer numerical control (CNC) routers, and laser engravers, which can achieve linear movements in a simple manner. Thanks to the RepRap project, the cost of these devices has significantly decreased in the last 15 years, making them accessible even to the general consumer.[13] Their potential for scientific purposes, including chemical synthesis[14], simplifying chromatographic processes[15], liquid handling[16], and fabricating functional materials[17] is a testament to their versatility and cost-effectiveness. On the other hand, commercial systems for liquid handling are often too expensive for the average academic research laboratory and lack the individual customization options of do-it-yourself (DIY) systems. Alternatives for specific experiments based on open-source 3D printing technology[18–20] have emerged, which are pretty similar to commercial ones; however, due to the open-source basis, the costs and makes are reduced, and the possibility for specially tailored robots for specific experiments is possible. By investing in versatile and cost-effective alternatives, laboratories can foster innovation while minimizing financial strain. Ultimately, embracing a more adaptable approach to automation will enable researchers to focus on discovery and innovation rather than logistical constraints and repetitive work, e.g., pipetting of defined volumes. Complementing already existing DIY liquid handling systems such as EvoBot[21], FINDUS[22], BioCloneBot [23] and OSMAR[24], we started developing MULA (Table 1). MULA represents a step forward in laboratory automation, offering a mixture of affordability, flexibility, highly customizable, and user-friendliness. It is designed for the needs of smaller labs and academic institutions in mind. The high customizability of MULA allows researchers to make easy modifications for new procedures or experiments without the need for costly overhauls or specialized training. In this manuscript, we present a detailed documentation of MULA and its setup, validation, and utilization as a multifunctional liquid automation robot with the intent of helping researchers focus on discovery and advancement without the constraints of high costs and inflexible equipment.

2. Hardware description

As the name implies, MULA (**mu**ltifunctional **l**iquid **a**utomation) is a highly modular and customizable framework that can be built

Table 1
List of DIY systems already published and compared to this work.

| Name, reference	OSMAR[24]	EVO-BOT[21]	FINDUS[22]	BioCloneBot[23]	MULA (this work)
Structural parts made *via*	Laser-cutting	Laser-cutting	3D-printing	3D-printing	3D-printing
Mainboard, Firmware	MKS Gen-L, custom Marlin	MEGA 2560 R3, custom Marlin	ESP8266 12F, custom	MKS Gen-L, custom	BTT Octopus, custom Marlin
Control *via*	AutoIt, Hype!terminal	Python script on Raspberry Pi	Python script	Custom C# frontend	Python script, Pronterface
Fluid dispensing *via*	Microsyringe & Needle	Plastic-syringe & Needle	Pipette & Tip	Microsyringe & Tip	Microsyringe & Needle
Proposed cost	$700AU	$600	$400 + pipette	<$2000CAD	~ 700€
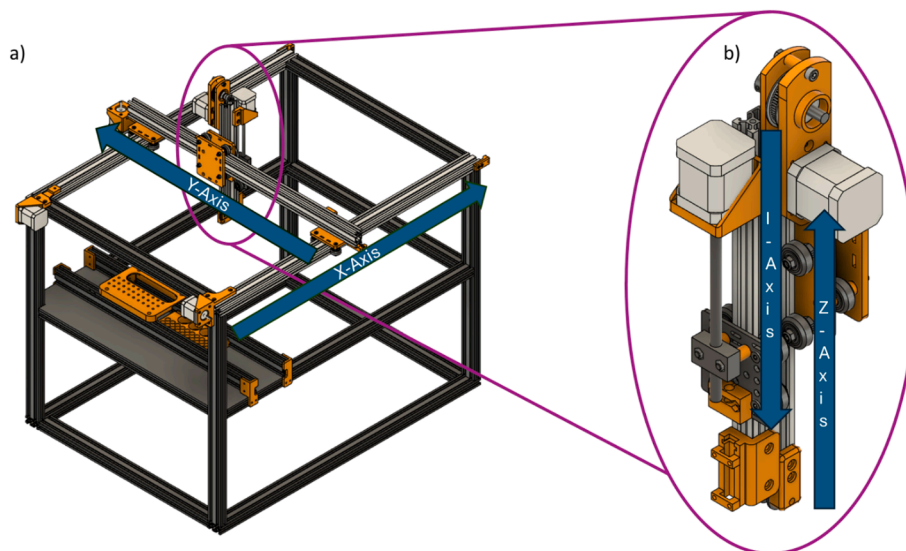
Fig. 1. CAD model of MULA: a) assembled frame with 3D-printed parts (orange) and 2040 V-slot profiles (white); b) Sampling head of MULA. For visibility reasons, some parts, like the electronics board case, are not depicted in this illustration. (For interpretation of the references to colour in this figure legend, the reader is referred to the web version of this article.)
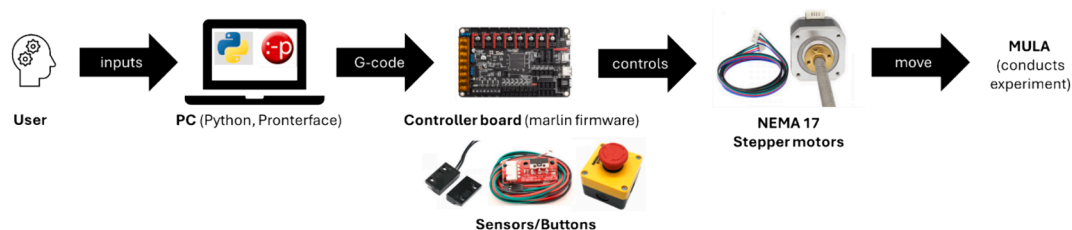
Scheme 1. Command-chain overview of MULA: The user inputs parameters to the PC, which are transformed into G-code commands, which the software then sends to the control board. The firmware on the board uses these instructions to control the stepper motors, which make MULA move accordingly and conduct the experiment.

in various sizes and for different applications. The robot is built with a cartesian motion system, which is the most common for DIY and commercial liquid handling systems, although there are some interesting exceptions [25]. The system has four movable axes. X- and Y-axes are both horizontal and use a timing belt mechanism, with the X-axis being duplicated. The two remaining axes are both vertical, using a lead screw (I-axis) and a geared timing belt (Z-axis) mechanism. All axes use 2040 V-slot profiles and V-slot wheels to support linear motion. We have decided to use a timing-belt mechanism with a 3:1 gear ratio for the Z-axis to combine the Z- and I-axis on one 2040 V-slot profile, making the head very compact. Fig. 1 depicts this elegant approach, which makes this system easy to assemble and more compact than other DIY approaches.[24] The X-, Y-, and Z-axes control the movement of the syringe, while the I-axis controls the movement of the syringe plunger. Since we have constructed MULA like a 3D printer, we wońt discuss the accuracy and reliability of the timing belt mechanisms of the X-, Y- and Z-axis but instead focus on the liquid handling ability. MULA contains a *Hamilton* micro syringe with a removable needle instead of an air displacement pipette since we plan to use this system with closed vials (septa) and notice during testing that air displacement pipettes are not ideal when using non-aqueous liquids. As a bonus, when using a gastight syringe, this system is also able to handle gases. We configured MULA with a sampling area measuring 41 cm on the Y-axis, 56 cm on the X-axis, and 10 cm on the Z-axis, although this can be easily adapted as described later. To adapt to different experimental conditions, we have designed a modular rack system that slides into regular aluminum profiles. The template of this rack as well as the rack-top part is supplied as a.step file and can easily be adjusted by common CAD tools. We provide a template for a 30-vial rack for GC vials. *NEMA* 17 stepper motors are employed on all axes due to their good availability and documentation. The BTT Octopus board with custom marlin firmware is used via a computer for motion control to run the stepper motors. Combining this specific board with the used *Trinamic* 2209 drivers allows to use a sensorless homing procedure for all axes except the Z-axis, reducing the number of limit switches and the associated wiring.[2] Sensorless homing is also achieved for the syringe plunger (I-axis), which improves reproducibility and user experience and reduces the need to manually recalibrate the position of the syringe plunger when an accident happens. In general, it can be assumed that the ability to home the machine is a significant safety and convenience feature, which we considered

---

[2] For more info visit https://marlinfw.org/docs/hardware/tmc_drivers.html (2024, June 26).

as missing on other DIY systems.[24] Furthermore, the board can control up to 8 individual stepper motors, allowing for further upgrades (as depicted in the outlook) since we currently only use 5 Motors (X_1, X_2, Y, Z, I). By using G-code instructions, the machine we designed is controlled using open-source and freely available software (Marlin, Pronterface), just like other machines such as 3D printers, CNC routers, and laser cutters. The complete process of communicating with MULA is depicted in Scheme 1.

While prototyping this machine, we developed several improvements over comparable DIY systems such as OSMAR and EVO-bot. Hamilton gastight syringes (although relatively costly) with removable needles make the system described in this work very versatile and durable, especially when dealing with liquids other than water (organic solvents like dichloromethane corrupt plastic syringes very quickly). Moreover, we want to highlight the high accessibility of this machine since all custom parts can be 3D-printed using a regular desktop 3D printer. There is no need for soldering or laser-cutting parts, which require harsh safety precautions and might not be accessible to smaller universities. Furthermore, our setup is compact, modular, user-friendly and simple to maintain and assemble.

In Summary:

- Accessible, simple to construct, easy to maintain and control
- Highly customizable
- Potential for further upgrades (see outlook)
- Cheap and modular system for automatic liquid handling

3. Design files

This section encompasses the 3D-printed components and firmware utilized in the construction and operation of MULA. As mentioned above, one advantage of our approach is that it does not require the use of sophisticated machines such as CNC routers and laser engravers. Instead, a basic desktop 3D printer is sufficient to create all custom parts.

3.1. 3D-printed parts

The files were printed with *Prusament* PETG on a *Prusa* I3 MK3S+ printer with a 0.6 mm nozzle. To increase the mechanical strength of all parts, the perimeter count was increased to 4 in *PrusaSlicer*. We printed the X- and Y-gantry and all stepper motor mounts with 80 % infill and 0.3 mm layer height. All other parts were printed with 40 % infill and 0.3 mm layer height. Besides all parts' .stl and .step files, we also provide the .3mf files (ready to print) with our settings in the repository. The 3D-printed parts make up a large part of the machine we developed. We have designed all 3D-printed parts to limit the number of different screw sizes where possible. Therefore, M4x10 and M3x10 screws are used to mount compounds to the aluminum profiles and attach stepper motors, respectively. There are three principal categories of parts:

- Mount: Those parts are mounted to the frame to support relevant mechanical or electronic structures
- Gantry: Those parts are incorporated in timing belts and are needed for the movement of the axes
- Spacer: Those parts are needed to fill gaps between other parts

Gantry_X contains several holes to mount the V-slot wheels and the timing belt and connect the Y-axis profile. Gantry_Y is a slightly more complex part to attach the V-slot wheels for the Y-axis, the timing belt of the Y-axis, but also the V-slot wheels for the Z-axis and the timing belt of the Z-axis. Gantry_Y_mount incorporates a mount for a cable drag chain. Furthermore, there are four mounts for the stepper motors (X_left, X_right, Y, I), accounting for different axial mounting conditions. Although they have a similar design, they are clearly distinguishable from each other.

For the Z-axis, a gearbox-like mount is utilized for the stepper motor, which is built from the two Z_Gearbox parts (A and B). Next, since the timing belt must be connected to an idler pulley at the other end of the axis, the Idler_mount part is needed for each one of the four axes employing a timing belt mechanism. The mounting of the micro syringe the frame is conducted using three parts: Syringe_mount is a parametric part that can be adapted for different syringe sizes and keeps the main body of the syringe connected to the I-, Z-axis profile; Plunger_mount, on the other hand, is another parametric part responsible for securing the plunger of the syringe to the I-axis gantry (there are also two versions for plungers with or without threads); Lastly, the Syringe_bracket parts are used to secure the syringe body to the Syringe_mount part. Then, there are 4 different parts needed for the pipetting area: 30Vial_rack and 96Well_rack, which contain the sample and solvent vials. They slide into the pipetting area profiles and can easily be customized. 30Vial_top is mounted on top of the pipetting area profiles and is needed to keep the vials in place when working with septa. The two parts named Rack_mount (A and B) are needed to connect the pipetting area profiles to the main frame and thus ensure a consistent location of all vials during the experiments. The small part labelled Endstop_mount is employed on the Z-Axis to mount the endstop switch to the Z-Axis profile. Lastly, the spacer parts (M5_Spacer_6, M5_Spacer_7, M4_Spacer_12 and M5_Spacer 14) are needed for encapsulating screws in different parts of the machine.

3.2. Software

3.2.1. Calculation of important parameters

Several parameters must be specified in the original marlin firmware when building a custom variant of MULA. While a large part of

Table 2

Software and hardware parameters and resulting calculated steps/mm for all axes of MULA.

Axis	Micro-stepping	Steps/Revolution (1.8° resolution)	Slope (lead screw)	Motor pulley teeth (T_m)	Distance teeth GT2 belt (b)	Gearbox ratio (r)	Calculated steps/mm
X,Y	16	200	–	20	2 mm	1	80
Z	16	200	–	20	2 mm	3	240
I	16	200	8 mm	–	–	1	400

Table 3

Custom modifications to the marlin firmware.

File	Line	Modification	Purpose
Config.h	174–188	Change the relevant (X, Y, Z, X2, I, E0) driver types to: **TMC2209**	Enables sensorless homing
	216	Comment (add "//" before): #define AXIS4_rotates	Use linear motion for the syringe plunger
	886, 894	Uncomment (remove "//" before): USE_IMIN_PLUG USE_ZMAX_PLUG	Enables endstops on I- and Z-axis
	964, 971	Change to: Z_MAX_ENDSTOP_INVERTING **true** Z_MIN_PROBE_ENDSTOP_INVERTING **true**	Invert logic of end-stop and probe to align with hardware setup
	1019, 1026, 1039, 1285	Change to: DEFAULT_AXIS_STEPS_PER_UNIT { **80, 80, 240, 400, 400**} DEFAULT_MAX_FEEDRATE { **5000, 5000, 2000, 200, 200**} DEFAULT_MAX_ACCELERATION { **500, 500, 300, 100, 100**} NOZZLE_TO_PROBE_OFFSET { **10, 10, 0, 0**}	To accommodate for the additional axis, enter the previously calculated steps/mm and set speed and acceleration
	1125	Comment (add "//" before): #define Z_MIN_PROBE_USES_Z_MIN_ENDSTOP_PIN	Enables homing on Z-axis
	1165	Uncomment (remove "//" before): FIX_MOUNTED_PROBE	Enables homing on Z-axis
	1412, 1424	Uncomment (remove "//" before): I_ENABLE_ON 0DISABLE_I false	Enables I-axis
	1444, 1485	Change to: INVERT_Z_DIR **true** Z_HOME_DIR **1**	Ensure that the Z-axis moves in the right direction
	1445, 1486	Uncomment (remove "//" before) and/or change to: INVERT_I_DIR **true** I_HOME_DIR −1	Enables correct homing for the syringe plunger
	1496, 1497, 1505	Change to: X_BED_SIZE **500** Y_BED_SIZE **350** Z_MAX_POS **75**	Sets the software limits for the sampling area; Can be disabled afterwards by the M221 G-code command (not recommended!)
	1506, 1507	Uncomment (remove "//" before) and change to: I_MIN_POS 0 I_MAX_POS **100**	Sets a software limit of 100 mm for the syringe plunger
	1887	Change to: HOMING_FEEDRATE_MM_M { **(50*60), (50*60), (10*60), (10*60)**}	Sets the speed for the homing procedure and includes the plunger axis
Config_adv.h	500, 502, 506, 507, 513	Uncomment (remove "//" before) and/or change to: USE_CONTROLLER_FAN CONTROLLER_FAN_PIN **FAN2_PIN** CONTROLLERFAN_SPEED_ACTIVE **170** CONTROLLERFAN_SPEED_IDLE **30** CONTROLLER_FAN_EDITABLE	Configures the Fan that cools the stepper drivers
	773	Uncomment (remove "//" before): #define INVERT_X2_VS_X_DIR	To make the second X-axis motor turn in the right direction
	837, 838	Change to: HOMING_BUMP_MM { **0, 0, 3, 0**} HOMING_BUMP_DIVISOR { **2, 2, 4, 2** }	Settings for sensorless homing; Only the non-sensorless Z-axis backoffs during homing
	844	Uncomment (remove "//" before): #define HOME_Z_FIRST	Ensures that the z-axis is up before homing other axes
	1014	Change to: AXIS_RELATIVE_MODES {**false, false, false, false, false**}	
	1039	Change to: DISABLE_INACTIVE_Z **false**	Ensures that the Z-axis wońt lower when inactive
	1264	Change to: MANUAL_FEEDRATE { **50*60, 50*60, 4*60, 4*60, 4*60**}	
	3078	Change to: CHOPPER_TIMING CHOPPER_DEFAULT_**24V**	
	3113, 3178	Uncomment (remove "//" before): MONITOR_DRIVER_STATUSSENSORLESS_HOMING	Enables sensorless homing
	3182, 3184, 3190, 3222	Uncomment (remove "//" before) and/or change to: X_STALL_SENSITIVITY **100** Y_STALL_SENSITIVITY **100** I_STALL_SENSITIVITY **100** TMC_DEBUG	Sets the sensitivity for sensorless homing; this can be changed afterwards using the M914 G-code command
Pins.h	54,	Change to: **I**_DIAG_PIN PG11	Enables the I-axis

(continued on next page)

Table 3 (*continued*)

File	Line	Modification	Purpose
	140 ff.	<pre>140 #ifdef I_STALL_SENSITIVITY
141   #define I_STOP_PIN   I_DIAG_PIN
142   #if I_HOME_TO_MIN
143   #define I_MAX_PIN   E3_DIAG_PIN // PWRDET
144   #else
145   #define I_MIN_PIN   E3_DIAG_PIN // PWRDET
146   #endif
147   #elif NEEDS_I_MINMAX
148   #ifndef I_MIN_PIN
149   #define I_MIN_PIN   I_DIAG_PIN // Z-STOP
150   #endif
151   #ifndef I_MAX_PIN
152   #define I_MAX_PIN   E3_DIAG_PIN // PWRDET
153   #endif
154   #else
155   #define I_STOP_PIN   I_DIAG_PIN // Z-STOP
156 #endif
157
158   #undef NEEDS_X_MINMAX
159   #undef NEEDS_Y_MINMAX
160   #undef NEEDS_Z_MINMAX
161 #undef NEEDS_I_MINMAX</pre>	Enables the I-axis
	209 ff.	<pre>209 #define I_STEP_PIN PG4 // MOTOR 3
210   #define I_DIR_PIN   PC1
211 #ifndef I_ENABLE_PIN
212   #define I_ENABLE_PIN   PA0
213 #endif
214 #ifndef I_CS_PIN
215   #define I_CS_PIN   PC7
216 #endif</pre>	Enables the I-axis

the settings will remain unchanged, there are some parameters that likely deviate. This includes the size of the sample area, the choice of stepper drivers (Note again that only TMC2209 and 2226 drivers support sensorless homing!), the sensitivity for sensorless homing and the default axis-steps per mm. Besides the dimension of the sample area (which is calculated in Chapter 5), another important parameter to specify in the firmware is the correct correlation between motor steps and mm. We want to demonstrate how we calculated this parameter in the following to make it as easy as possible to adapt the system to other possible configurations:

For the belt movements (X, Y, Z) we used the formula: $\frac{steps}{mm} = \frac{Steps/Revolution \ \times \ Microstepping}{T_m \ \times \ b} \times r$

For the movements of the lead screw (I), we instead used: $\frac{steps}{mm} = \frac{Steps/Revolution \ \times \ Microstepping}{Slope}$

Table 2 includes the used parameters and calculated steps/mm for our build. With the correct correlation between motor steps and mm, the movement of the X-, Y-, and Z-axis can be controlled precisely. Besides the different correlation of steps/mm, for the two different transmissions from rotational to linear motion (timing belt and lead screw), there are other factors to consider, such as longevity and accuracy. [26] The sensitivity for homeless probing (STALL_SENSITIVITY) was determined empirically. We found a value of 100 suitable for all axes, but this might differ in other builds.[3]

3.2.2. Modifications to the marlin firmware

In Table 3, we briefly comment on the parameters that we have changed from the original marlin configuration from the board manufacturer.

3.2.3. Flashing/Compiling of the firmware

MULA is controlled by a *BTT Octopus* 1.1 board, which is otherwise used to control DIY 3D printers. In order to send commands, the board requires a USB cable connection to a PC and the correct firmware. We recommend using a micro-SD card containing the Firmware.bin file according to the board's manual to flash the correct firmware to the Octopus board. The MULA marlin firmware build can be found in the repository. To reproduce our setup without significant changes, our Firmware.bin can be directly used (note that you can change many of the settings, such as the axis steps-per-unit *via* G-code commands in Pronterface: see https://marlinfw.org/meta/gcode/). However, if it is necessary to adjust the machine's dimensions or change the control board or stepper driver type, we advise recompiling the firmware from scratch using the VSCode editor and the platformIO IDE extension. Scheme 2 illustrates the decision tree for firmware flashing/compiling. A brief guide for setting up VSCode editor accordingly is available in the assembly manual, although this process is generally very well documented. Note that we have changed several parameters from the stock marlin configuration so that the user can adapt the firmware by changing the provided config.h and config_adv.h and the pins_BTT_OCTO-PUS_COMMON.h files.

3.2.4. Prerequisites for Machine control on windows

When the correct firmware is flashed and the electronics are connected properly, the board is ready to receive G-code commands (like a 3D printer) from the computer *via* USB. In 3D printing, the G-code file is generated in the slicer, where a complex algorithm

---

[3] For more information visit https://marlinfw.org/docs/gcode/M914.html (2024, June 26).
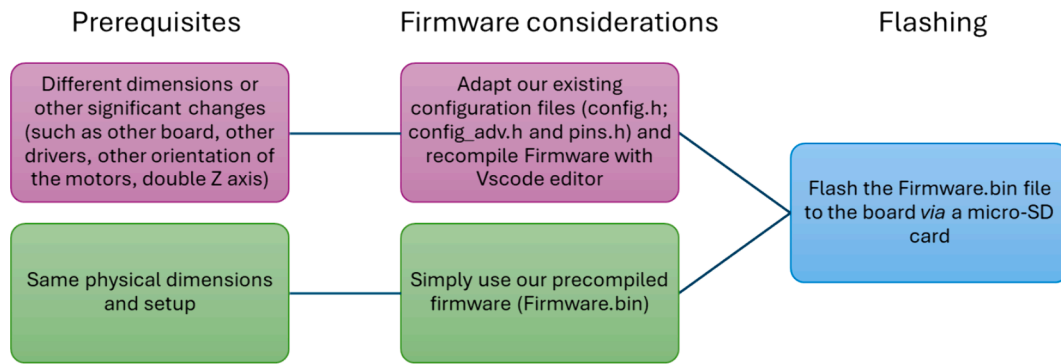
Scheme 2. Decision tree for the steps to flash the firmware to the control board.

generates the G-code file layer by layer based on the object's geometry. In our case, we had to approach the G-code generation differently. Therefore, we created a primitive slicer equivalent with an intuitive GUI that allows for straightforward input of all relevant parameters and then generates the respective G-code file. We are providing those programs as executables (.exe) files to eliminate the need to establish a working Python environment, which might overcharge inexperienced users. However, we still provide the original Python scripts in the repository for experienced users. The free software Pronterface should also be installed (from https://github.com/kliment/Printrun/releases) for initial calibration, manual control and sending of the G-code files.

3.3. Design files summary

Design file name	File type	Open source license	Location of the file
MULA_complete	STEP / F3D (Fusion 360)	CC BY NC 3.0	Mendeley Data repository: https://doi.org/10.17632/3m3t4f9ft3
MULA_Paranetric_syringe	STEP / F3D (Fusion 360)	CC BY NC 3.0	Mendeley Data repository
Gantry_X	STL	CC BY NC 3.0	Mendeley Data repository
Gantry_Y	STL	CC BY NC 3.0	Mendeley Data repository
Gantry_Y_mount	STL	CC BY NC 3.0	Mendeley Data repository
Stepper_mount_X_left	STL	CC BY NC 3.0	Mendeley Data repository
Stepper_mount_X_right	STL	CC BY NC 3.0	Mendeley Data repository
Stepper_mount_Y	STL	CC BY NC 3.0	Mendeley Data repository
Stepper_mount_I	STL	CC BY NC 3.0	Mendeley Data repository
Z_Gearbox_A	STL	CC BY NC 3.0	Mendeley Data repository
Z_Gearbox_B	STL	CC BY NC 3.0	Mendeley Data repository
Idler_mount	STL	CC BY NC 3.0	Mendeley Data repository
GT2_Belt_clip	STL	CC BY NC 3.0	Mendeley Data repository
Syringe_mount_100μL	STL	CC BY NC 3.0	Mendeley Data repository
Plunger_mount_100μL	STL	CC BY NC 3.0	Mendeley Data repository
Syringe_bracket_100μL	STL	CC BY NC 3.0	Mendeley Data repository
Syringe_mount_250μL	STL	CC BY NC 3.0	Mendeley Data repository
Plunger_mount_250μL	STL	CC BY NC 3.0	Mendeley Data repository
Syringe_bracket_250μL	STL	CC BY NC 3.0	Mendeley Data repository
Syringe_mount_1000μL	STL	CC BY NC 3.0	Mendeley Data repository
Plunger_mount_1000μL	STL	CC BY NC 3.0	Mendeley Data repository
Syringe_bracket_1000μL	STL	CC BY NC 3.0	Mendeley Data repository
Syringe_mount_2500μL	STL	CC BY NC 3.0	Mendeley Data repository
Plunger_mount_2500μL	STL	CC BY NC 3.0	Mendeley Data repository
Syringe_bracket_2500μL	STL	CC BY NC 3.0	Mendeley Data repository
30Vial_rack	STL	CC BY NC 3.0	Mendeley Data repository
96Well_rack	STL	CC BY NC 3.0	Mendeley Data repository
30Vial_top	STL	CC BY NC 3.0	Mendeley Data repository
Rack_mount_A	STL	CC BY NC 3.0	Mendeley Data repository
Rack_mount_B	STL	CC BY NC 3.0	Mendeley Data repository
Rack_mount_5mm_acrylic_A	STL	CC BY NC 3.0	Mendeley Data repository
Rack_mount_5mm_acrylic_B	STL	CC BY NC 3.0	Mendeley Data repository
Endstop_mount	STL	CC BY NC 3.0	Mendeley Data repository
M5_Spacer_6	STL	CC BY NC 3.0	Mendeley Data repository
M5_Spacer_7	STL	CC BY NC 3.0	Mendeley Data repository
M4_Spacer_12	STL	CC BY NC 3.0	Mendeley Data repository
M5_Spacer_14	STL	CC BY NC 3.0	Mendeley Data repository
Liquid_handling.exe	executable	CC BY NC 3.0	Mendeley Data repository
Volume_calibration.exe	executable	CC BY NC 3.0	Mendeley Data repository
Liquid_handling.py	Python script	CC BY NC 3.0	Mendeley Data repository

(continued on next page)

(continued)

Design file name	File type	Open source license	Location of the file
Volume_calibration.py	Python script	CC BY NC 3.0	Mendeley Data repository
config.ini	Configuration file	CC BY NC 3.0	Mendeley Data repository
MULA_Marlin firmware	Software package	CC BY NC 3.0	Mendeley Data repository

4. Bill of materials summary

The complete bill of materials can be found in the supplementary information. The total cost of all parts is 676.83 € in Germany, including the *Hamilton* gastight syringe and needle, as well as 1 kg of PETG filament. The cost of the tools and a 3D printer, as well as a PC for control, is not included.

5. Assembly instructions

Different angles of the CAD model are depicted in Fig. 2. To make the assembly of our system as straightforward as possible, we have eliminated the need for special tools and techniques like soldering. Since almost all necessary parts are 3D-printed, basically all
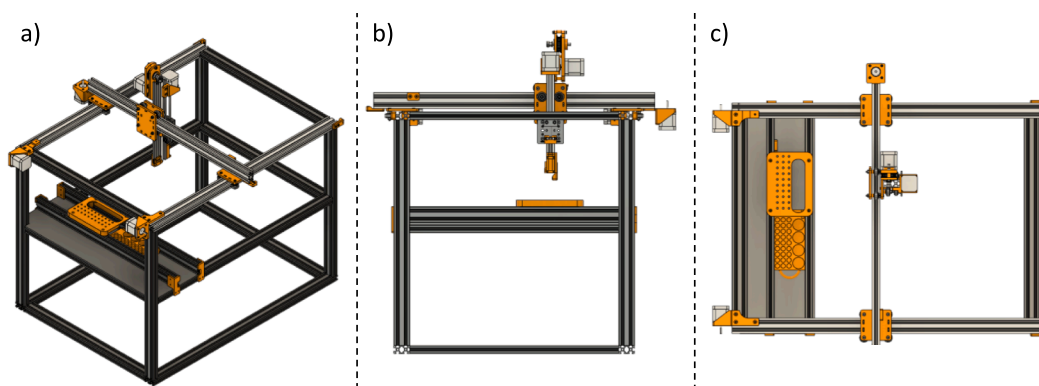

Fig. 2. CAD model of MULA in different orientations: a) Diagonal view b) side-view c) top-view.
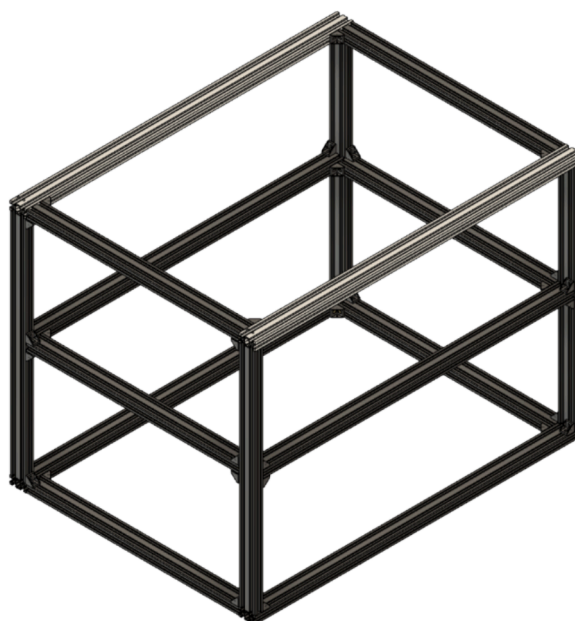

Fig. 3. Assembled structural frame of our implementation of MULA: A double cuboid made from 2040 Nut 6 aluminium profiles with dimensions of 800 x 600 x 600 mm. 2040 V-slot profiles are illustrated in white.

that is needed to build MULA is a set of hex keys, some pliers, and a wrench. If not available in the right length, the aluminum profiles and the hardened steel rod can be cut to the correct length in your mechanic's department or local hardware store.

Timing Belts: To cut the correct length of the timing belt, we recommend using the formula $L[mm] = 2(n + 150)$, where n is the length of the profile in mm. This accommodates the space needed for the idler- and stepper pulleys. It might be easier to connect the timing belt to the gantry plate with the provided clips or cable ties before assembly; however, connecting the belt to the already assembled and mounted gantry plate is also possible (and necessary later for the z-axis).

Hammer nuts: To ensure proper mounting to the frame, make sure the hammer nuts are aligned correctly. The flat side of the nut should be in contact with the aluminum profiles.

Sampling area: If MULA needs to be designed with respect to the effective sampling area X_s x Y_s x Z_s, the following formulae can be used to estimate the actual dimensions X x Y x Z of the frame, from which the actual lengths of the aluminum profiles are calculated as described in the next chapter:

$$X = X_s + 240 \ mm | Y = Y_s + 220 \ mm | Z = Z_s + 100 \ mm$$

Assembly manual: Since we wanted to make the assembly as easy as possible, we have created a detailed illustrated assembly manual, which we provide with the article in the supplementary information.

Aluminium profiles and frame assembly (assembly manual pages 1–3).

Most of the frame is assembled from standard 2040 aluminum extrusions as depicted in Fig. 3. However, the profiles where the two X-axis gantries are mounted should have a 2040 V-slot type. The profiles of the main frame are connected to each other with 90° corner brackets (in our case, made from metal but could also be 3D-printed), M4x10 screws and M4 hammer nuts. The main build has a frame

Table 4
Formulas to calculate the correct lengths and parts for the frame.

| Category	Our Build (800 x 600 x 600 mm)	Parametric double cuboid (**X x Y x Z**)	Parametric cuboid (**X x Y x Z**)
Motion	2 x 800 mm 2040 V-Slot	2 x **X** mm 2040 V-Slot	2 x **X** mm 2040 V-Slot
	1 x 700 mm 2040 V-slot	1 x (**Y**+100 mm) 2040 V-Slot	1 x (**Y**+100 mm) 2040 V-Slot
	1 x 200 mm 2040 V-Slot	1 x (**Z**/2 – 100 mm) 2040 V-Slot	1 x (**Z** – 100 mm) 2040 V-Slot
Frame	2 x 800 mm 2040	2 x **X** mm 2040	2 x **X** mm 2040
	2 x 760 mm 2040	2 x (**X** – 40 mm) 2040	4 x (**Y** – 80 mm) 2040
	6 x 520 mm 2040	6 x (**Y** – 80 mm) 2040	4 x (**Z** – 40 mm) 2040
	4 x 560 mm 2040	4 x (**Z** – 40 mm) 2040	24 x corner brackets
	44 x corner brackets	44 x corner brackets	48 x M4 x 10 screw
	88 x M4 x 10 screw	88 x M4 x 10 screw	48 M4 hammer nut
	88 M4 hammer nut	88 M4 hammer nut	
Rack	2 x 600 mm 2040	2 x **Y** mm 2040	2 x **Y** mm 2040
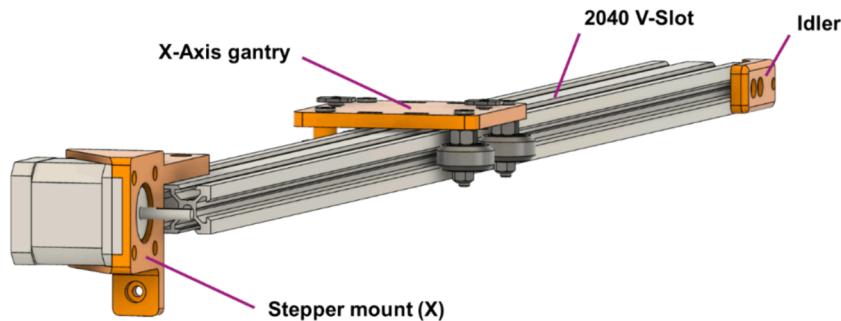
Fig. 4. CAD model of the assembled X-axis. Note that several parts were omitted, including screws, pulleys and belts.
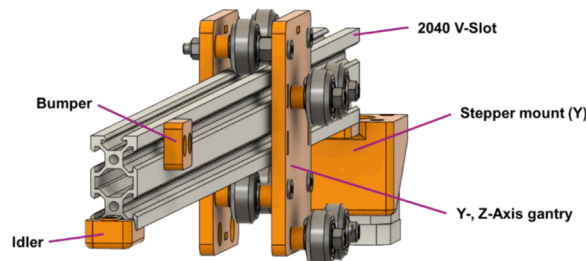
Fig. 5. CAD model of the assembled Y-axis. Note that several parts were omitted, including screws, pulleys and belts.
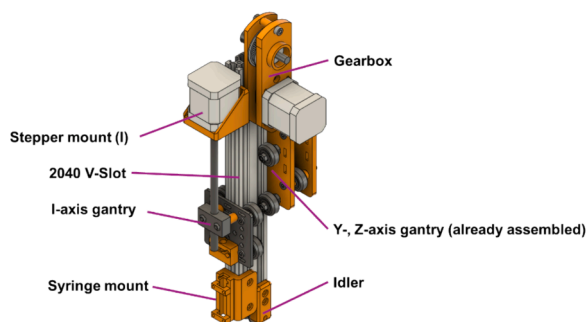
Fig. 6. CAD model of the assembled I-, Z-axis. Note that several parts were omitted, including screws, pulleys and belts.

size of 800 x 600 x 600 mm. However, if adjustment of the dimensions is planned to build MULA with the dimensions X x Y x Z (note that this is the size of the frame, not the sampling area), it is necessary to calculate the length of the 2040 profiles according to Table 4. V-Slot profiles are used to support the moving parts. We recommend cutting the Y-axis profile to Y+100 mm and the Z-axis profile to Z/ 2 − 100 mm for the double cuboid and Z − 100 mm for the cuboid (if the Z-axis is too long here, the syringe might drop to the bottom every time the motors are disabled).

For example, our implementation was designed to have a sample area of 380 mm in the Y-direction, leading to a total frame size of 600 (380 + 220) mm. The 2040 Y-axis V-slot profile then has a total length of 700 (600 + 100) mm.

X-Axis assembly (assembly manual pages 6–13, Fig. 4***).***

To assemble the X-axis, the first step is to assemble and mount the two X-axis gantries to the frame and continue by mounting the stepper motors and idler pulleys. Then, feed the belt over the pulleys and secure it to the gantries using zip-ties or 3D-printed clips. Lastly, attach two M4x10 screws and M4 hammer nuts on each gantry, where the y-axis profile will be connected later.

Y-Axis assembly (assembly manual pages 15–23, Fig. 5***).***

The Y-axis assembly is very similar to the X-axis; one Y-axis plate is assembled as described below. After this, connect the second Y-axis plate and attach the Y-axis gantry to the Y-axis profile. Then, attach the assembled Y-axis stepper mount and idler mount to the Y-axis profile. Proceed with the timing belt and secure it as described in the X-axis assembly. Lastly, attach the assembled Y-axis to the two X-axis gantries.
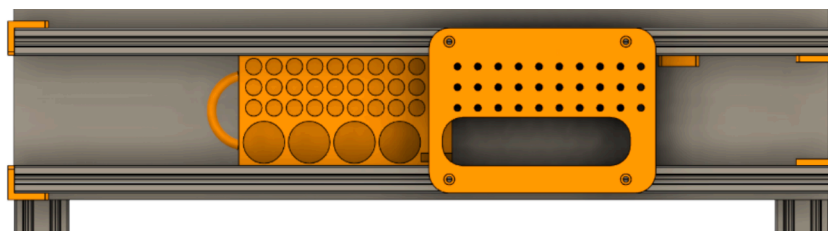

Fig. 7. Moveable rack assembly.
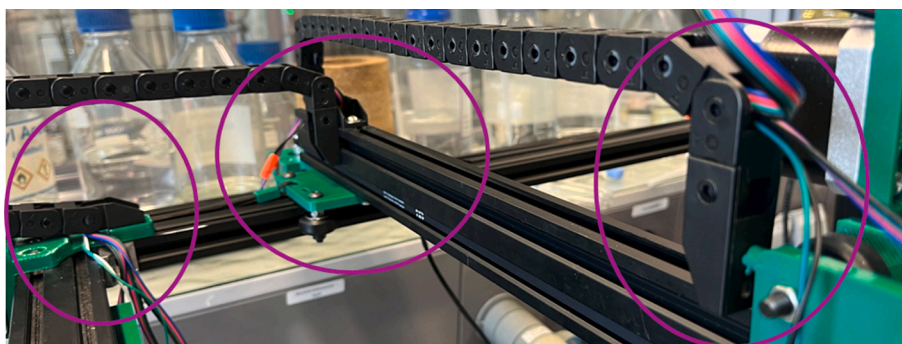

Fig. 8. Drag chain setup of MULA.

I-, Z-Axis assembly (assembly manual pages 24–41, Fig. 6***).***

The I-, Z-axis assembly begins with the Z-axis stepper gearbox assembly and attachment of the gearbox to the I-, Z-axis profile.
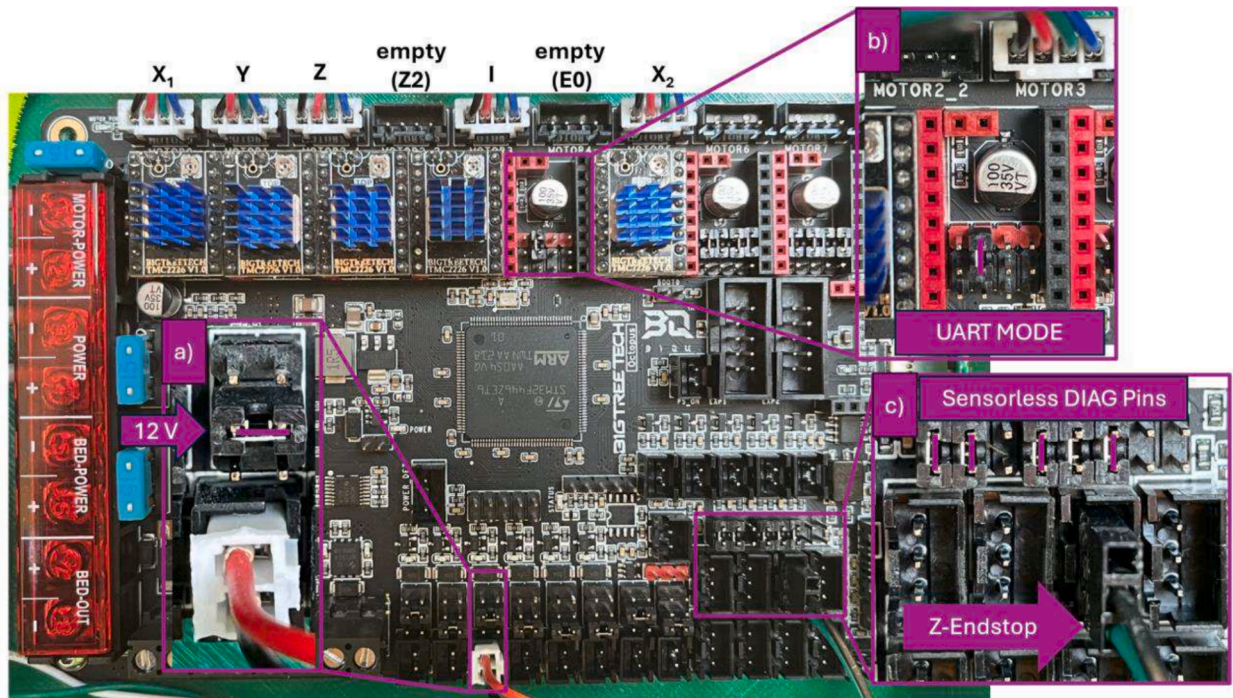
Fig. 9. Octopus control board; with a) showing the fan connector and fan power jumper (12 V). b) Show the driver's settings for UART mode. c) showing the sensorless DIAG Pings and the connected cable for the Z-endstop. The connected stepper motors to the X_1-,Y-, Z-, I- and X_2-axes are shown on the top left (more information at https://3dwork.io/en/btt-octopus/).

Then, attach the assembled I-axis stepper mount and I-axis gantry to the Z-axis profile. Next, mount the assembled idler mount to the lower end of the Z-axis profile and prepare the timing belt. Using a 200 mm long V-slot profile, we use around 700 mm of timing belt according to the aforementioned formula. Note that we had problems in sourcing the Acme nut block for the lead screw due to it only being available as part of an *Openbuilds* C-beam assembly. However, we found a 3D-printable version of the part that can be used as a replacement when printed from PETG.[4] We have created different mounts for *Hamilton* gastight syringes (100, 250, 1000 and 2500 μL). Note that the two larger volume syringe plungers have a thread in the plunger, and the smaller ones do not. We designed two variants of the Plunger_mount to accommodate this. Due to simpler detachment, we recommend using the threaded plunger when possible. Insert and mount the syringe into the Syringe_mount and secure it with the Syringe_bracket parts. Lastly, attach the assembly to the I-, and Z-axis profile and verify that the plunger can be attached to the Plunger_mount using a M3x8 screw.

*Rack assembly (assembly manual pages 42–48,*Fig. 7*).*

Attach the 30Vial_top part to one profile. Then, slide the 30Vial_rack into the aluminum profile (sometimes, the remains of support structures must be removed first; slide the rack back and forth on the profile until it moves smoothly). To ensure that the moveable rack does not move too far, align the rack with the holes of the Rack_top part and then secure it with a Bumper_30mm part. We have designed two variants of the Rack_mount (A/B) parts; one accommodates a 5 mm acrylic plate beneath the profiles, and the other one does not. Slide the second profile into both the top part and the moveable rack. Add two Rack_mountA/B parts and mount the assembly to the main frame. Make sure that the rack still can be removed. Then, attach the two remaining Rack_mountA/B parts on the other side of the rack to finish the rack assembly.

*Cable and board management (assembly manual pages 50, 51,*Fig. 8*).*

Two drag chains are used for proper cable management. One is mounted to the head of MULA on the Y-gantry_mount part with an M3x10 screw and on the Y-axis profile, while the other is also mounted to the Y-axis profile and to the Stepper_mount_right with an M4x16 screw.

Furthermore, we have incorporated the octopus control board in a 3D-printed case, which is then mounted to the frame to make the setup cleaner and better manage the cables from the board. We used an available case from Thingiverse[5] that suited our needs well.

*Electronic assembly and validation (assembly manual pages 55–56,*Fig. 9*).*

To ensure a safe and reliable operation, the assembly of the electronic part of MULA must be conducted carefully and with caution. Five or more *Trinamic* 2226 (or similar) drivers must be installed on the controller board after ensuring that the configuration jumpers

---

[4] For more information visit https://www.thingiverse.com/thing:2607994 (2024, June 30).
[5] For more information https://www.thingiverse.com/thing:5463756 (2024, June 30).
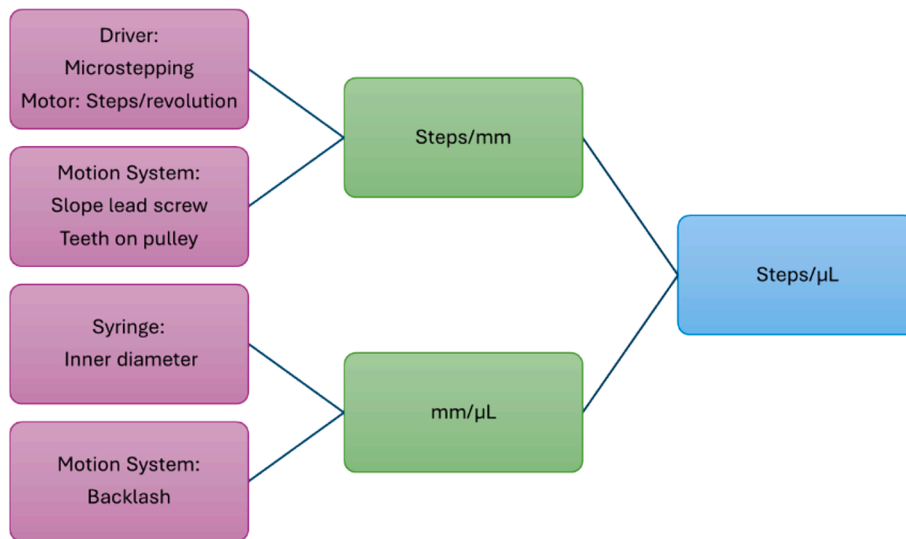
Scheme 3. Overview of the correlation of steps, mm and μL.

under each driver are set for UART mode, as depicted in Fig. 9b). Note that there is a free driver slot between the I- and X_2-axis drivers; this is where the driver for the extruder can be mounted. Then, the plugs from the stepper motors are connected to the board, as depicted at the top of Fig. 9. Since we are currently not using a double Z-axis, the 4th motor connector from the left side must be left empty. Furthermore, the power connectors and an emergency button are connected to the board. Then, the stallguard diagnostic jumpers and Z-endstop connector must be configured according to Fig. 9c. Lastly, the fan connector and fan power jumper must be configured according to Fig. 9a. After connecting all the electronics, the following steps are recommended to eliminate the possibility of false connections or other issues with the setup:

Firmware Flashing and Check: Prepare the firmware as previously described and flash it to the board by inserting the micro-SD card and powering it. Further information can be found in the control board manual (https://github.com/bigtreetech/BIGTREETECH-OCTOPUS-V1.0;page 20/21). Then, check if the flash was successful by removing the micro-SD card from the board and reinserting it into your PC; if the flash was successful, there should now be a file named FIRMWARE.CUR. It is unnecessary to place the micro-SD card back into the octopus board unless you want to flash a new firmware (in that case, just copy the new FIRMWARE.bin file to it). You can now connect the board to the PC using the provided USB-C cable. In the device manager, you should find the assigned COM port of the board, which must be selected in Pronterface in the next step.

Endstop Check: send the M119 command *via* Pronterface[6]; with our configuration, you should see the parameter z_max change from open to TRIGGERED when pressing the Z-axis end-stop switch and resending the M119 command.

Driver/Stepper Check: send the M122 command *via* Pronterface[7]; this should display some information for all configured stepper motors; when the driver and motor of one axis are installed correctly, all axes should be listed here.

Homing Check: The machine is ready to conduct a first homing sequence using Pronterface when all previous checks give good results. Make sure that nothing is obstructing the movement of the machine! Then, pressing the homing symbol will home all axes (Note: The Z-axis should always home first!). When the machine is not moving as expected, you can always press the emergency power cutoff and either adapt the firmware (invert homing directions) or check the wiring of the stepper motors before trying again.
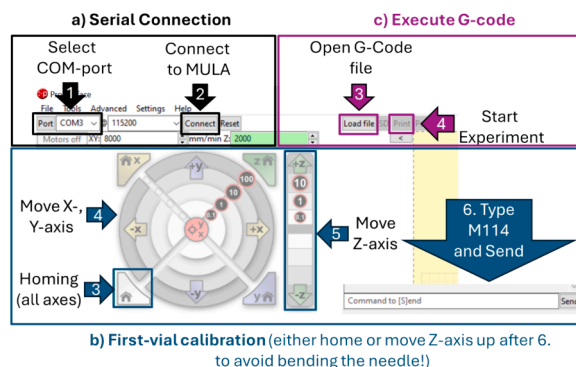
Volume correlation

For the movement of the syringe plunger, the unit mm is unsuitable since the user wants to specify a volume instead of a length. Therefore, a correlation between the linear motion of the plunger I-axis (in mm) and the actual dispensed volume (in μL) is crucial. Scheme 3 gives an overview of the parameters and other considerations to obtain a correlation between motor steps and dispensed μL. We are introducing this correlation not in the firmware. Instead, the Python script calculates the distance of the plunger according to the volume input and generates the appropriate G-code commands. In the following paragraph, the basic theory behind this approach is demonstrated:

To calculate the volume of the syringe displaced when moving the plunger 1 mm, the inner diameter (d) of the used syringe must be obtained from the manufacturer. Then, with the formula: $\frac{mm}{\mu L} = \frac{1}{\pi \times \left(\frac{d}{2}\right)^2}$ for d = 4.61 mm as in our case, we get a theoretical

---

[6] More information on https://marlinfw.org/docs/gcode/M119.html (2024, June 30).

[7] More information on https://marlinfw.org/docs/gcode/M122.html (2024, June 30).

Scheme 4. Pronterface tutorial: a) When opening Pronterface, the first step is always to establish a serial connection. In our case, COM-Port 3 is assigned to MULA. However, this can differ between setups. b) To conduct a first-vial calibration, start by homing all axes and then manually move the X- and Y-axis to the right position above the vial. Lower the Z-axis to verify and then request the position of the head by sending the M114 command via the terminal. c) To execute a G-code file, simply load the file and click the button labeled "Print" to start the experiment.

Table 5
Explanation of parameters in the config.ini file.

Parameter in the config.ini file	Purpose
min/max_volume	Min/max volume that should be handled with the installed syringe
theoretical_factor, backlash_correction	See the previous paragraph about volume calibration
vial1_x/y, solvent1_x/y, waste_x/y	Position of 1st sample vial, 1st solvent vial and waste
Number_of_solvents dx_s/dy_s, increment_y	Number of solvent positions in the used rackThe relative distance of vials and solvents in the rack, used by the script to calculate the positions of all other vials and solvents
vials_per_row, columns	Number of vials in the rack in Y (vials_per_row) and X (columns) direction
Z_min, Z_max Z_slow	Absolute minimum and maximum coordinates of the Z-axis Coordinates of the Z-axis for layering (not in contact with liquid)
Fz, Fxy	Speed for Z- and XY-movements
Fa_push, Fa_pull, Fa_slow	Plunger feed rate (speed) during pull- and push movements

correlation factor of around $0.06 \frac{mm}{\mu L}$, meaning that the I-axis has to move 0.06 mm (or $0.06\ mm \times 400 \frac{steps}{mm} = 24\ steps$) [see chapter 3.2.2] to dispense 1 µL. Therefore, with a 1000 µL syringe, we can achieve a theoretical volume resolution of $\frac{1 \mu L}{24 steps} \approx 0.0417\ \mu L$. If that is not enough, one could always further increase the micro-stepping of the I-axis (or better change to a smaller syringe). Keep in mind that a micro syringe will quickly lose accuracy with volumes smaller than 10 % of the maximum volume. However, during testing with only the theoretical correlation factor, we found that there was an absolute systematic error of around 25 µL for all tested volumes. A possible explanation for this observation might be the backlash of the plunger axis. For a detailed explanation of backlash in the field of liquid handling, please consider this article. [27] To tackle this error, a backlash correction is conducted with *absolute systematic error* $[\mu L] \times$ *theoretical_factor* $\frac{mm}{\mu L} =$ *backlash_correction* $[mm]$]. This procedure is detailed in the paragraph for volume calibration.

6. Operation instructions

6.1. Software

In Section 3.2, the requisite configuration of the control board has been delineated, encompassing driver installation and firmware upload. Once the aforementioned procedures have been completed, it is possible to utilize any software that facilitates serial communication in order to control MULA. Pronterface is our software of choice for accepting and executing G-code files. The software is used in two different ways. The first step is establishing a serial connection with the marlin control board. This is achieved by selecting the correct COM-port (when connecting MULA with a USB cable, the assigned COM-port appears in the port selection in the Pronterface) and clicking the *Connect* button (Scheme 4a). Then, the user can either load the G-code file and start an experiment by clicking the *Print* button or manually home the machine and conduct the first-vial calibration by moving the axes and sending the M114 command when at the correct positions to request the coordinates. The process of executing G-code files or conducting first-vial calibration is depicted in Scheme 4b) and c).

To generate a custom G-code file with the provided executables, the following things must be considered:

The config.ini file: This file stores many relevant parameters for vials, machine settings, and syringe size and is read by the executable every time it is launched. Ensure that the executable and the configuration file are in the same folder and that the correct configuration file is loaded. Due to changes in experiments, regular modification of this file is inevitable. In Table 5, the relevant
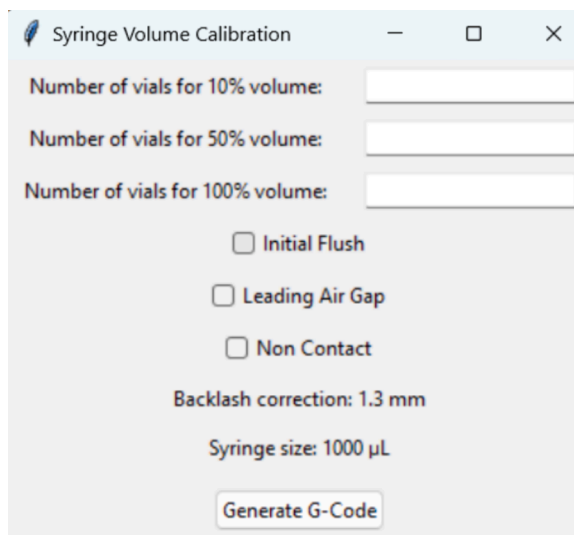
Fig. 10. The Syringe Volume calibration.exe file. The software, as depicted, gives the possibility, depending on which syringe is installed, to take 10%, 50%, or 100% of the maximum volume. In addition, the user can choose between different pulling modes to calibrate the syringe. Furthermore, the backlash correction can be calibrated as well by changing the config file.
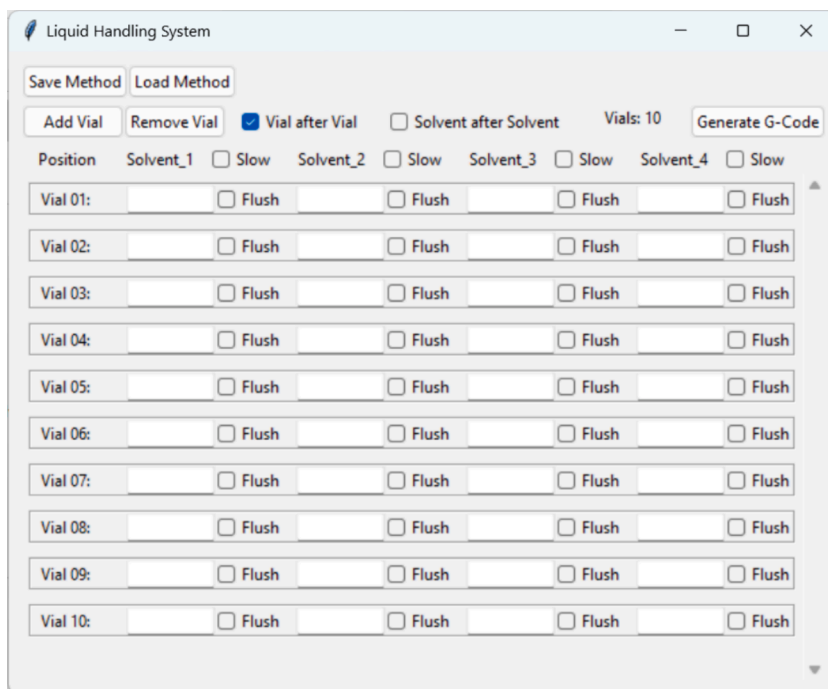

Fig. 11. GUI of the program for general liquid handling.

parameters in the config file are briefly explained.

The Volume calibration.exe file: For general calibration of syringes, we have created a GUI to generate G-code instructions for MULA (Fig. 10). The user can pull 10 %, 50 %, and 100 % of the maximum volume of the installed syringe as defined in the config file. By default, the user can fill a maximum of 30 vials in total with the installed rack. Furthermore, the user can choose between different modes, such as initial flush, leading air gap, and non-contact dispensing, while calibrating the syringe. It is also possible to use all the different pull methods at once. In our testing, using the Initial flush setting gives higher reproducibility; therefore, for volume calibration, we always use the initial flush mode at the beginning. MULA will then flush the installed syringe by default three times with the chosen fluid. In addition, the user can adjust the backlash correction in the config file and fine-tune the calibration of the syringe.

The Liquid handling.exe file: For general liquid handling tasks, we have created an intuitive GUI to generate G-code instructions
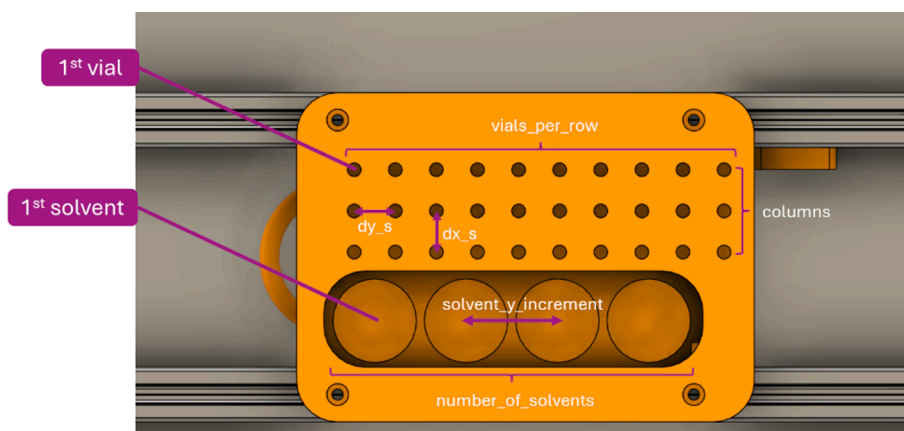
Fig. 12. Visual explanation of several parameters from the Rack section in the configuration file. For the depicted 30Vial rack, the following values are given: vials_per_row = 10; columns = 3; dx_s, dy_s = 15 [mm], solvent_y_increment = 35 [mm], number_of_solvents = 4 (when the waste is located somewhere else; otherwise set to 3 and calibrate the position of the most right solvent as waste coordinates.

for MULA (Fig. 11). Users can save or load a method with the respective buttons, as in commercial implementations. By default, there are 10 vials in the GUI, and the number of vials can be adapted by interacting with the two buttons to add or remove vials. Then, there are two modes of how MULA can handle the task: Vial after Vial and Solvent after Solvent. In the first mode, MULA fills one vial after another with all selected solvents, whereas in the second mode, it is ensured that all vials are filled with one solvent type before changing to the next solvent. This largely eliminates the need for flushing operations. Checkboxes for flushing operations are on the right side of each volume input window (white square; input in µL). If those are selected, MULA will flush once before executing the respective pipetting task. Lastly, by ticking the slow checkbox for a solvent type, all dispensing operations for that solvent will happen at a reduced speed and with contact-free dispensing (needle not in contact with liquid). This is especially useful when layering miscible solvents for crystal growth experiments.

6.2. Hardware

Safety considerations: The described machine deals with micro syringes with sharp needles that can be hazardous. The risk is even higher if the micro syringe samples are corrosive or poisonous liquids or gases. As the user must assemble the syringe driver in the presented setup, it is crucial to exercise care and attention to ensure proper operation and avoid exposing people to unnecessary risks. Furthermore, injuries can happen from the moving parts. Immediately press the emergency cutoff in the case of an emergency.

Positioning of the machine: The machine should be located on a flat surface, and ideally, dampeners should be mounted to the bottom of the frame to reduce vibrations. Verify that nothing obstructs the movement of the axes by carefully moving the head in all corners.

Dry run: Before attaching the needle to the syringe and connecting the plunger to the I-gantry, we suggest trying a dry run to validate all axes' correct function and homing and ensure no cable is stuck.
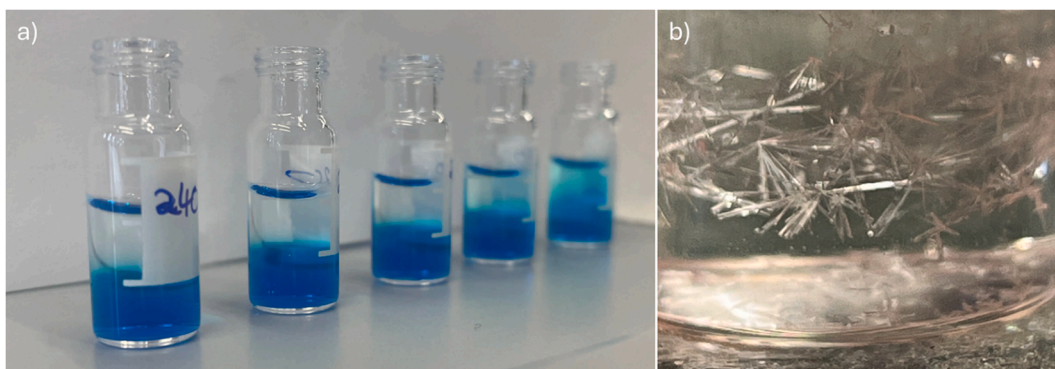
Fig. 13. Solvent layering experiments with MULA: a) optimization of the best dispensing velocity. Interestingly, going very slow did not yield the best results because the liquid then simply dropped down from the needle, disturbing the lower layer. We have found that a feed rate of 240 works best with a type 5 needle tip to ensure the liquid is dispensed via the glass vial wall. b) Single crystals of D-glucose after several layering attempts of a saturated aqueous D-glucose solution with acetone.

a) $A\ (\%) = \dfrac{100(V_0 - \bar{V})}{V_0}$
b) $VC\ (\%) = \dfrac{100s}{\bar{V}}$

$$with\ \bar{V} = \bar{x} \times \frac{1}{\rho_T}, \qquad \bar{x} = \frac{\sum x_i}{n}\ and\ s = Z \times \sqrt{\frac{\sum(x_i - \bar{x})^2}{n-1}}$$
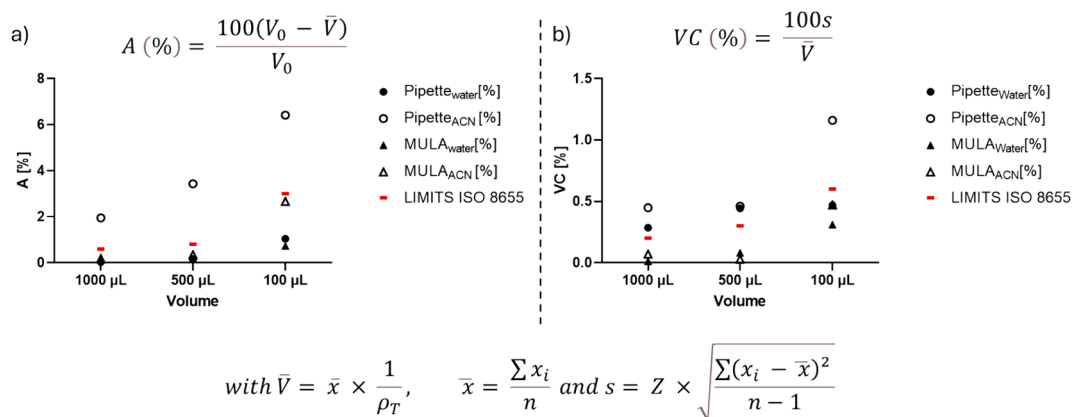
Fig. 14. Validation results of MULA in comparison to an air displacement pipette with water and acetonitrile (ACN) as solvents. a) Both MULA and the tested pipette show comparable accuracies within the ISO 8655 limits when water is used as a solvent. However, when an organic solvent like ACN is of interest, MULA delivers significantly better accuracy. b) For small volumes (100 μL), MULA delivers slightly better repeatability between measurements. For larger volumes (500, 1000 μL), interestingly, under the tested conditions, the pipette fails to fulfill the ISO 8655 limits, while MULA again yields significantly lower repeatability errors.

First-vial calibration: For a safe and reliable machine operation, it is critical to calibrate the absolute positions of the relevant 1st vial locations (sample, solvent and waste) in the removable rack when the needle is connected to the syringe (Fig. 12). Any misalignment can result in damage to the syringe needle. This can be accomplished after needle attachment by moving the syringe horizontally to the desired position in Pronterface and then slowly lowering the Z-axis (and readjusting the horizontal position) until it is in the middle of the vial opening. Command M114 can then be used to determine the absolute position of the vial. It is advisable to exercise caution during this procedure. Once the position of the first vial has been optimally adjusted, it must be stored in the config.ini file. Repeat this procedure also for the first solvent vial and the position of the waste. Don't forget to save the config.ini file afterwards. Despite the care taken during the initial positioning, it is virtually impossible to completely avoid accidents when dealing with micro syringe sampling because penetrating through septa can cause the needle to bend, necessitating either straightening or replacing with a new needle. Following the replacement of the needle, it is again essential to conduct a first-vial calibration.

Volume calibration: When absolute volume accuracy is critical for your work, volume calibration is recommended for each syringe-needle combination to accommodate for variations of the inner syringe diameter and backlash of the I-axis. This is done gravimetrically by weighing vials before and after the liquid handling task and adjusting the theoretical factor and/or backlash correction in the config.ini file:

1. If not done already, set the volume correlation factor in the config.ini file to the theoretical factor
2. Download the Excel template for volume calibration
3. Measure the weight of the empty test vials before the experiment
4. Conduct at least 3 samples each for 10 %, 50 % and 100 % of the total syringe capacity with the solvent of your choice
5. Measure the weight of the test vials after the liquid dispensing and calculate the mass of only the liquid
6. Calculate the volume of liquid using the correct density and compare with the target value
7. If the measured volume is too low, increase the value for backlash_correction according to the aforementioned formula and *vice versa.*

Syringe and needle configuration: Vials with thicker septa may present a challenge when attempting to puncture them using syringes with relatively thin needles (e.g. RN 26). Additionally, previously bent needles from accidents may prove more difficult to penetrate septa compared to new, straight needles. It is, therefore, necessary to conduct a trial-and-error process to identify the optimal combination of syringe and septum. Other than previously shown [24], *Hamilton* micro syringes with a type 2 needle tip were found to clog with silicone parts from the septum (soaking in toluene usually works to remove silicone remains from the needle) therefore, we investigated type 5 needles, which were highly reliable when used with 1.0 mm 55° shore A silicone/PTFE septa. Note that storing a separate config.ini file for each syringe size is a good practice when switching between several syringes.

7. Validation and characterization

There are several methods for growing single crystals for single-crystal X-ray diffractometry. Besides diffusion and cooling of a saturated solution, layering of two different solvents is a common technique to obtain the desired crystals. However, finding suitable solvents and solvent ratios can be very tiring and tricky. Using MULA, we conducted a high-throughput screening for crystal growth after optimizing the speed of adding the second layer. This is illustrated in Fig. 13a, where an aqueous solution of methylene blue is layered with acetone. We then used the slow checkbox for the liquid handling script with a type 5 needle (hole on the side; the liquid is

dispensed slowly via the glass vial wall) to automatically layer different volumes of acetone on top of a saturated glucose solution. This gave us beautiful crystals that we then analyzed to obtain a suitable molecular model for D-glucose, as depicted in Fig. 13b). Note that the execution of this experiment by MULA is also demonstrated in a short, detailed video that can be found in the repository. When screening multiple different solvent mixtures, using an automated liquid handler like MULA thus can save the user several hours of manual pipetting.

Furthermore, we tested the liquid handling performance according to DIN EN ISO 8655. The tests were performed *via* contact dispensing (needle in contact with liquid) using a 1000 μL *Hamilton Gastight* syringe with a removable needle (RN) in size 22 with a type 2 tip. As recommended in the ISO norm, we have conducted 10 measurements for each of the three specified volumes: 100 μL (10 %), 500 μL (50 %) and 1000 μL (100 %). Distilled water and HPLC-grade acetonitrile were used for the testing to further demonstrate the versatility of this system. For comparison, we had a trainee conduct the same experiments with a calibrated 1000 μL air displacement pipette. We then calculated the accuracy (**A**) and coefficient of variation (**VC**) according to the formulas for statistical quality control of air displacement pipettes. Those experiments again highlighted the advantages in accuracy and repeatability of MULA over classical air-displacement pipettes, especially for volatile liquids like acetonitrile, as depicted in Fig. 14.

To conclude, we have found automatic liquid handling using MULA to be superior to manual pipetting with an air-displacement pipette in the experiments that were conducted. Due to its simplified nature and control, MULA has some limitations. The control *via* open-loop-control (no direct feedback from MULA) might result in problems for more elaborate experiments. Currently, only one rack is supported simultaneously during an experiment (although this is rather a software limitation than a hardware limitation and can be resolved in the future), making more complicated experiments not feasible at the moment. Another limitation is that only one syringe can be integrated so far. However, this is currently being investigated since the hardware and electronic configuration can include a second individual Z-, I-Axis. Such a dual-syringe setup is useful for parallelizing experiments or excelling in dilution experiments, where both very large and very small volumes are transferred. Also, as an outlook, the ability to connect three more stepper motors to the control board enables creative users to complement the herein-reported modes with further improvements, such as a stepper-controlled centrifuge or a stepper-controlled sliding mechanism for lifting or locking vials in racks. Finally, our group is currently not only investigating the ability to conduct time-specific experiments (kinetic experiments) for different homogenous catalyzed reactions but also enabling a close-loop-control (direct feedback) setup by using a custom Python script to control MULA directly *via* serial communication.

CRediT authorship contribution statement

Leon F. Richter: Writing – original draft, Visualization, Validation, Software, Project administration, Methodology, Investigation, Data curation, Conceptualization. **Wolfgang R.E. Büchele:** Writing – original draft, Validation, Project administration, Investigation, Data curation, Conceptualization. **Alexander Imhof:** Software, Conceptualization. **Fritz E. Kühn:** Writing – review & editing, Resources.

Declaration of competing interest

The authors declare that they have no known competing financial interests or personal relationships that could have appeared to influence the work reported in this paper.

Acknowledgements

Appendix A. Supplementary data

Supplementary data to this article can be found online at https://doi.org/10.1016/j.ohx.2024.e00581.

References

[1] M.G.O. Lorenz, Liquid-Handling Robotic Workstations for Functional Genomics, SLAS Technology 9 (2004) 262–267, https://doi.org/10.1016/j.jala.2004.03.010.

[2] K. Potgieter, R. Meijboom, Robotics-assisted high-throughput catalytic investigation of PVP nanoparticles in the oxidation of morin, J. Chem. Technol. Biotechnol. 96 (2021) 2547–2557, https://doi.org/10.1002/jctb.6795.

[3] X. Yang, D. Acevedo, A. Mohammad, N. Pavurala, H. Wu, A.L. Brayton, R.A. Shaw, M.J. Goldman, F. He, S. Li, R.J. Fisher, T.F. O'Connor, C.N. Cruz, Risk Considerations on Developing a Continuous Crystallization System for Carbamazepine, Org. Process Res. Dev. 21 (2017) 1021–1033, https://doi.org/10.1021/acs.oprd.7b00130.

[4] L. Bessemans, V. Jully, C. de Raikem, M. Albanese, N. Moniotte, P. Silversmet, D. Lemoine, Automated Gravimetric Calibration to Optimize the Accuracy and Precision of TECAN Freedom EVO Liquid Handler, J. Lab. Autom. 21 (2016) 693–705, https://doi.org/10.1177/2211068216632349.

[5] M.A.H. Capelle, R. Gurny, T. Arvinte, High throughput screening of protein formulation stability: Practical considerations, Eur. J. Pharm. Biopharm. 65 (2007) 131–148, https://doi.org/10.1016/j.ejpb.2006.09.009.

[6] F. He, C.E. Woods, E. Trilisky, K.M. Bower, J.R. Litowski, B.A. Kerwin, G.W. Becker, L.O. Narhi, V.I. Razinkov, Screening of monoclonal antibody formulations based on high-throughput thermostability and viscosity measurements: design of experiment and statistical analysis, J. Pharm. Sci. 100 (2011) 1330–1340, https://doi.org/10.1002/jps.22384.

[7] C.G. Begley, J.P.A. Ioannidis, Reproducibility in Science, Circ. Res. 116 (2015) 116–126, https://doi.org/10.1161/CIRCRESAHA.114.303819.

[8] B. Miles, P.L. Lee, Achieving Reproducibility and Closed-Loop Automation in Biological Experimentation with an IoT-Enabled Lab of the Future, SLAS TECHNOLOGY: Translating Life Sciences Innovation 23 (2018) 432–439, https://doi.org/10.1177/2472630318784506.

[9] L.P. Freedman, I.M. Cockburn, T.S. Simcoe, The Economics of Reproducibility in Preclinical Research, PLoS Biol. 13 (2015) e1002165.

[10] M. Christensen, L.P.E. Yunker, P. Shiri, T. Zepel, P.L. Prieto, S. Grunert, F. Bork, J.E. Hein, Automation isn't automatic, Chem. Sci. 12 (2021) 15473–15490, https://doi.org/10.1039/D1SC04588A.

[11] M. E. DiLorenzo, C. F. Timoney, R. A. Felder, Technological advancements in liquid handling robotics, JALA: Journal of the Association for Laboratory Automation (2001), 6, 36-40. https://doi.org/10.1016/S1535-5535-04-00123-6.

[12] Q. Wei, B. Shi, F. Wang, S. Shao, L. Zhu, X. Zhao, Simple and Rapid Preparation of MIL-121 with Small Particles for Lithium Adsorption from Brine, Coatings 11 (2021) 854. https://www.mdpi.com/2079-6412/11/7/854.

[13] R. Arnott, The RepRap Project—Open Source meets 3D printing, (2008). https://hdl.handle.net/10523/1531.

[14] M. O'Brien, L. Konings, M. Martin, J. Heap, Harnessing open-source technology for low-cost automation in synthesis: Flow chemical deprotection of silyl ethers using a homemade autosampling system, Tetrahedron Lett. 58 (2017) 2409–2413, https://doi.org/10.1016/j.tetlet.2017.05.008.

[15] D. A. V. Medina, A. Lozada-Blanco, J. P. G. Rodríguez, F. M. Lanças, Á. J. Santos-Neto, An open-source smart fraction collector for isocratic preparative liquid chromatography, HardwareX (2023), 15. https://doi.org/10.1016/j.ohx.2023.e00462.

[16] A. Faiña, B. Nejati, K. Stoy, EvoBot: An Open-Source, Modular, Liquid Handling Robot for Scientific Experiments, Appl. Sci. 10 (2020) 814, https://doi.org/10.3390/app10030814.

[17] M. Politi, F. Baum, K. Vaddi, E. Antonio, J. Vasquez, B.P. Bishop, N. Peek, V.C. Holmberg, L.D. Pozzo, A high-throughput workflow for the synthesis of CdSe nanocrystals using a sonochemical materials acceleration platform, Digital Discovery 2 (2023) 1042–1057, https://doi.org/10.1039/D3DD00033H.

[18] J.M.P. Gutierrez, T. Hinkley, J.W. Taylor, K. Yanev, L. Cronin, Evolution of oil droplets in a chemorobotic platform, Nat. Commun. 5 (2014) 5571, https://doi.org/10.1038/ncomms6571.

[19] M.M. Hanczyc, J.M. Parrilla, A. Nicholson, K. Yanev, K. Stoy, Creating and Maintaining Chemical Artificial Life by Robotic Symbiosis, Artif. Life 21 (2015) 47–54, https://doi.org/10.1162/ARTL_a_00151.

[20] C. Zhang, B. Wijnen, J.M. Pearce, Open-source 3-D platform for low-cost scientific instrument ecosystem, J. Lab. Autom. 21 (2016) 517–525, https://doi.org/10.1177/2211068215624406.

[21] A. Faina, F. Nejatimoharrami, K. Stoy, EvoBot: An Open-Source, Modular, Liquid Handling Robot for Scientific Experiments, Appl. Sci. 10 (2020) 814, https://doi.org/10.3390/app10030814.

[22] F. Barthels, U. Barthels, M. Schwickert, T. Schirmeister, FINDUS: An Open-Source 3D Printable Liquid-Handling Workstation for Laboratory Automation in Life Sciences, SLAS Technology 25 (2020) 190–199, https://doi.org/10.1177/2472630319877374.

[23] K. K. C. D. H. Wells, N. Kharma, B. B. Jaunky, K. Nie, G. Aguiar-Tawil, D. Berry, BioCloneBot: A versatile, low-cost, and open-source automated liquid handler, HardwareX (2024), 18. https://doi.org/10.1016/j.ohx.2024.e00516.

[24] M.C. Carvalho, R.H. Murray, Osmar, the open-source microsyringe autosampler, HardwareX 3 (2018) 10–38, https://doi.org/10.1016/j.ohx.2018.01.001.

[25] G. Gome, J. Waksberg, A. Grishko, I. Y. Wald, O. Zuckerman, in Proceedings of the Thirteenth International Conference on Tangible, Embedded, and Embodied Interaction, Association for Computing Machinery: Tempe, Arizona, USA, 2019, pp. 55–64. https://doi.org/10.1145/3294109.3295619.

[26] D.C. Florian, M. Odziomek, C.L. Ock, H. Chen, S.A. Guelcher, Principles of computer-controlled linear motion applied to an open-source affordable liquid handler for automated micropipetting, Sci. Rep. 10 (2020) 13663, https://doi.org/10.1038/s41598-020-70465-5.

[27] A. Gervasi, P. Cardol, P.E. Meyer, Open-hardware wireless controller and 3D-printed pumps for efficient liquid manipulation, HardwareX (2021) 9, https://doi.org/10.1016/j.ohx.2021.e00199.